Spring 2018

Local properties and rupture characteristics of thoracic aortic aneurysm tissue

Yuanming Luo
University of Iowa

LOCAL PROPERTIES AND RUPTURE CHARACTERISTICS OF THORACIC AORTIC ANEURYSM TISSUE

by

Yuanming Luo

A thesis submitted in partial fulfillment of the
requirements for the Doctor of Philosophy
degree in Mechanical Engineering
in the Graduate College of
The University of Iowa

May 2018

Thesis Supervisor: Professor Jia Lu

Graduate College
The University of Iowa
Iowa City, Iowa

CERTIFICATE OF APPROVAL

PH.D. THESIS

This is to certify that the Ph.D. thesis of

Yuanming Luo

has been approved by the Examining Committee for the thesis requirement for the Doctor of Philosophy degree in Mechanical Engineering at the May 2018 graduation.

Thesis committee: _____
Jia Lu, Thesis Supervisor

_____
Stéphane Avril

_____
Stephen Baek

_____
Kyung K. Choi

_____
Sarah C. Vigmostad

_____
Shaoping Xiao

ACKNOWLEDGEMENTS

Dedicated to the people I love

ABSTRACT

Ascending thoracic aortic aneurysms (ATAAs) are focal dilatations in the aorta that are prone to rupture or dissect. Currently, the clinically used indicator of the rupture risk is the diameter. However, it has been demonstrated that the diameter alone may not properly predict the risk. To evaluate the rupture risk, one must look into the local mechanical conditions at the rupture site and understand how rupture is triggered in the tissue which is a layered fibrous media. A challenge facing experimental studies of ATAA rupture is that the ATAA tissue is highly heterogeneous; experimental protocols that operate under the premise of tissue homogeneity will have difficulty delineating the heterogeneous properties. In general, rupture initiates at the location where the micro-structure starts to break down and consequently, it is more meaningful to investigate the local conditions at the rupture site.

In this work, a combined experimental and computational method was developed and employed to characterize wall stress, strain, and property distributions in harvested ATAA samples to a sub-millimeter resolution. The results show that all tested samples exhibit a significant degree of heterogeneous in their mechanical properties. Large inter-subject variability is also observed. A heterogeneous anisotropic finite strain hyperelastic model was introduced to describe the tissue; the distributions of the material parameters were identified. The elastic energy stored in the tissue was computed. It was found that the tissue fractures preferentially in the direction of the highest stiffness, generating orifices that are locally transverse to the

peak stiffness direction. The rupture appears to initiate at the position absorbed of the highest energy.

Machine learning was used to classify the curves at rupture and non-rupture locations. Features including material properties and curve geometric characteristics were used. The work showed that the rupture and non-rupture states can indeed be classified using pre-rupture response features. A random forest algorithm was employed to provide insight on the importance of the features. Inspired by the importance scores provided by random forest, the rupture groups were interrogated and some strong correlations between the strength and the response features were revealed. In particular, it was found that the strength correlates strongly with the end stiffness, as well as tension at the point where the curvature of the total tension strain curve attains maximum, which occurs early in the response. The latter suggests that the strength, which cannot be measured without damaging the tissue, may be estimated from from pre-rupture response.

PUBLIC ABSTRACT

Ascending thoracic aortic aneurysms (ATAAs) threat people's life by sudden rupture causing deadly inner blooding. The current clinically used indicator of ATAAs rupture, i.e., the ATAAs' diameter, is insufficiently predicting the risk. From the mechanical point of view, rupture initializes locally where the stress acting on ATAAs is higher than the maximum stress that the tissue can sustain, i.e., the strength. In this work, a combined experimental and computational method was developed and employed to characterize wall stress, strain, and property distributions in harvested ATAA samples to a sub-millimeter resolution. The results show that all tested samples exhibit a significant degree of heterogeneous in their mechanical properties. It was found that the tissue fractures preferentially in the direction of the highest stiffness, generating orifices that are locally transverse to the peak stiffness direction. The rupture appears to initiate at the position where the tissue absorbed the highest energy per unit surface area. Machine learning was used to explore the possibility of detecting the rupture features. The work showed that the rupture and non-rupture states can indeed be classified using pre-rupture response features. It was found that the strength correlates strongly with the end stiffness, as well as tension at the point where the curvature of the total tension strain curve attains maximum. The findings suggest that the *in vivo* strength may be indirectly inferred by pre-rupture mechanical responses.

TABLE OF CONTENTS

LIST OF TABLES

Table

LIST OF FIGURES

Figure

LIST OF ALGORITHMS

Algorithm

CHAPTER 1
INTRODUCTION

An ascending thoracic aortic aneurysm (ATAA) is bulging and weakness in the wall of the ascending thoracic aorta. It affects approximately 10 out of 100,000 persons per year and is ranked the 15^{th} leading cause of death in individuals aged 65 years together with abdominal aneurysm [16, 39, 30]. A typical ATAA grows silently over many years until sudden dissection or rupture causing life-threatening internal bleeding [56, 29, 107, 74]. Study has shown that the mortality rate of the ruptured ATAA is so high that only forty-one percent of the patients were alive on arrival at an emergency hospital, and the overall mortality rate was 97% to 100% [67]. Untreated ATAAs are extremely dangerous. Pressler and Mcnamara reported that, if not treated, the 5-year rupture rate for patients was 47% and approximately 50% of patients with acute untreated ascending aortic dissection die within 48 hours [101]. Timely surgery is almost the only choice for the patients once the ATAAs rupture or dissect [14, 17, 21], but those who underwent emergency surgery still had 15-26% mortality [66, 50]. To avoid those subsequences, early diagnosis and surgical treatment to prevent dissection or rupture are essential. Elective surgery before rupture can lower mortality to only 3-5% [28]. However, a treatment decision should be made by balancing the risk of rupturing and surgery operation itself since the elective operation carries a mortality rate of approximately 5% to 9% [16, 101, 18]. Hence, the indicators of when the surgical intervention will be necessarily needed in the treatment become critical. Currently, the diameter of the ATAA is the most commonly-used criterion

for clinical treatment. Coady and Elefteriades et al. conducted a series of study over 10 years based on the accumulative patient data from Yale University [18, 17, 29]. After studying 1600 patients and 3000 serial images, they concluded that the critical size for the ATAA is 6.0 cm and by the time of reaching the point, the likelihood of rupture or dissection was 31% which is significantly higher than the one with less diameter [14, 32, 29]. Therefore, they recommended intervention for the ATAA at 5.5 cm, right before the critical size. The guidelines of thoracic aortic disease from Hiratzka and his colleagues drew the similar conclusion after they reviewed around 840 related papers[56]. However, there are many researchers questioned this criterion. Kallenbach et al. indicated that surgery at a diameter of ≥ 5.5 cm would lead to nearly one-fourth of patients at danger since the rupture or dissection also occurred at an aortic diameter < 5.5 cm in 22% of investigated patients [69]. Pape et al. delineated that many dissections or ruptures happen when the diameters are less than 5.5 cm and many stay intact even the diameter larger than 6.0 cm [93]. Kallenbach et al. concluded that aortic dissection or rupture involves a mechanical failure of the aortic wall and aortic size alone is a poor predictor of the rupture risk [69].

1.1 Aneurysm mechanics

Thanks to the rapid development of experiment techniques and finite element methods, stress analysis has become a helpful tool in understanding the mechanical behavior of aneurysm. Modern biomechanical studies of aneurysms initially focused on abdominal aortic aneurysms. Stringfellow et al. used finite element analysis to

determine the wall stress distribution and concluded that the ability of the aneurysm wall to withstand stress in the longitudinal as well as the circumferential directions is an important factor determining aneurysm rupture[115]. Vorp et al. investigated the effect of maximum diameter and asymmetric bulge on abdominal aortic aneurysm (AAA) wall stress[121]. They showed the wall stress is not evenly distributed and the potential for rupture is as dependent on aneurysm shape as it is on maximum diameter. Fillinger et al. obtained the 3D geometry of AAA by CT scan *in vivo* and determined the wall stress distribution by finite element analysis[38, 37]. They found that the wall stress is superior to maximum diameter for determining AAA rupture risk. Raghavan et al. developed a finite strain constitutive model for AAA and examined the variation of model parameters within their patient population[103]. They indicated that the patient-specific parameters were difficult to determine and the population property means are reasonably sufficient to calculate the wall stress. Wang et al. investigated the role of intraluminal thrombus (ILT) on AAA rupture[123]. They found that the presence of ILT alters the wall stress distribution and reduces the peak wall stress in AAA. Wilson et al. used a finite-element-based growth and remodelling model of evolving aneurysm geometry to show that regional variations in material anisotropy, stiffness and wall thickness should be expected to arise naturally and thus should be included in the analyses of aneurysmal enlargement or wall stress[124]. Gesst et al. suggested that the peak rupture potential index, which calculated as the ratio of locally acting wall stress to strength, may be better able to identify those AAAs at high risk of rupture than maximum diameter or peak wall stress along[118].

Lu et al. [83] computed the stress field for AAA by inverse finite element method and found that the conventional approach, which treats the deformed AAA state as reference, over-predicts the stress.

1.2 Biomechanical study of ATAA

There are mainly three experimental methods being used on investigate the ATAA mechanical properties: uni-axial tensile test, bi-axial tension test and bulge inflation test.

1.2.1 Uni-axial tensile test

Uni-axial tensile test is the simplest and most widely utilized method among the *vitro* testing methods to obtain material properties. By subjecting a sample to a controlled tensile displacement along a single axis, directional stress-strain curve and then is collected to determine the elastic tissue properties from the curve. The method assumes that the sample is homogeneous, and thus the stress and strain inferred from the end force and displacement can faithfully represent the true stress and strain in the center region of the specimen. If the material is heterogeneous, the samples must be cut sufficiently small. Samples from different locations must be harvested. To investigate the spatial variation of the ATAA tissue using uni-axial tensile test, Vorp et al. divided the harvest samples into longitudinal (LONG) or circumferential (CIRC) orientation and uni-axial tensile test was then performed on the samples[122]. They found that no significant difference in maximum tangential stiffness was noted between CIRC and LONG specimens. Iliopoulos et al. divided

twelve patients' data into groups according to direction and region, then performed uni-axial testing beyond rupture[63, 64]. Directionally, they showed that the failure stress (measure of tissue strength) and peak elastic modulus (measure of tissue stiffness) were significantly higher circumferentially in all regions. Regionally, they found that the anterior region longitudinally being the weakest and least stiff of all regions. They also indicated that no correlation was found between failure stress and ATAA diameter or patient age. Similarly, Khanafer et al. divided the samples into greater and lesser curvature groups then tested uniaxially in circumferential and longitudinal orientations[70]. It was found that the maximum elastic moduli in the lesser curvature were significantly higher in the circumferential orientation than in the longitudinal. Ferrara et al. divided their specimens into groups according to region (anterior *vs* posterior), direction (circumferential *vs* longitudinal), age (young *vs* old), gender (male *vs* female), valve type (tricuspid aortic valve, TAV, *vs* bicuspid aortic valve, BAV), and presence of hypertension, diabetes mellitus, and/or Marfan syndrome (*yes/no*) [34, 35]. Then, they further grouped the data according to the critical value of body mass index (BMI), maximum AsAA diameter, and aortic stiffness index (ASI),respectively. They tested the groups by uni-axial tensile test, then confirmed the anisotropy and heterogeneity of the ATAA tissue. As can be seen from above that the regional heterogeneity of the ATAA is a common phenomenon [111]. Although uni-axial test can provide different homogeneous properties from different samples (regions), but it can not identify heterogeneous or anisotropic information locally within one sample. Furthermore, there is no guarantee that results obtained

from a uni-axial test can be applied to a biaxial state [86].

1.2.2 Bi-axial tensile test

Since aneurysm tissues are stretched bi-axially in *vivo*, bi-axial test seems to be a better option to determine the material parameters, especially the anisotropic properties. By varying applied load ratios, bi-axial test can provide different datasets which could be particularly useful for developing advanced constitutive law. Consequently, bi-axial tensile test has been largely employed to study the mechanical properties of soft biological tissue [45, 130, 4, 51]. However, reports using the method on the ATAAs are still limited. Okamoto et al. studied the ATAA properties from the pathology angle. They harvested samples from patients suffering Marfan Syndrome, bicuspid aortic valve, or advanced age[102, 129]. Their bi-axial elastic results showed that the mean strength is significantly lower in older patients than younger suggesting that age may influence the ATAA rupture dissection of rupture. This finding is inconsistent with the result from Illiopoulos et al.. Pham et al. studied the bi-axial tissue properties from the patients harboring bicuspid aortic valve (BAV) or bovine aortic arch (BAA)[71]. The ultimate tensile strength of BAV and BAA samples are found to decrease with age and the BAV samples are stiffer than both ATAA and BAA samples. They also indicated that no apparent difference in failure mechanics among the tissue groups suggests that each of the patient groups may have a similar risk of rupture. Roberts et al. sectioned rings of human ascending aorta samples from healthy, dilated tricuspid aortic valve, and dilated bicuspid aortic

valve into quadrantsanterior, posterior, medial (inner curvature) and lateral (outer curvature)[104]. Low- and high- stress elastic moduli were calculated from the equi-biaxial stress-strain curve to determine the local mechanical properties. They claimed that the elastic modulus was dependent on quadrant and tissue type but not direction (isotropic) which contradicts with other results using the same method. Matsumoto et al. tested the stress-strain curves of the ATAA tissues and undilated part adjacent to the ATAA bi-axially[87]. By fitting the measured curves with a strain energy function considering material anisotropy, their results indicated that aneurysm tissues are not only stiffer but also more anisotropic than the nonaneurysmal tissues. Azadani et al. compared the mechanical properties of the ATAA tissues with normal human ascending aortas showing that ATAAs are much stiffer than normal ascending aortas at their respective physiologic stress[3]. And they further indicated that patient-specific physiologic stress does not correlate with maximum ATAA diameter, and patient-specific ATAA wall stress may be a useful variable to predict rupturing. Babu et al. draw the same conclusion by quantifying the biaxial mechanical properties of ATAA, and found significantly higher stiffness for dissected tissues, but did not correlate with greater aortic diameter[5].

As can be seen from these research, even though the bi-axial method can provide anisotropic information regionally, but some conflicting results show that the regional properties resolution may be too large that it still may not be able to investigate the local variations.

1.2.3 Bulge inflation test

Inflation test is another way to examine bi-axial mechanical properties of soft tissue [40, 119, 128]. The basic testing protocol is that the tissues are clamped flatly in the inflation device forming a hermetically sealed cavity. A fluid (water mostly) is successively injected at controllable rate to bulge the tissue and the pressure is measured simultaneously. The deformation of the tissue is tracked optically, and when it ruptures, a measure of tissue strength can be obtained [2]. This method certainly has been extended to the ATAA properties testing. Sugita et al. measeured rupture properties of thoracic aortic aneurysms (TAAs) in *vitro* in a inflation test to predict the ultimate stress of TAAs from their mechanical behavior in a physiological pressure range[117]. In-plane stress and strain of the specimen were calculated using Laplaces law and deformations of the markers drawn on the specimen surface, respectively. With the stress-strain curve, ultimate stress and tangent elastic modulus can be then determined. In addition, they defined a yielding parameter that can significantly distinguish between the TAAs sample and the control group which was porcine thoracic aortas. Romo et al. collected full field displacement data during each of the inflation tests using a digital image stereo-correlation (DIS-C) system and then derived the local stress fields at burst and estimated the thickness evolution. It was shown that rupture of the ATAA does not systematically occur at the location of maximum stress, but in a weakened zone of the tissue where the measured fields show strain localization and localized thinning of the wall[105] .

1.3 limitations of existing methods

One of the challenges in the experimental study of ATAA properties is that the ATAA tissues are heterogeneous. ATAAs undergo continuous remodeling, and the properties are modulated by the local cellular activities underneath the pathological development [68, 8, 54]. When the material is not reasonably homogeneous, these tests no longer generate a uniform stress field in the center region of specimen. Thus, the measured stress and strain are homogenized values over the specimen, not the local properties. For this and other reasons, it is not surprising that conflicting results were reported on the regional and directional stiffness and strength. In this regard, a fundamental limitation of the previous studies is the underlying assumption of tissue homogeneity.

1.4 Relation between strength and elastic parameters

The lack of reliable information about the tissue strength is one of the major challenges of stress-based evaluation. Existing studies have indicated that the material properties exhibit significant variabilities regionally. Some studies suggested that there could exist significant correlations between the ATAA strength and certain features of the stress response. For instance, Iliopoulos et al. reported that there is a direct correlation between the strength and the peak elastic modulus[63]. The same correlation was also reported for aorta root aneurysms [64]. Sugita et al. found that the strength correlates significantly with a 'yield point', namely a particular stress at the early phase of response [117, 116]. The importance of the latter is that the yield

point is more likely in *in vivo* stress range. Thus, the correlation opens the possibility of estimating the strength from *in vivo* response data, or using the yielding parameter as a surrogate of strength, which, is practically meaningful.

1.5 Objectives

Motivated by the need of delineating the local heterogeneous conditions of ATAA, and the needs of understanding the mechanical characteristics of ATAA rupture, the objectives of this study are:

1. Determining the ATAA tissue properties to a sub-millimeter resolution
2. Identifying the local conditions at the failure site
3. Explore the relation between heterogeneous properties and rupture characteristics
4. Searching for patterns, if any, in the stress-strain curves at ruptured and non-rupture sites using machine learning

1.6 Future applications

The work done in this study develops a method that can precisely identify local mechanical properties of ATAAs' tissues, including strength and explores a way to infer strength from pre-rupture mechanical responses. The method only takes deformation motion of the ATAA tissue and the corresponding pressure as input, which enables many potential usages in the future. A potential application *in vivo* is estimation of ATAA rupture risk. This requires one to collect 4D image data. With 4D image data, the developed method can be used to predict the stress and property

distributions. The set of response data at every Gauss point then forms a response database of an ATAA *in vivo*. The dataset will be further used in machine learning model to evaluate ATAAs' rupture risk. The method is expected to help on clinically evaluating the rupture potential of ATAA, predicting exactly where the ATAA will rupture and further provides advice on surgical treatment, thus aid surgical treatment.

1.7 Organization of the thesis

The thesis is organized in seven chapters. Chapter 1 reviews existing scholarship, particularly three different experiment protocols to investigating the mechanical properties of the ATAAs. Existing methods heavily rely on the homogeneity assumption of the aneurysm tissue which would have difficulty to delineate the locally heterogeneous characteristics of the ATAA tissue.

Chapter 2 introduces the experimental setting of the experimental method used in the study. This is an inflation test combined with an advanced analysis method aimed to identify the distribution of heterogeneous properties. The experiment was carried out in the Ecole Nationale Suprieure des Mines de Saint-Étienne. For the sake of completeness, the experimental protocol is briefly described here. The experiment utilized a Digital Image Correlation (DIC) method to record the surface deformation; the reconstruction of surface from point cloud was accomplished in this study and the method is presented. Since this study utilizes the NURBS surface mesh, basis of NURBS surface geometry is reviewed. Next, stress and strain acquisition techniques are presented. Stress acquisition is based on an inverse membrane analysis which is a

method designed to solve the membrane stress based on a given current configuration of the surface and the applied pressure. The membrane theory including kinematics and kinetics is reviewed first and then the inverse membrane finite element method for membrane is introduced. Strain distribution is derived from the extracted NURBS surface.

Chapter 3 shows the full field results including NURBS mesh reconstruction, stress computation from inverse membrane analysis, strain calculation from NURBS interpolation. The membrane assumption is critical to the present work; this assumption is validated numerically using 3D finite element simulations. The result is also presented in this Chapter.

Chapter 4 presents the identified mechanical properties. A hyperelastic material model is used to described the elastic behavior. This model considers anisotropic behavior and the representation of anisotropy is discussed. To evaluate the fidelity of the identified heterogeneous material model, a forward analysis is performed applying the identified pointwise parameters to simulate the inflation deformation of the experiments. Mechanical properties reported in this study are compared to findings from the literature.

Chapter 5 utilizes the identified full field properties to investigate the local mechanical condition at rupture sites. The energy consumption in the tissue was computed. The rupture appears to initiate at the position of the highest strain energy; The most striking finding is that the tissue fractures preferentially in the direction of the highest stiffness, generating orifices that are locally transverse to the

fiber direction. Possible implications of these findings are discussed.

Chapter 6 explores the possible relationship between ATAA strength and elastic properties by using machine learning technique. Three sets of features extracted from tension-strain curves were used to classified the curve at rupture location and non-rupture locations. Based on the importance scores provided by the machine learning, implications of some features were interrogated and and some strong correlations between the strength and the response features were revealed.

Lastly, conclusions and future work are presented in Chapter 7.

CHAPTER 2
EXPERIMENTAL AND COMPUTATIONAL METHODS

Developing experimental protocols that can accurately identify spatial variation in mechanical properties of soft tissues has long been a challenging problem. Existing experiment approaches, for instance, uni-axial and bi-axial tensile tests, heavily rely on the homogeneity assumption. To test heterogeneous material, the most popular strategy is to divide the tissue into multiple samples and test them individually. But still, the heterogeneity assumption is implied and the sample size must to sufficiently small in order to obtain reasonable results. The heterogeneity of the sample to be rather large sized. In this study, a new protocol is developed by integrating the Digital Image Correction (DIC), an inflation test and an inverse stress analysis methodology [81]. This combined method enables the identification of full-field stress, strain and mechanical properties without being limited by the complexity of the tissue heterogeneity. In this section, the technical details of data acquisition, geometry reconstruction, stress and strain computations are presented.

2.1 Inflation test

A bulge inflation test was utilized to deform the ATAA sample to rupture. All samples were collected from patients undergoing elective surgery to replace their ATAAs with a graft in accordance with a protocol approved by the Institutional Review Board of the University Hospital Center of St. Étienne and then tested in Ecole Nationale Suprieure des Mines de Saint-Étienne. The testing procedure is

following. The collected specimen was cut into a square specimen approximately 45 × 45 mm. The thickness of the sample was obtained by averaging the measured values of minimum five locations. To prevent slipping during the test, fatty deposits of the surface were removed as much as possible. The specimen was then clamped in the bulge inflation device and a speckle pattern was spayed on its luminal surface as shown in Figure 2.1. Later, water was infused into the cavity behind the sample with a syringe pump driven at 2 mL/min. During the test, the pressure was measured using a digital manometer (WIKA, DG-10). Images of the inflating specimen were collected using a commercial DIC system (GOM, 5M LT) composed of two 8-bit CID cameras equipped with 50 mm lenses (resolution: 1624 × 1236 px) every 3 kPa until the sample ruptured. After rupturing, the collected images were analyzed using the commercial correlation software ARAMIS (GOM, v. 6.2.0) to determine the three-dimensional displacement of approximately 15,000 points of the surface.

2.2 Geometry reconstruction

2.2.1 NURBS surface element

After obtaining the DIC point clouds of the specimen, a deforming surface that corresponds through all pressurize states was extracted. Non-uniform rational Basis spline(NURBS) representation is chosen to represent the surface since it can maintain C^1 or higher order of continuity easily. NURBS is a parametric model commonly used in computer graphics especially for generating and representing curves and surfaces. A p^{th} order NURBS curve is defined by a knot vector ξ, a set of control points $\{\mathbf{Q}_i\}$,

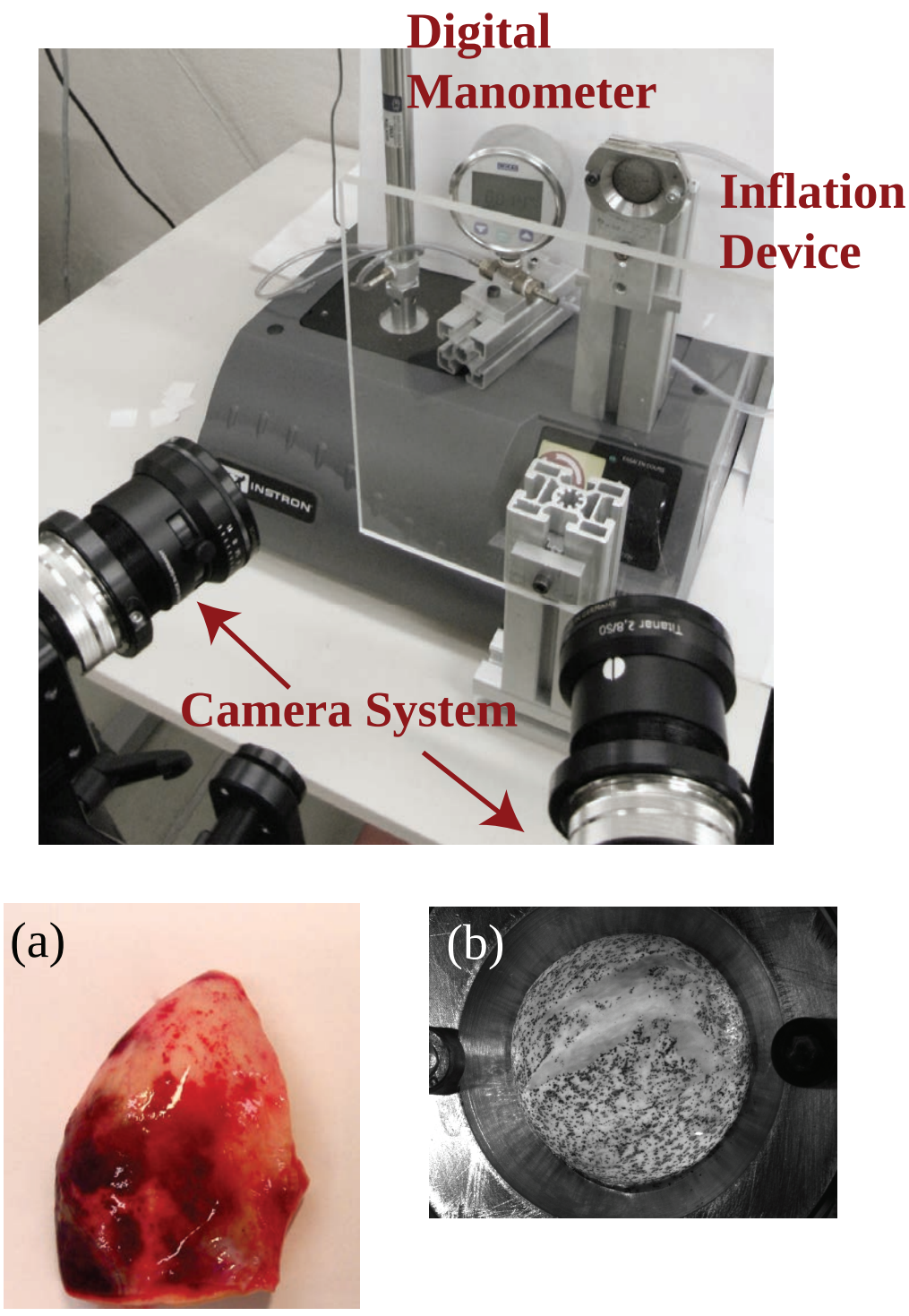

Figure 2.1: Experimental setup and test sample **a** before testing and **b** after rupture (Reproduced with permission from Dr. Stéphan Avril, copyright University Hospital Center of St. Étienne)

corresponding weights $\{w_i\}$. A NURBS curve has the form

$$\mathcal{C}(\xi) = \frac{\sum_{i=1}^{n} B_{i,p}(\xi) w_i \mathbf{Q}_i}{\sum_{i=1}^{n} B_{i,p}(\xi) w_i}, \tag{2.1}$$

or simply $\mathcal{C}(\xi) = \sum_{i=1}^{n} R_i \mathbf{Q}_i$ with $R_i = \frac{B_{i,p}(\xi) w_i}{\sum_{i=1}^{n} B_{i,p}(\xi) w_i}$. $\{B_{i,p}\}$ are the B-spline basis functions, which are completely defined by the knot vector and the degree. The knot vector is a non-decreasing sequences of coordinates in the parametric space, denoted as $\xi = \{\xi_1, \xi_2, \ldots, \xi_{n+p+1}\}$. The B-spline basis functions follow a recursive relation

$$B_{i,p} = \frac{\xi - \xi_i}{\xi_{i+p} - \xi_i} B_{i,p-1} + \frac{\xi_{i+p+1} - \xi}{\xi_{i+p+1} - \xi_{i+1}} B_{i+1,p-1} \tag{2.2}$$

where for zero degree,

$$B_{i,0} = \begin{cases} 1 & if \quad \xi_i \leq \xi < \xi_{i+1} \\ 0 & otherwise \end{cases} \tag{2.3}$$

The knot vector specifies the divisions of the curve in the parametric space. Each non-empty segment $[\xi_1, \xi_{i+1}]$ defines a Bezier segment. The interior knots can repeat up to p times; with each repetition the degree of continuity at that knot reduces by one. The first and last knots can repet $p + 1$ times, in which case the B-spline is interpolatory at the two ends. B-splines and NURBS enjoy many properties desirable for geometric description and analysis. For a complete coverage, see [98].

NURBS surfaces are functions of two parameters mapping to a surface in three-dimensional space. A NURBS surface is constructed by taking the tensor-product of

two NURBS curves, giving the parametric form

$$\mathcal{S}(\xi^1,\xi^2)=\frac{\sum_{i=1}^{n_1}\sum_{j=1}^{n_2}B_{i,p}(\xi^1)B_{j,q}(\xi^2)w_{ij}\mathbf{Q}_{i,j}}{\sum_{i=1}^{n_1}\sum_{j=1}^{n_2}B_{i,p}(\xi^1)B_{j,q}(\xi^2)w_{ij}} \tag{2.4}$$

The control points $\mathbf{Q}_{ij}$ form a $n_1 \times n_2$ net. The rectangle $[\xi_1^1,\xi_{n1+p+1}]\times[\xi_1^2,\xi_{n_2+q+1}^2]$ defines the parametric domain of the NURBS surface, where each non-empty sub-domain $[\xi_i^1,\xi_{i+1}^1]\times[\xi_i^2,\xi_{i+1}^2]$ specifies a Bezier element. Eq. 2.4 can be expressed in the following form:

$$\mathcal{S}(\xi^1,\xi^2)=\sum_{I=1}^{n}N_I(\xi^1,\xi^2)\mathbf{Q}_I, n=n_1\times n_2, \tag{2.5}$$

where the controls points and their interpolation functions are stored in vector form. More details can be found in the literature [6, 25, 33, 98].

2.2.2 NURBS surface reconstruction

Obtaining NURBS meshes started from fitting a template to the DIC point cloud at the first pressure state. The template was a circular domain with a diameter slightly less than that of the point cloud in the first pressure state. As shown in Figure 2.2, the template was parameterized as a 2^{nd} order patch with 22×22 control points, i.e. 20×20 NURBS elements. Since the 2nd order NURBS control points are not physical points on the surface, they cannot be derived directly from the image points. Instead, they are obtained from the point cloud using a moving least square method [7]. The algorithm was summarized in Algorithm 2.1. For each Gauss point in the NURBS mesh, a set of nearest image points in the DIC point cloud were identified based on their distance to the Gauss point in the first pressure state. The radius

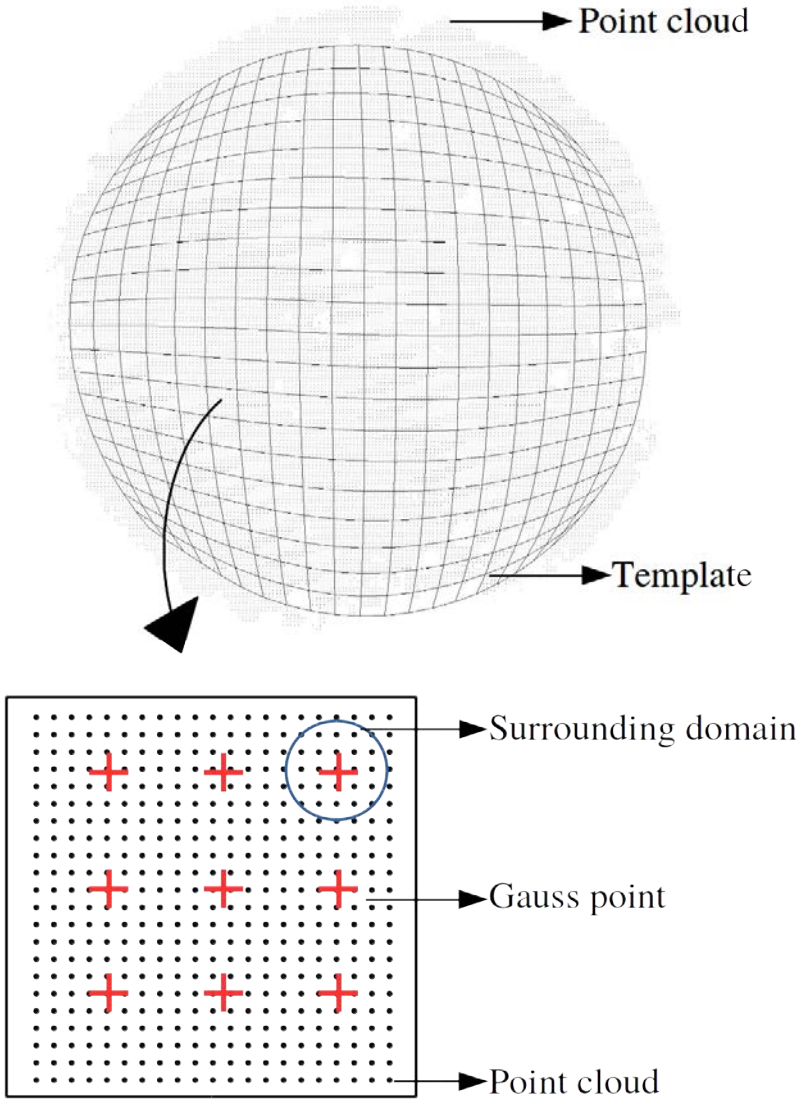

Figure 2.2: NURBS mesh extraction

of the neighboring region was automatically adjusted so that it contained at least six image points. The position of Gauss point, $\mathbf{p}_g$, was computed using an affine interpolation

$$\mathbf{p}_g = \frac{\sum_{\mathbf{p}\in\Omega_g} w_j \mathbf{p}_j}{\sum_{\mathbf{p}\in\Omega_g} w_j} \tag{2.6}$$

where $\mathbf{p}_j$ are the DIC points position vectors within the surrounding domain Ω_g of the Gauss point, weighted by w_j which is the inverse of the distance between $\mathbf{p}_j$ and $\mathbf{p}_g$. Notice that control points are known in the first pressure stage, therefore, the domain Ω_g and the weighting function w_j for each Gauss point were determined in the first pressure stage and used to solve for the control points of the later pressure states. On the other hand, the position of the Gauss point from the NURBS representation is given by

$$\mathbf{x}_g = \sum N_i(u_g, v_g)\mathbf{Q}_i \tag{2.7}$$

where N_i are the NURBS surface basis functions, $\mathbf{Q}_i$ are the control points, and the pair of knot variables, (u_g, v_g) represent a material point. The control points were obtained by solving a global least square problem formulated as

$$\text{Min}(\sum_{\Omega} \parallel \mathbf{x}_g - \mathbf{p}_g \parallel^2) \tag{2.8}$$

The summation goes over the whole domain.

To evaluate the accuracy of the constructed NURBS mesh, the distance deviation between the NURBS surface and the DIC point cloud was computed. For each image point $\mathbf{p}_i$, the closest projection point on the NURBS mesh on the first

pressurized state. This established a one-to-one mapping between an image point and a point on the NURBS surface. The same mapping was used in later pressure states, to establish a corresponding mesh. Points whose closest projection laid outside of the NURBS domain were discarded since they did not involve in mesh computation either. The distance deviation in a pressurized state was then computed by

$$d = \sqrt{\left(\frac{\sum_i \|\mathbf{x}_i - \mathbf{p}_i\|^2}{n}\right)} \tag{2.9}$$

where n is the number of DIC cloud point within the domain, and $\mathbf{x}_i$ is the corresponding point of $\mathbf{p}_i$.

2.3 Pointwise identification method

Pointwise identification method is used for properties determination. The basic procedure is summarized in the Figure 2.3. The characteristic of this method is that the tension and strain data are acquired by different methods. Tension is computed by inverse membrane method and strain is derived from surface deformation for each Gauss point. Mechanical properties are then determined by constitutive regression.

2.3.1 Stress prediction

Stresses for all cases were computed using an inverse membrane analysis. The underlying theory of this method is summarized. Take the advantage of statically determined membrane structure, assumed material properties can be used in the analysis and the computed stress should be well approximate to the true stress in the tissue.

Algorithm 2.1 Moving least square

Input: DIC point cloud and NURBS template mesh

Pre-adjustment Artificially adjust the NURBS template mesh to cover the image point cloud as much as possible

Part I: At zero pressure state

For $i = 1 \leq$ num of elements **do**

For $j = 1 \leq$ num of Gauss points within one element **do**

1. Search surrounding domain and record into an array *dlist*;
2. Calculate w_j for each image point and then $\mathbf{p}_g = \frac{\sum_{\mathbf{p}\in\Omega_g} w_j \mathbf{p}_j}{\sum_{\mathbf{p}\in\Omega_g} w_j}$
3. Calculate $\mathbf{x}_g = \sum N_i(u_g, v_g)\mathbf{Q}_i$
4. Calculate $\| \mathbf{x}_g - \mathbf{p}_g \|^2$ and add its contribution to the global matrix

End

End

Solve least square system $\text{Min}(\sum_\Omega \| \mathbf{x}_g - \mathbf{p}_g \|^2)$ to obtain $\mathbf{Q}_i$ for zero pressure state

Part II: Non-zero pressure states

For $i = 1 \leq$ num of elements **do**

For $j = 1 \leq$ num of Gauss points within one element **do**

1. Use the array *dlist* determined in Part I;
2. Re-calculate w_j for each image point and then $\mathbf{p}_g = \frac{\sum_{\mathbf{p}\in\Omega_g} w_j \mathbf{p}_j}{\sum_{\mathbf{p}\in\Omega_g} w_j}$
3. Calculate $\mathbf{x}_g = \sum N_i(u_g, v_g)\mathbf{Q}_i$
4. Calculate $\| \mathbf{x}_g - \mathbf{p}_g \|^2$ and add its contribution to the global matrix

End

End

Solve least square system $\text{Min}(\sum_\Omega \| \mathbf{x}_g - \mathbf{p}_g \|^2)$ to obtain $\mathbf{Q}_i$ for each pressure state

output: Control points of NURBS mesh

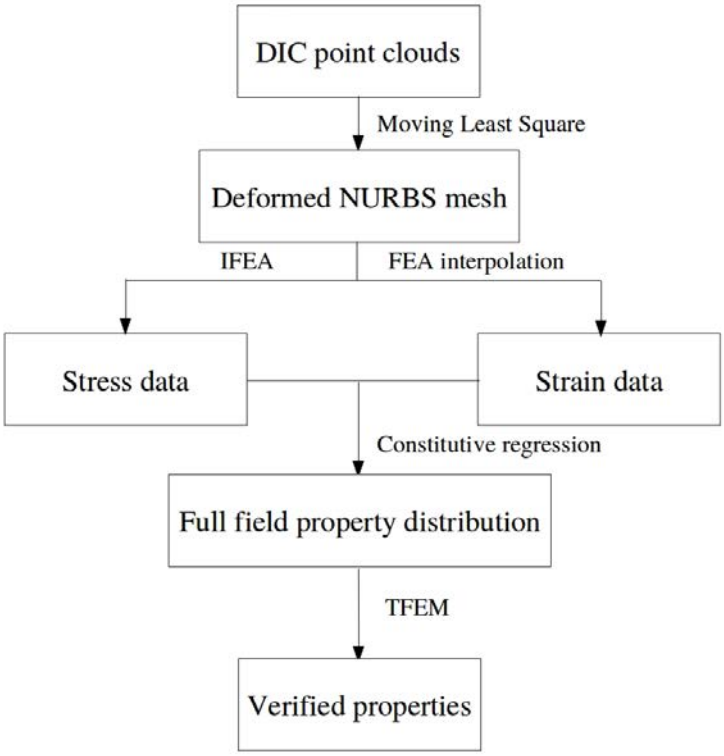

Figure 2.3: Flowchart of pointwise identification

2.3.1.1 Kinematics

Membrane is a 3D thin wall surface which is assumed to be continuous and differentiable. Its thickness h_0 in reference configuration, denoted as Ω_0, is significantly smaller than the other two dimensions. Material point in the reference ($\Omega_0 \in \mathbb{R}^2$) and current configuration ($\Omega \in \mathbb{R}^2$) are parameterized as $\mathbf{X}(\xi^1, \xi^2)$ and $\mathbf{x}(\xi^1, \xi^2)$ where ξ^α ($\alpha = 1, 2$) are surface convective coordinates. The basis vectors (shown in Figure 2.4) in the tangent planes of Ω and Ω_0 can be defined as

$$\mathbf{G}_\alpha = \frac{\partial \mathbf{X}}{\partial \xi^\alpha}, \quad \mathbf{g}_\alpha = \frac{\partial \mathbf{x}}{\partial \xi^\alpha}. \tag{2.10}$$

The dual basis are

$$\mathbf{G}^\alpha = G^{\alpha\beta}\mathbf{G}_\beta, \quad \mathbf{g}^\alpha = g^{\alpha\beta}\mathbf{g}_\beta, \tag{2.11}$$

where $\mathbf{G}^{\alpha\beta}$ can be computed through the inverse of the matrix $\mathbf{G}_{\alpha\beta}$. The components of metric tensor $\mathbf{G}_{\alpha\beta}$ are define as

$$G_{\alpha\beta} = \mathbf{G}_\alpha \cdot \mathbf{G}_\beta. \tag{2.12}$$

Likewise the dual basis vector for the current configuration is defined as $\mathbf{g}^\alpha = g^{\alpha\beta}\mathbf{g}_\beta$ with $g^{\alpha\beta} = \mathbf{g}^\alpha \cdot \mathbf{g}^\beta$. The repeated indices implies summation convention. Then the in-plane deformation gradient $\mathbf{F}$ represented by the basis is

$$\mathbf{F} = \mathbf{g}_\alpha \otimes \mathbf{G}^\alpha, \tag{2.13}$$

and the inverse deformation gradient $\mathbf{F}$ is defined by

$$\mathbf{F}^{-1} = \mathbf{G}_\alpha \otimes \mathbf{g}^\alpha. \tag{2.14}$$

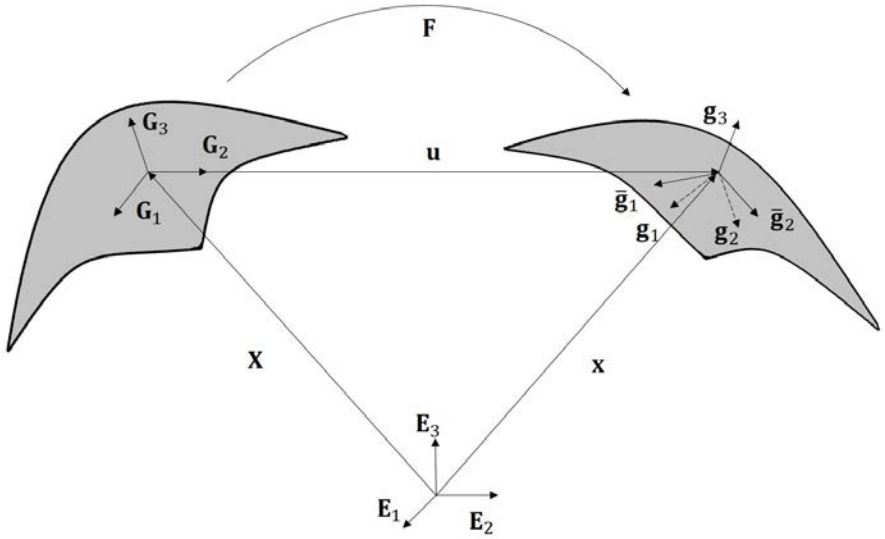

Figure 2.4: Schematic illustration of the kinematic map and base vectors

The Green-Lagrangian deformation tensor $\mathbf{C} = \mathbf{F}^\top \mathbf{F}$ is

$$\mathbf{C} = (\mathbf{G}_\alpha \otimes \mathbf{g}^\alpha)(\mathbf{g}^\beta \otimes \mathbf{G}_\beta) = g_{\alpha\beta}\mathbf{G}^\alpha \otimes \mathbf{G}^\beta. \tag{2.15}$$

The Green-Lagrangian strain tensor $\mathbf{E} = \frac{1}{2}(\mathbf{F}^\top \mathbf{F} - \mathbf{I})$ can be also represented as

$$\mathbf{E} = \frac{1}{2}(g_{\alpha\beta}\mathbf{G}^\alpha \otimes \mathbf{G}^\beta - \mathbf{I}). \tag{2.16}$$

With $\mathbf{I} = G_{\alpha\beta}\mathbf{G}^\alpha \otimes \mathbf{G}^\beta$, the strain tensor is

$$\mathbf{E} = \frac{1}{2}(g_{\alpha\beta} - G_{\alpha\beta})\mathbf{G}^\alpha \otimes \mathbf{G}^\beta. \tag{2.17}$$

2.3.1.2 Kinetics

Since the wall stress σ is assumed to lie along the tangent plane of the surface, it has the form

$$\sigma = \sigma^{\alpha\beta}\mathbf{g}_\alpha \otimes \mathbf{g}_\beta, \sigma^{\alpha 3} = \sigma^{\alpha 3} = \sigma^{33} = 0. \tag{2.18}$$

As the in-plane action is described by the surface tension, which is the stress resultant over the thickness:

$$\mathbf{t} = \int_{-\frac{h}{2}}^{\frac{h}{2}} \sigma dh \approx t^{\alpha\beta} g_\alpha \otimes g_\beta, t^{\alpha\beta} = h\sigma^{\alpha\beta} = t^{\beta\alpha}, \tag{2.19}$$

where h is the thickness of the membrane in Ω. Static equilibrium is governed by the balance equation

$$\frac{1}{\sqrt{g}}(\sqrt{g}t^{\alpha\beta}\mathbf{g}_\alpha)_{,\beta} + p\mathbf{n} = 0, \tag{2.20}$$

and appropriate boundary conditions. In the equilibrium equation, $g = \det(g_{\alpha\beta})$, p is the applied pressure and $\mathbf{n}$ is the outer unit normal vector of the surface.

The advantage of membrane equilibrium system is that the wall stress is static determinacy. The three partial differential equations in equation 2.20 are suffice to determine the three components of the stress in a Neumann boundary value problem. In other words, the wall stress can be fully determined independent of material parameters.

2.3.1.3 Finite element inverse membrane analysis

The inverse deformation problem has been studied by a number of researchers [1, 108, 53, 91, 13, 127]. The inverse element used in this studies was based on the idea of Govindjee et al. [46, 47]. Briefly, the Cauchy wall tension is parameterized by the inverse deformation gradient. A set of nonlinear algebraic equations for the reference positions of the control points are obtained from the weak form. The equations are solved to determine the reference control points. Once the reference configuration

is solved, the deformation is known and the tension in the deformed state can be determined from the constitutive relation. The inverse method has been successfully applied on solving the stress in abdominal aortic aneurysm(AAA), cerebral aneurysm and many other membrane like structures [79, 80, 82, 133, 134, 78, 131].

Defined the undeformed configuration and current configuration as $\mathbf{X}(\xi_1, \xi_2)$ and $\mathbf{x}(\xi_1, \xi_2)$. The inverse displacement is:

$$\mathbf{U} = \mathbf{X} - \mathbf{x} \tag{2.21}$$

Eulerian weak form of inverse membrane is

$$R := \int_\Omega t^{\alpha\beta}\mathbf{g}_\alpha \cdot \delta\mathbf{x}_{,\beta} da - \int_{\partial\Omega} \bar{\mathbf{t}} \cdot \delta\mathbf{x} ds - \int_\Omega p\mathbf{n} \cdot \delta\mathbf{x} da = 0, \tag{2.22}$$

where $\delta\mathbf{x}$ is kinematically admissible variation to the current configuration Ω, $\mathbf{n}$ is the surface normal, $\bar{\mathbf{t}}$ is the surface traction and p is the pressure. By linearizing the weak form relative to the initial configuration, the element stiffness has the form

$$K_{IJ} = \int_\Omega \mathbf{B}_I^\top \mathbb{C}\mathbf{B}_{0J} da, \tag{2.23}$$

where $\mathbf{B}_I$ is the strain-displacement matrix with respect to current configuration

$$\mathbf{B}_I = \begin{bmatrix} N_{I,1}g_1^\top \\ N_{I,2}g_2^\top \\ N_{I,1}g_2^\top + N_{I,2}g_1^\top \end{bmatrix}, \tag{2.24}$$

$\mathbf{B}_{0J}$ is the strain-displacement matrix with respect to reference configuration

$$\mathbf{B}_{0J} = \begin{bmatrix} N_{I,1}G_1^\top \\ N_{I,2}G_2^\top \\ N_{I,1}G_2^\top + N_{I,2}G_1^\top \end{bmatrix}, \tag{2.25}$$

The material tangent tensor $\mathbb{C}$ in components form is

$$C_{\alpha\beta\delta\gamma} = \frac{4}{J}\frac{\partial^2 w}{\partial g_{\alpha\beta}\partial G_{\delta\gamma}} + t^{\alpha\beta}G^{\delta\gamma}. \tag{2.26}$$

To be noticed that this expression possesses only minor symmetry, i.e. $C_{\alpha\beta\delta\gamma} = C_{\beta\alpha\delta\gamma} = C_{\alpha\beta\gamma\delta} = C_{\beta\alpha\delta\gamma}$. The material tangent is in the Voigt form. Note that only the material stiffness appears in the linearization process, and the element stiffness matrix is unsymmetric.

2.3.2 Strain acquisition

Strain computation is straightforward. Recall that we have obtained the NURBS representation of the surface in both the reference and current configurations:

$$\mathbf{X} = \sum_{I=1}^{Nel} N_I(\xi^1, \xi^2)\mathbf{Q}_I, \quad \mathbf{x} = \sum_{I=1}^{Nel} N_I(\xi^1, \xi^2)\mathbf{q}_I, \tag{2.27}$$

where N_I is the NURBS basis function for the I^{th} node, Nel is the total number of nodes in one element. ξ^1, ξ^2 are the convected surface coordinates. The covariant base vectors in reference and current domain are computed by

$$\mathbf{G}_\alpha = \frac{\partial \mathbf{X}}{\partial \xi^\alpha} = \sum_{I=1}^{Nel} \frac{\partial N_I}{\partial \xi^\alpha}\mathbf{Q}_I, \quad \mathbf{g}_\alpha = \frac{\partial \mathbf{x}}{\partial \xi^\alpha} = \sum_{I=1}^{Nel} \frac{\partial N_I}{\partial \xi^\alpha}\mathbf{q}_I. \tag{2.28}$$

Then the Green Lagrangian strain are obtained by using from Equation 2.12 to Equation 2.16

2.3.3 Constitutive regression

After computing tension and strain data, an appropriate constitutive model described the mechanical behavior of the tissue is selected to perform regression algorithms. Constitutive constants, i.e. the elastic property, are then obtained. Con-

stitutive regression is to minimize an objective function, which typically is difference of the mechanical response from numerical model and experiment measure. In this work, the objective function is constructed from the tension results of inverse method and constitutive model. The constitutive regression process will be presented in detail in the later chapter.

CHAPTER 3
GEOMETRY RECONSTRUCTION AND FULL FIELD DATA

Nine samples of seven ATAA sections were collected from patients undergoing elective surgery to replace their ATAAs with graft in accordance with a protocol approved by the Institutional Review Board of the University Hospital Center of St. Etienne. Information on each of the patients' age, gender, and aneurysm diameter (as measured during a pre-surgical CT scan) are shown in Table 3.1.

Table 3.1: Sample Information

Patient	Gender(M/F)	Age	Diameter(mm)	Thickness(mm)
1	M	55	55	2.35
2	F	65	49	1.82
3	F	80	52	1.68
4	M	79	52	1.76
5 (a) & (b)	M	76	58	1.82
6	M	72	51	1.90
7(a)	F	76	65	2.38
7(b)	F	76	65	2.51
mean	-	64.33	49.66	1.80

3.1 Method

3.1.1 Geometry reconstruction

NURBS meshes were reconstructed from DIC image point cloud for all cases. Each NURBS mesh contains 22 $\times$ 22 control points, i.e. 20 $\times$ 20 NURBS elements

and each image has approximate 15000 data points. These image points are evenly spread around a circular surface. Algorithm 2.1 was used to solve the Gauss points of the NURBS mesh. Initially, the radius of the neighboring region for Gauss points was set to a default value, 0.18 mm. It was gradually increased if the number of neighboring points for a Gauss point was less than 6. Position vectors of Gauss points were obtained by solving the moving least square problem using Equation 2.6 – 2.8.

3.1.2 Computation of tension

Taking the reconstructed NURBS mesh of each pressure states as input, the wall tension was computed individually using inverse membrane method described in 2.3.1.3. Benefits from the static determinacy of membrane assumption, the influence of material model is expected to be weak. However, an auxiliary material model is still needed for inverse finite element computation. In this study, a quadratic neo-Hookean material model was implemented. The strain energy function has the form

$$w = \frac{v_1}{2}(I_1 - 2\log J - 2) + \frac{v_2}{4}(I_1 - 2)^2 \tag{3.1}$$

To ensure a robust convergence, material parameters v_1 and v_2 were set to unrealistically high values. For most cases, $v_1 = 2000\text{N/mm}$ and $v_2 = 500\text{N/mm}$.

The control points on the outermost edge of the mesh were fixed. Since the DIC point cloud did not include the physical clamped edge of the specimen, these boundary conditions are only approximate. Imposing displacement boundary condition will compromise the static determinacy. But the influence of boundary condition

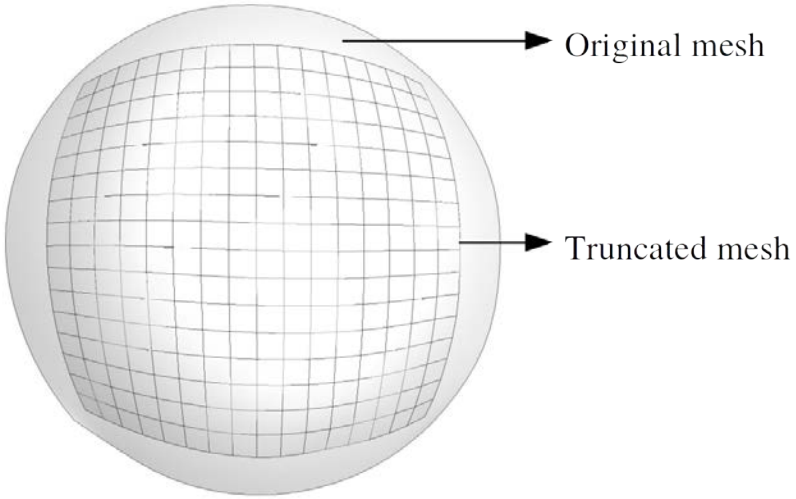

Figure 3.1: Truncated mesh demonstration

is typically confined to a boundary layer [81, 75, 132, 22]. Here, the outer ring of elements were taken as the boundary layer as shown in Figure 3.1. Although the tension and strain were computed in these elements, the constitutive regression described in the later sections do not include them.

3.1.3 Computation of strain

Surface strains were computed with the aid of NURBS curvilinear coordinate system. The base vectors ($\mathbf{G}_\alpha, \mathbf{G}^\alpha, \mathbf{g}_\alpha, \mathbf{g}^\alpha$) and metric tensor components ($G_{\alpha\beta}$, $G^{\alpha\beta}$, $g_{\alpha\beta}$, $g^{\alpha\beta}$) of a material point on the NURBS mesh were approximated using Equation 2.27 – 2.28. Then the surface Cauchy-Green deformation tensor, $\mathbf{C}$, and the Green-Lagrangian strain tensor $\mathbf{E}$ were computed by Equation 2.15 and 2.16 respectively.

3.2 Results

3.2.1 Geometric Reconstruction

Using the experimental DIC point cloud, a NURBS mesh was generated for each ATAA sample. Figure 3.2 shows the extracted NURBS mesh at the last pressure state of each sample superimposed on the experimental DIC point cloud at the same pressure. Using Equation 2.9 the distance deviation for each pressure stage was computed. The deviation changes for all cases versus pressure state are shown in Figure 3.3. It is easy to notice that the values are relatively larger at low pressures while as the tissue is inflated the distance deviation rapidly decreases and stabilizes after 30kPa. Overall, the distance deviations are at the order of 0.01 which is very small. Domain average of distance deviation from the last pressure state for each case is also provided in Table 3.2. The deviations are on the order of a few to a few tens of microns, comparable to the DIC accuracy.

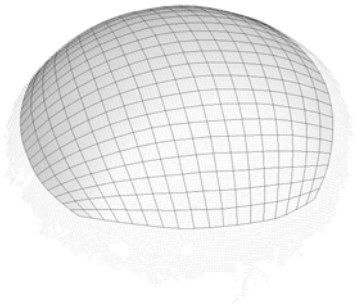

(a) Patient 1

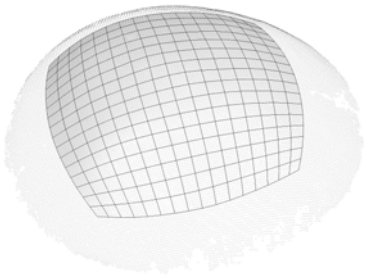

(b) Patient 2

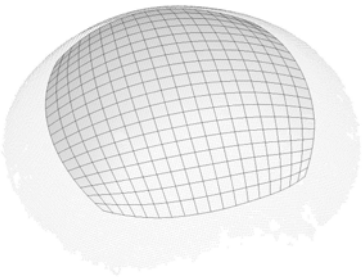

(c) Patient 3

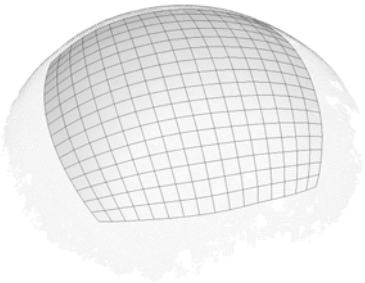

(d) Patient 4

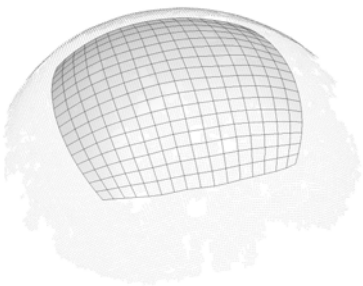

(e) Patient 5(a)

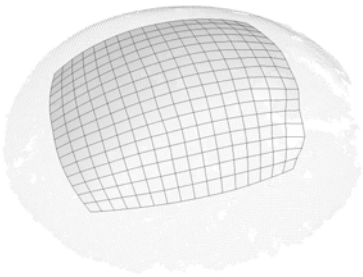

(f) Patient 5(b)

Figure 3.2: Mesh fitting of all patients

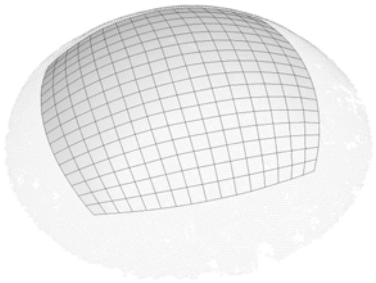

(g) Patient 6

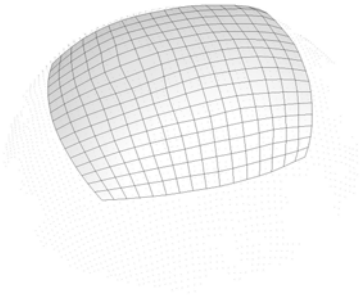

(h) Patient 7(a)

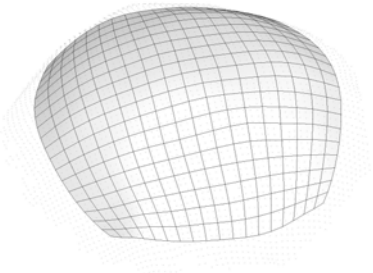

(i) Patient 7(b)

Figure 3.2: Mesh fitting

Table 3.2: Size of domain and surface deviation

Patient	Radius of the NURBS domain(mm)	Deviation(mm)
1	10.00	0.001±0.001
2	11.50	0.002±0.001
3	11.00	0.014±0.003
4	12.00	0.014±0.004
5(a)	10.00	0.024±0.006
5(b)	11.00	0.028±0.008
6	12.00	0.016±0.005
7(a)	10.50	0.036±0.016
7(b)	12.00	0.008±0.003

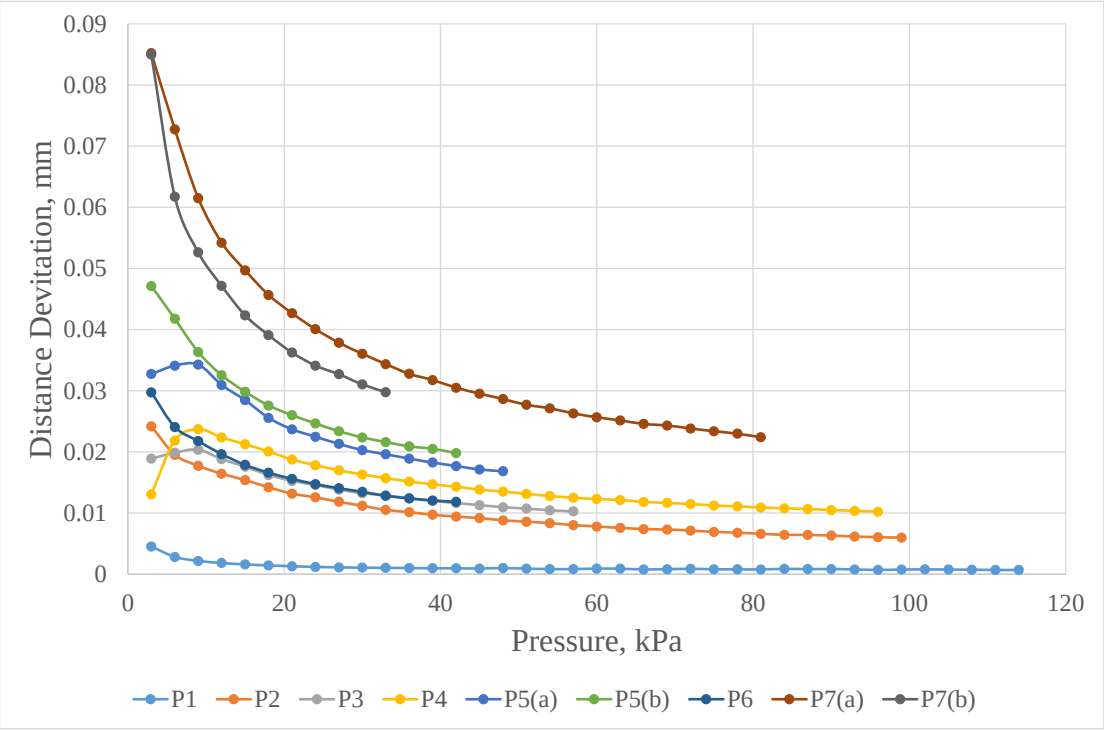

Figure 3.3: Distance variation

3.2.2 Tension and strain

Figure 3.4 and Figure 3.5 show the distributions of the magnitude of the Cauchy wall tension and Green-Lagrangian strain at the pressure state just preceding rupture respectively. Because the distribution of wall tension and strain remained similar throughout the inflation of the specimen. Stress and strain concentrations are easily observed. The highest value of the wall tension mostly occurs at the apex of the sample. Exceptions, such as Patient 5(b) and 7(b) whose the peak tension values located on the left edge, were caused by the boundary conditions applied in the inverse membrane simulation. Compared to stress concentration, location of the peak strain values locate on the edges mostly.

The maximum and mean values of the magnitude of the Cauchy wall tension and the magnitude of the Green-Lagrangian strain at the pressure state preceding rupture are listed in Table 3.3. Although the maximum wall tension varies significantly from patient to patient, the maximum strain at failure appears to be clustered around 0.3. Patient 1 has a significantly higher strain than the others. The possible reason is the large difference of age between Patient 1 (age = 55 yr) and the others(mean age = 65.5 yr).

3.3 Membrane validation

The surface tension obtained in this study hinges on the assumption that the sample can be described as a membrane. In mechanics, a membrane is defined as a thin structure that offers negligible resistance to bending. That means that

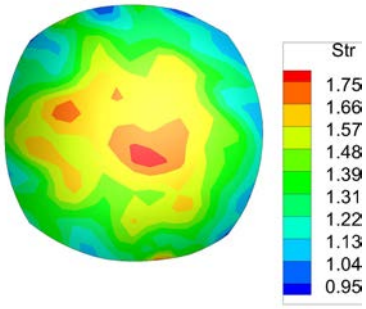

(a) Patient 1

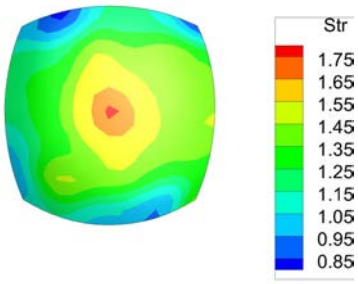

(b) Patient 2

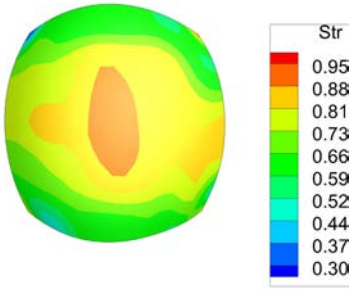

(c) Patient 3

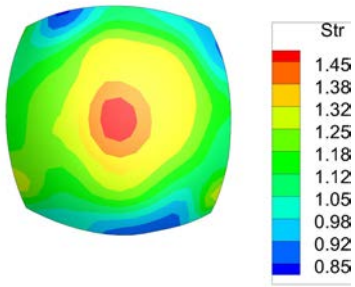

(d) Patient 4

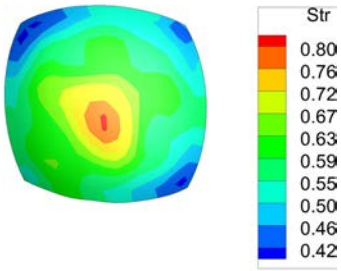

(e) Patient 5(a)

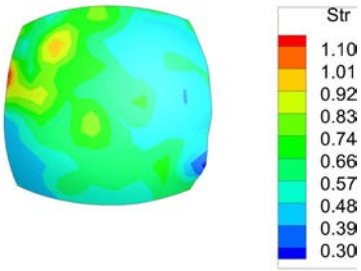

(f) Patient 5(b)

Figure 3.4: Tension (N/mm)

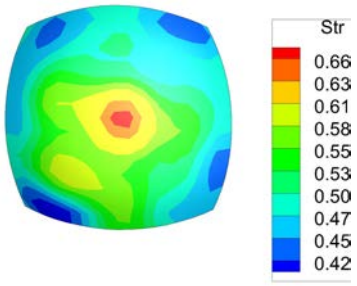

(g) Patient 6

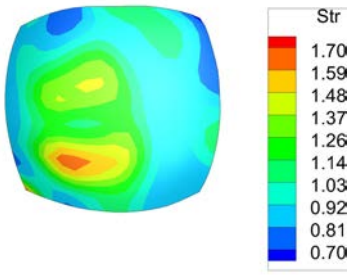

(h) Patient 7(a)

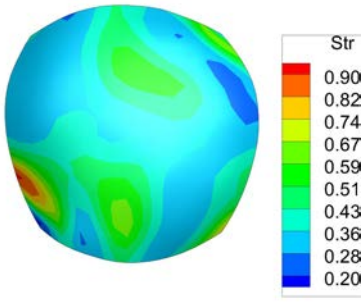

(i) Patient 7(b)

Figure 3.4: Tension (N/mm)

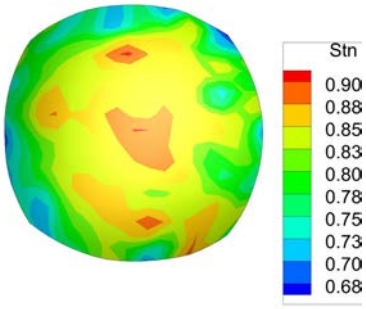

(a) Patient 1

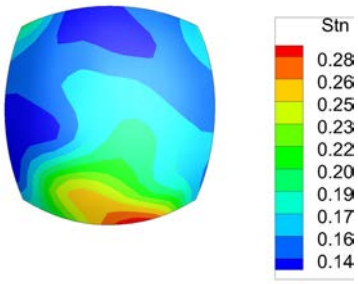

(b) Patient 2

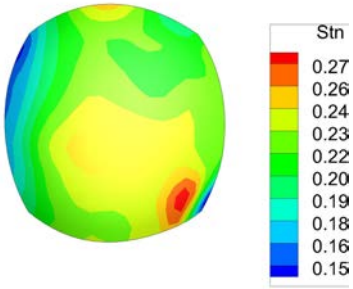

(c) Patient 3

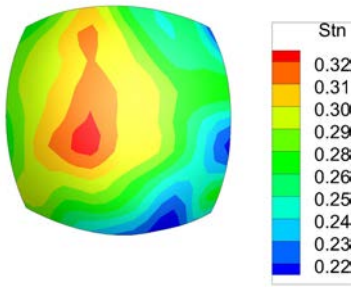

(d) Patient 4

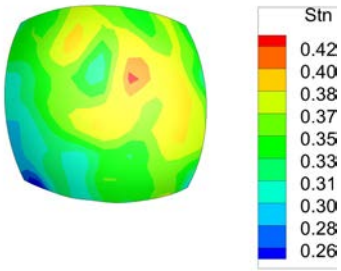

(e) Patient 5(a)

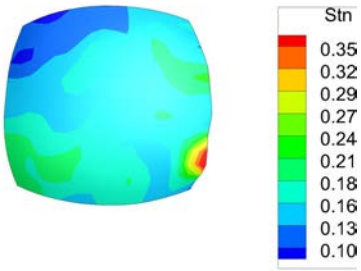

(f) Patient 5(b)

Figure 3.5: Strain

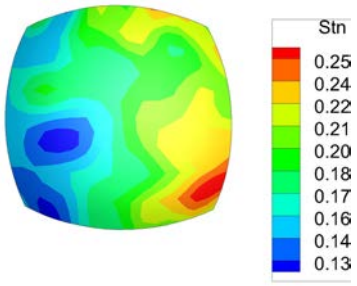

(g) Patient 6

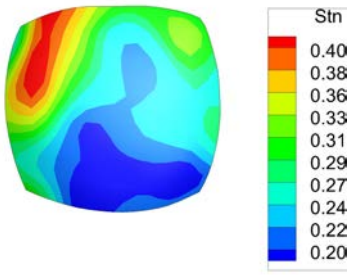

(h) Patient 7(a)

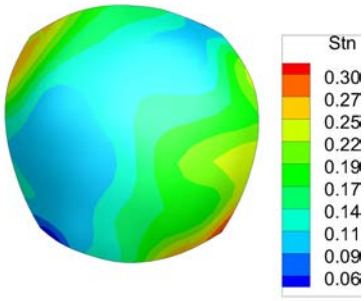

(i) Patient 7(b)

Figure 3.5: Strain

Table 3.3: Tension and strain magnitude in the highest pressure state

Patient	Pressure(kPa)	Tension		Strain	
		Maximum(N/mm)	Mean(N/mm)	Maximum	Mean
1	117	2.05	1.34±0.22	0.95	0.80±0.06
2	99	1.80	1.26±0.20	0.31	0.17±0.04
3	57	0.94	0.74±0.10	0.28	0.22±0.02
4	96	1.51	1.14±0.15	0.33	0.27±0.03
5(a)	48	0.82	0.56±0.08	0.44	0.34±0.03
5(b)	42	0.90	0.57±0.12	0.23	0.16±0.03
6	42	0.69	0.50±0.05	0.27	0.18±0.03
7(a)	81	2.06	1.02±0.27	0.43	0.26±0.06
7(b)	33	0.99	0.41±0.13	0.33	0.15±0.06

the effects of bending moments and transverse shears are neglected and will lead to a considerable simplification for mechanical analysis. It has been shown that most biological membranes can be modelled mechanically via a continuum theory of membranes under many conditions [62]. However, the membrane theory applies when ratio of the longitudinal dimension to the thickness varies between 80 and 100 [120]. Since the ratios of diameter to thickness of our samples fall out of the theory limits, it is necessary to verify whether the membrane assumption if valid.

3.3.1 Comparing model description

To validate the membrane assumption, a bulge inflation test was simulated in ABAQUS (v. 6.9) to replicate the experimental loading at low pressures, where the membrane assumption is most likely to be compromised. The nodes on the perimeter of the circular plate were fixed, again to mimic the experimental conditions. The resulting displacements from the ABAQUS model on the top surface were used as

inputs to inverse membrane approach. The stress fields from the ABAQUS model were used as the reference stress fields for comparison with the inverse membrane solution.

3.3.2 Abaqus model and results comparing

In ABAQUS, two models of a circular plate with a diameter of 30 mm were created. In the first model, the circular plate had a thickness of 2.40 mm, which is slightly larger than the thickest specimen tested (t=2.38 mm). In the second model, the plate was given a thickness of 2 mm, representing the average thickness of the specimens tested in this study. The diameter of the plate, 30 mm, matches the size of the clamped area during inflation test. The plate was meshed using continuum shell elements (SC8R) with 2 elements through the thickness and a total of 2970 nodes and 1882 elements. The perimeter nodes on the mid-line of the circular plate were fixed (Fig. 3.6). The circular plate was modeled as a neo-Hookean solid (c_1 = 0.04 Pa). Similar to the experimental protocol, four different levels of inflation were considered 100, 125, 150, and 170 kPa. Note that much higher pressures were needed due to the small shear stiffness used to model the specimen.

To mimic the experimental case, only the data from a 20 mm diameter region in the center of the plate was used as the input for the inverse analysis (Fig. 3.6(b)). Following the same approach used for experimental data in the manuscript, the principal Cauchy wall tensions (N/mm), denoted P_1 and P_2, were computed in the FEA analysis and the inverse approach. The wall tensions from the membrane model were

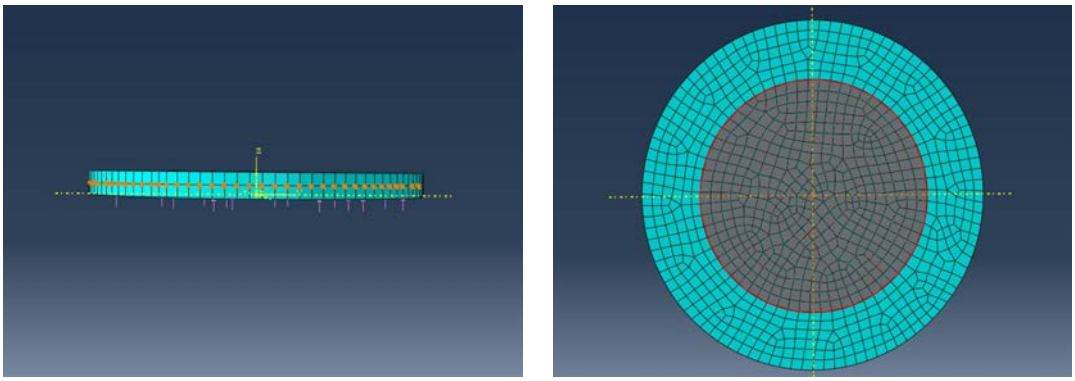

(a) Side view (b) Top view

Figure 3.6: Images of the FEA benchmark model in ABAQUS (v. 6.9). Figure 3.6a is the side view of the model showing pressure loading and fixed boundary condition at the plate mid-line. Figure 3.6b is the top view of the model where the elements in grey were used in the inverse analysis and those in blue were discarded.

compared to the benchmark FE solution for a pressure of 125 kPa and a thickness of 2.4 mm (Figure 3.7). Clearly, the stress fields produced are very similar. The maximum error between the FE solution and the inverse membrane solution is 14% and occurs near the boundary. The increase decrease in thickness does not markedly change the maximum error with the value only decreasing to 12%.

The data collected at low pressures ($p < 15$ kPa) were not used to perform the material identification. Experimentally at 15 kPa, the maximum out-of-plane displacement, H, was roughly 4 mm. Comparing this to the results from the computation model, Fig. 3.8, this likely results in an error of approximately 12% on the stress calculation. Further, as the pressure level and out of plane displacement in-

creases the error dramatically decreases approaching 5% at 5 mm of deformation. For comparison, the average maximum deformation for the samples tested was 5.7 mm. These results suggest that for early stages (15 kPa $<$ p $<$ 30 kPa), the error is around 10% and then rapidly decline to less than 5%. The material parameter identification is later driven by the high pressures states. These results suggest that the membrane assumption is a reasonable approximation for computing stresses especially when the pressure is higher than 15 kPa. At low pressures, when the out-of-plane displacement is small, the membrane stress deviates from the benchmark solution by more than 15%.

3.4 Discussion

By combining DIC, bulge inflation testing, and inverse membrane analysis, we are able to capture the deformation of the ATAA tissue and obtain the stress, strain at every Gauss point. The NURBS mesh was reconstructed to perform isogeometric analysis. This geometry description method intrinsically leads to a smooth surface reconstruction and further produces smooth stress and strain field. As can be seen in Figure 3.2, the reconstructed NURBS meshes overlap with the DIC point cloud visually at the last pressure states. In Figure 3.3, the higher distance deviations in the geometric reconstruction at pressures below 30 kPa are believed occur due to a non-smooth surface geometry. As the ATAA is inflated, the specimen surface becomes more smooth. Therefore, the fitting quality is getting better. Tension results calculated by inverse finite element presented in Figure 3.4 directly show that the

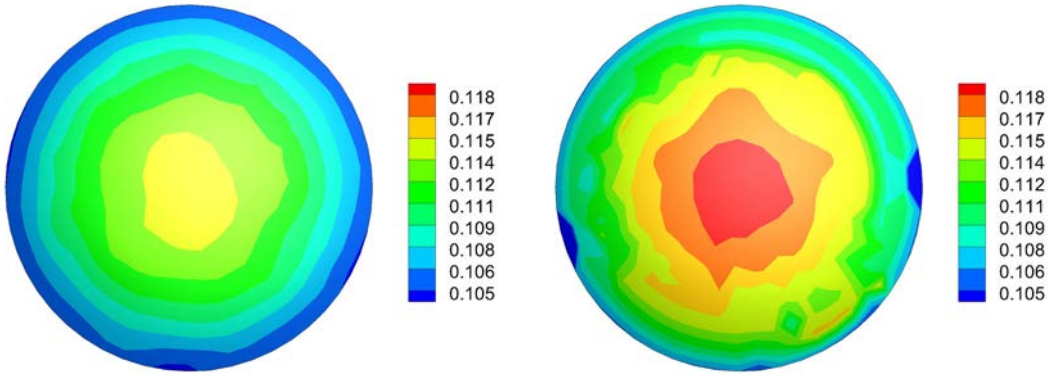

(a) Abaqus: P_1 (b) Inverse: P_1

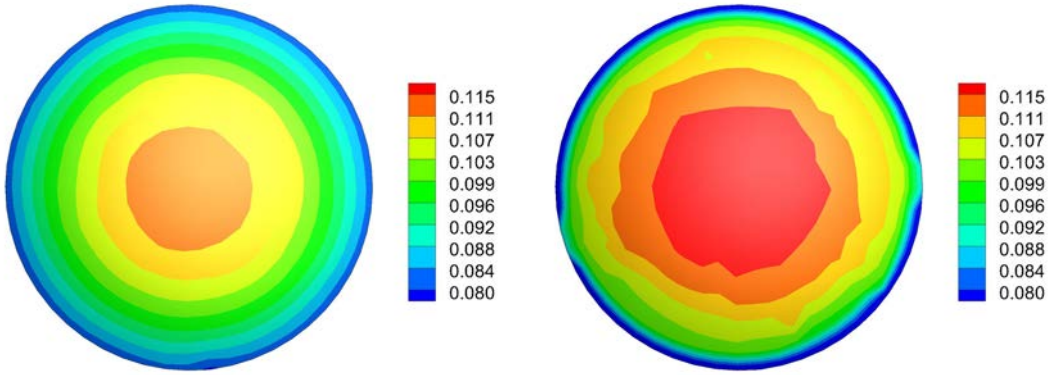

(c) Abaqus: P_2 (d) Inverse: P_2

Figure 3.7: Stress distribution over the central region extracted from the FEA model in N/mm for an applied pressure of 125 kPa and a model thickness of 2.4 mm. (a) Principal stress, P_1, from ABAQUS. (b) Principal stress, P_1, from inverse membrane solution. (c) Principal stress, P_2, from ABAQUS. (d) Principal stress, P_2, from inverse membrane solution.

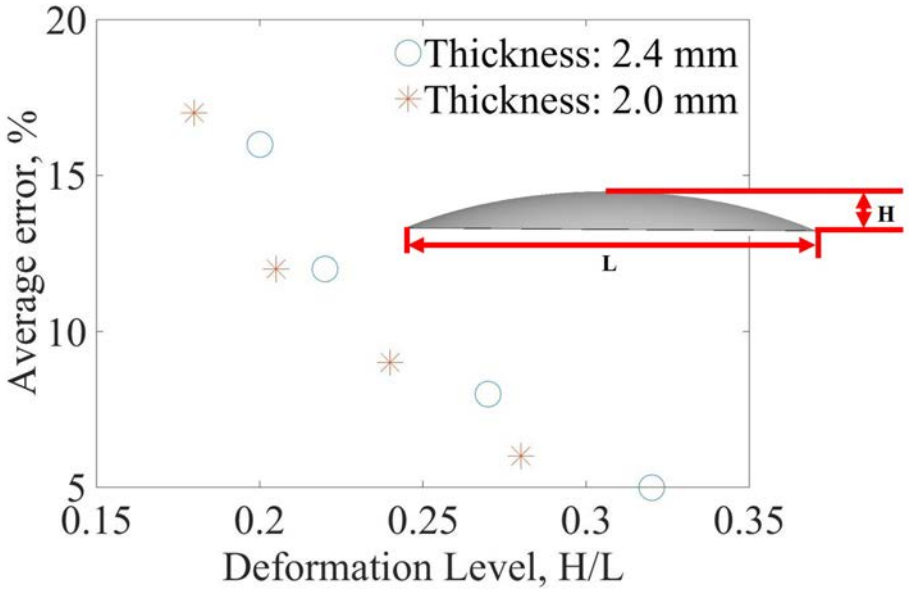

Figure 3.8: Stress percent error between the FE solution and the inverse membrane solution on P_1 as a function of deformation level. The deformation level is the ratio of the out-of-plane displacement to the specimen diameter.

tension is not evenly distributed in the tissue and the peak stress does not necessarily occurs in the center. In some previous studies using bulge inflation tests, the membrane stresses were frequently identified using the Laplace equation which requires that the membrane is axisymmetric. Investigators usually idealized the deformed to fulfilling the premise of the law [90, 20, 85]. However, during our bulge inflation tests, the ATAA did not maintain an axisymmetric shape. Hence, the employed numerical method is necessarily needed in this study.

There are several limitations to the method. First, a bulge inflation test can only produce a limited variety of deformations. Generally, it records the resulting deformation from a specified pressure and can not alter the strain pattern otherwise. It is unclear if the material properties identified from the bulge inflation test can be directly used to predict the response of the ATAA in conventional testing, such as uni-axial tension. Second, the applied membrane assumption ignores the structural information of ATAA. The ATAA tissue is composed of three different layers; but in modeling, the tissue is treated as a membrane and the layers information was discarded. The stress and strain are therefore representative of the combined response of the three layers. Despite these limitations, the approach provides a novel method that can characterize the complex heterogeneity observed in ATAA.

CHAPTER 4
LOCAL MECHANICAL PROPERTIES

Ascending thoracic aorta has complex microstructure. It is composed of three distinct layers, the intima, the media and the adventia. The micro-structure of ATAA naturally results in highly non-linear and heterogeneous characteristics. The full field stress strain data obtained from the experiments enabled an characterization of the distribution of heterogeneous properties. This chapter presents the property results and a computation validation of the identified properties.

4.1 Method

4.1.1 Constitutive theory

The constitutive equation for hyperelastic membrane is represented by a strain energy function, i.e. energy density per unit area. It can be established generally in two ways. If the 3D strain energy function of the material is known, the surface energy function can be simply derived by reduction. The other one is to hypothesize the function depends on the surface deformation gradient, and characterize the specific form by experiments[48, 113]. The later approach is the one followed by this work. The strain energy function is given a function of the deformation gradient $\mathbf{F}$. This function can be also expressed without loss in generality in terms of the first and second principal invariants of $\mathbf{C} = \mathbf{F}^T\mathbf{F}$. The artery tissue is a layered composite material. Its collagen fiber content directly result in anisotropic response to external loading. Holzapfel et al. suggested an additive decomposition of the isochoric strain-

energy function w for fiber reinforced tissue into a part associated with the isotropic beavior of the non-collagenous matrix material and another one associated with the anisotropic behavior of the collagen fiber network [60]. In this spirit, a modified form of the strain energy density proposed by Gasser, Ogden, and Holzapfel (GOH) was used

$$w = \frac{\mu_1}{2}\left(\mathrm{I}_1 - \ln\left(\mathrm{I}_2\right) - 2\right) + \frac{\mu_2}{4\gamma}\left(\mathrm{e}^{\gamma(\mathrm{I}_k-1)^2} - 1\right) \tag{4.1}$$

where $\mathrm{I}_1 = \mathrm{tr}\,\mathbf{C}$ and $\mathrm{I}_2 = \det\mathbf{C}$ are the principal invariants of the Cauchy-Green deformation tensor and $\mathrm{I}_\kappa = \mathbf{C} : (\kappa\mathbf{I} + (1-2\kappa)\,\mathbf{M}\otimes\mathbf{M})$ is a compound invariant consisting of isotropic and anisotropic contributions[44]. The first term accounts for the isotropic behavior of the matrix which includes the ground substance and elastin fibers while the second term represents the contribution of the collagen fiber network. In the compound invariant I_κ, the unit vector $\mathbf{M} = \cos\theta\,\mathbf{G}_1 + \sin\theta\,\mathbf{G}_2$ defines the orientation of the collagen fibers in the reference configuration while κ characterizes the dispersion of the collagen fibers. The dispersion parameter, κ, varies from 0 to $\frac{1}{2}$. When $\kappa = 0$ all of the collagen fibers are perfectly aligned in the direction $\mathbf{M}$. The distribution of collagen fibers has no preferential direction (isotropic) when $\kappa = \frac{1}{2}$. In Eq. 4.1, the parameters μ_1 and μ_2 are the effective stiffnesses of the matrix and collagen fibers, respectively, both having dimensions of force per unit length. The parameter γ is a non-dimensional parameter that governs the tissue's strain stiffening response.

The second Piola-Kirchhoff wall tension, $\mathbf{S}$, is written as

$$\mathbf{S} = 2\frac{\partial w}{\partial \mathrm{I}_1}\mathbf{1} + 2\frac{\partial w}{\partial \mathrm{I}_2}\mathrm{I}_2\mathbf{C}^{-1} + 2\frac{\partial w}{\partial \mathrm{I}_\kappa}(\kappa\mathbf{I} + (1-2\kappa)\mathbf{M}\otimes\mathbf{M}). \quad (4.2)$$

Substituting Eq. 4.1 into Eq. 4.2 one finds

$$\mathbf{S} = \mu_1(\mathbf{I} - \mathbf{C}^{-1}) + \mu_2\, \mathrm{e}^{\gamma(\mathrm{I}_\kappa - 1)^2}(\mathrm{I}_\kappa - 1)(\kappa\mathbf{I} + (1-2\kappa)\mathbf{M}\otimes\mathbf{M}) \quad (4.3)$$

noting that the second Piola-Kirchoff wall tension is related to the Cauchy wall tension via $\mathbf{t} = \frac{1}{\sqrt{\mathrm{I}_2}}\,\mathbf{F}\,\mathbf{S}\,\mathbf{F}^{\mathrm{T}}$.

4.1.2 Parameter identification

The Gauss point values of the model parameters μ_1, μ_2, γ, κ, and θ were determined by minimizing the objective function

$$f = \Sigma_{i=1}^{n} \|\mathbf{S}_i^{inv} - \mathbf{S}_i^{mod}\|^2 \quad (4.4)$$

where $\mathbf{S}_i^{inv}$ is the 2nd Piola-Kirchhoff stress computed from the inverse analysis and $\mathbf{S}_i^{mod}$ is the stress modeled by Eq. 4.3. The subscript i indicates the pressure state and n is the total number of states. The nonlinear regression problem is solved in MATLAB (MathWorks, v. 7.14). The parameters were confined to $\mu_1 \in (0.0, 10.0)$, $\mu_2 \in (0.0, 10.0)$, $\gamma \in (0.0, 100.0)$, $\kappa \in [0.0, 0.5]$, $\theta \in [0, \pi]$. To ensure that the solutions were not affected by the initial guess of parameters, three sets of initial guesses were used. Since the parameters θ and κ are tightly bound, the upper bound, lower bound, and middle values were used. Randomly chosen values between 0.5 to 1.0 were tested for μ_1 and μ_2. Results show that the parameters identification was largely insensitive to initial guesses.

The coefficient of determination, R^2 was calculated to evaluate the regression quality. The definition of the coefficient of determination is

$$R^2 = 1 - \frac{SS_{res}}{SS_{tot}} \tag{4.5}$$

where $SS_{res} = \sum_i^n (y_i - f_i)^2$ and $SS_{tot} = \sum_i^n (y_i - \bar{y})^2$. y_i and f_i represent the experiment and predicted values respectively. n is the total number of the data point and $\bar{y}$ is the the mean value of experiment values.

4.2 Results

4.2.1 Material Parameters

The distributions of the material parameters, μ_1, μ_2, γ, κ and θ are plotted in Figure 4.1, 4.2, 4.3, 4.4, 4.5, respectively and they clearly display a heterogeneous distribution. The parameter μ_1 displayed the sharpest changes in value, while the parameters μ_2, κ, γ changed more gradually. Not surprisingly, the values of μ_2 are an order of magnitude larger than μ_1 reflecting the difference in stiffness between the collagen fibers and the ground matrix. The non-uniform distribution of κ suggests that there are regional differences in the fiber organization. For some cases, the values of κ are approximately 0.5 in the center indicating that the tissue as a whole is only moderately anisotropic. The angle θ that defines the primary orientation of the collagen fibers is plotted. Note that θ is defined locally relative to the local basis vector $\mathbf{G}_1$ which is parallel to the horizontal meshlines. Keep in mind that when the value of κ is approximately 0.5, the fiber orientation θ is irrelevant since there is no

Table 4.1: Mean values of material properties

Patient	μ_1(N/mm)	μ_2(N/mm)	γ	κ	θ(rad)
1	0.12E-01±0.11E-01	0.27±0.10	1.61±0.35	0.40±0.48E-01	1.56±0.60
2	0.56E-02±0.94E-02	0.91±0.36	4.90±2.29	0.39±0.54E-01	1.64± 0.54
3	0.34E-02±0.62E-02	1.11±0.21	13.86±3.30	0.42±0.36E-01	1.76±1.03
4	0.20E-02±0.57E-02	0.87±0.22	12.19±2.68	0.42±0.49E-01	1.39±0.84
5(a)	0.22E-02±0.35E-02	0.28±0.07	7.75±2.07	0.41±0.39E-01	1.39±0.71
5(b)	0.69E-02±0.11E-01	1.75±0.96	23.94±10.62	0.37±0.72E-01	1.54±0.66
6	0.28E-02±0.63E-02	1.37±0.22	12.36±5.95	0.43±0.36E-01	1.56±0.73
7(a)	0.51E-02±0.11E-01	1.10±0.69	15.19±6.22	0.37±0.76E-01	1.74±0.70
7(b)	0.15E-01±0.30E-01	1.83±1.23	23.24±15.71	0.30±0.13	1.77±0.71
Population mean	5.30E-02	0.94	11.40	0.40	1.50

preferred fiber direction. Domain average values are summarized in the Table 4.1. A quick observation is the large properties difference not only exists between patients but also within a same patient. For instance, μ_1, μ_2, γ, κ and θ for patient 5(a) and 5(b) are 0.22E-02, 0.28, 7.75, 0.41, 1.39 and 0.69E-02, 1.75, 23.94, 0.37, 1.54.

To assess the quality of local regression, the least square R^2 values were calculated at every Gauss point. The average values for each case ranges from 0.92 to 0.99. It is evident that the material model fitted the stress strain data very well.In all cases, the model fits the data very well in middle-higher pressure regime. In low pressure states there are small yet visible deviations and that properly due to the bending effect as discussed in the previous section.

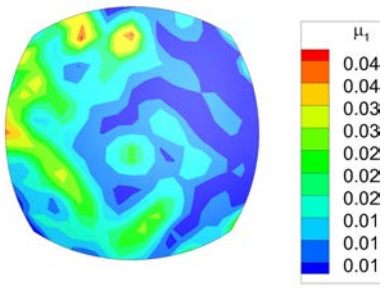

(a) Patient 1

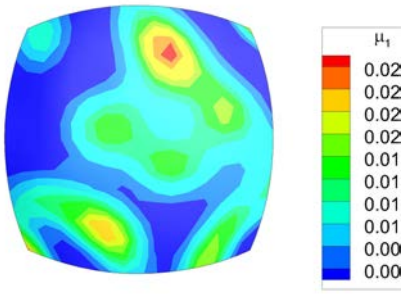

(b) Patient 2

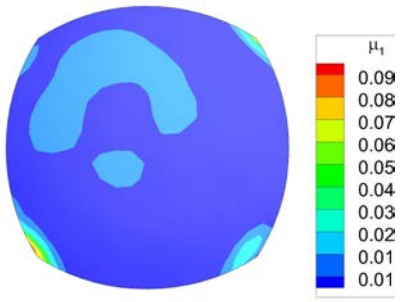

(c) Patient 3

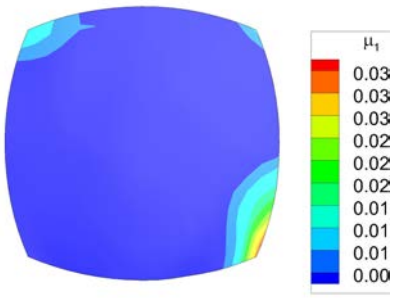

(d) Patient 4

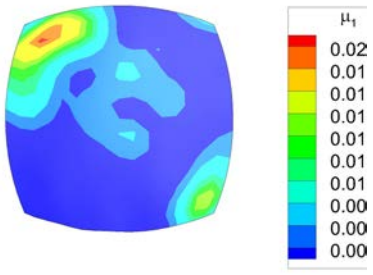

(e) Patient 5(a)

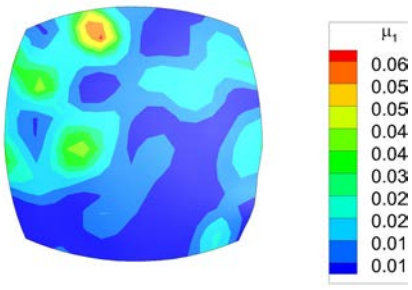

(f) Patient 5(b)

Figure 4.1: μ_1 (N/mm) values of all patients

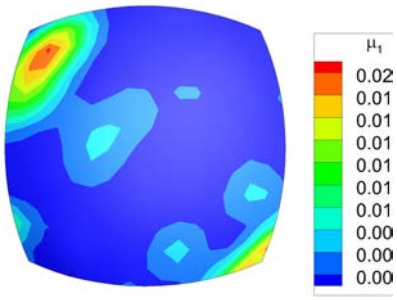

(g) Patient 6

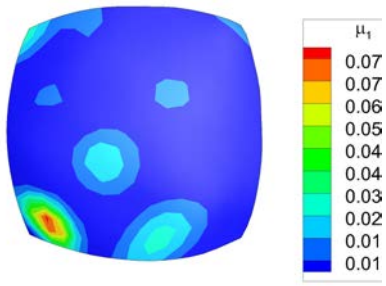

(h) Patient 7(a)

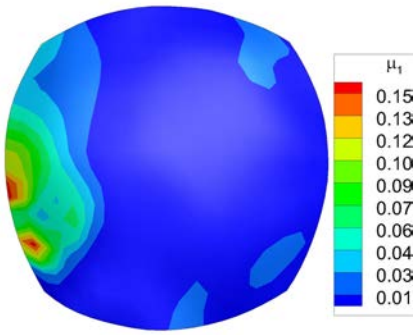

(i) Patient 7(b)

Figure 4.1: μ_1 (N/mm) values of all patients

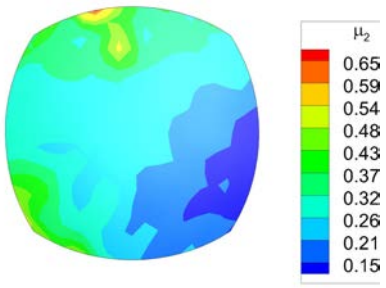

(a) Patient 1

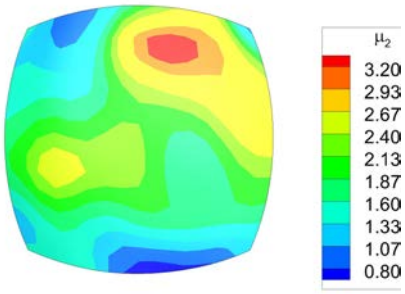

(b) Patient 2

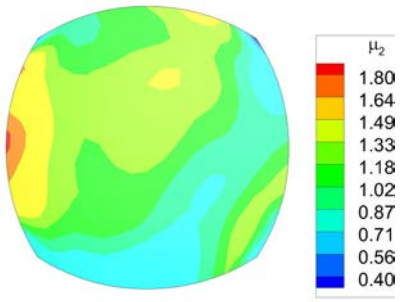

(c) Patient 3

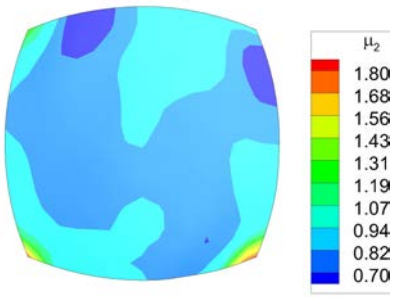

(d) Patient 4

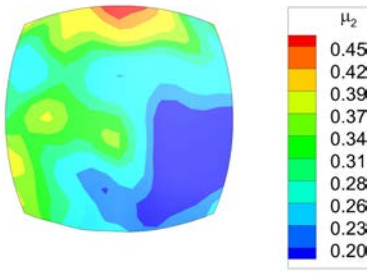

(e) Patient 5(a)

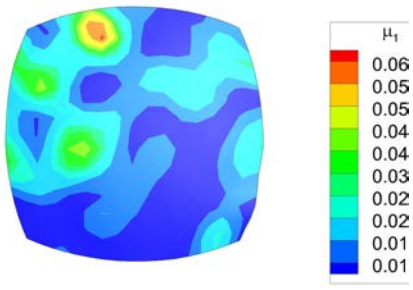

(f) Patient 5(b)

Figure 4.2: μ_2 (N/mm) values of all patients

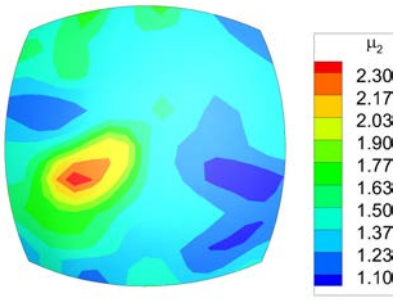

(g) Patient 6

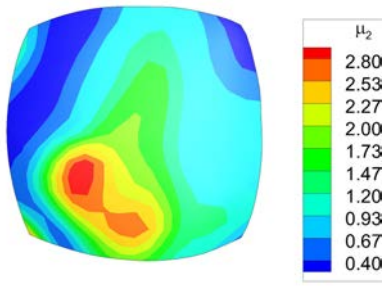

(h) Patient 7(a)

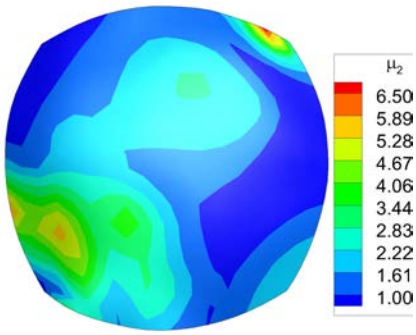

(i) Patient 7(b)

Figure 4.2: μ_2 (N/mm) values of all patients

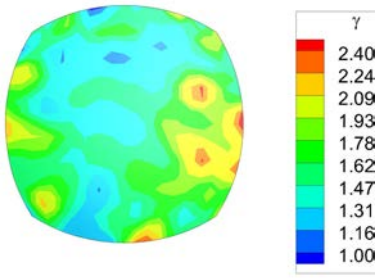

(a) Patient 1

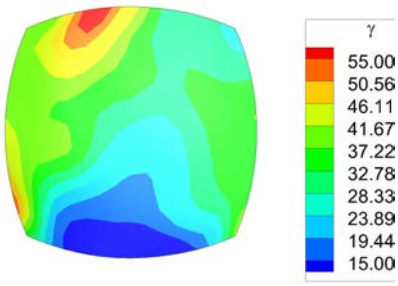

(b) Patient 2

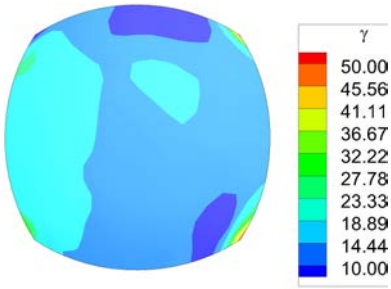

(c) Patient 3

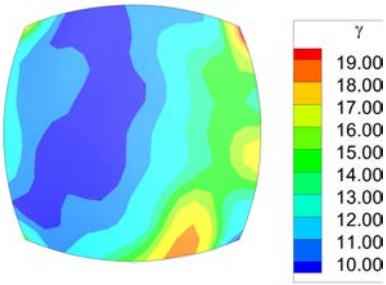

(d) Patient 4

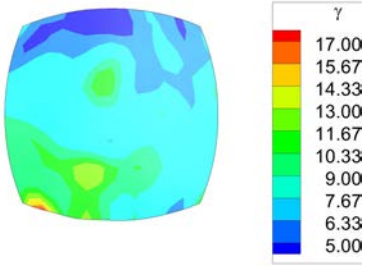

(e) Patient 5(a)

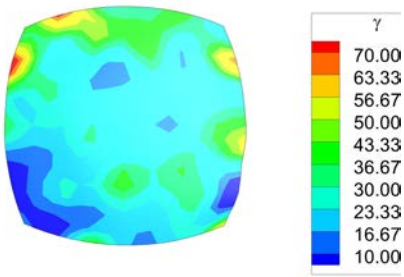

(f) Patient 5(b)

Figure 4.3: γ values of all patients

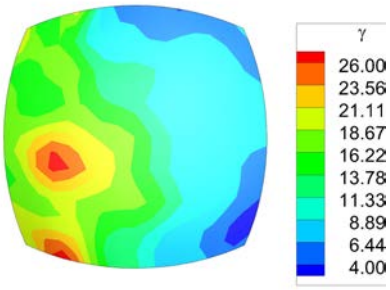

(g) Patient 6

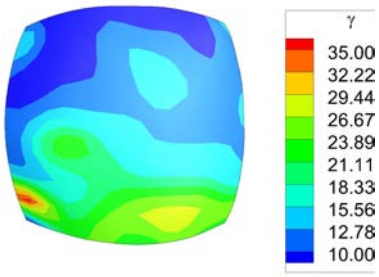

(h) Patient 7(a)

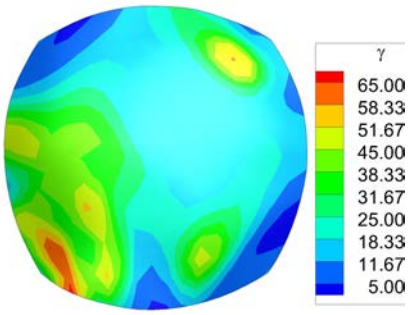

(i) Patient 7(b)

Figure 4.3: γ values of all patients

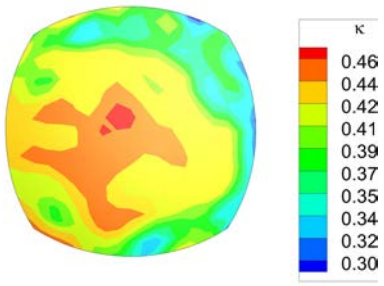

(a) Patient 1

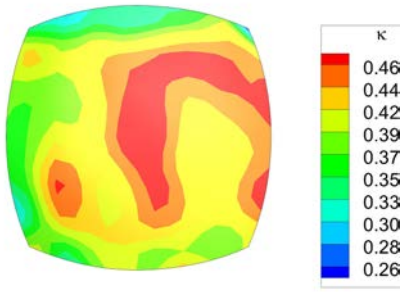

(b) Patient 2

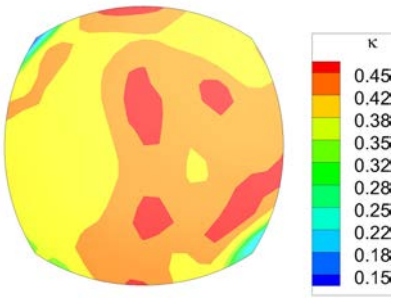

(c) Patient 3

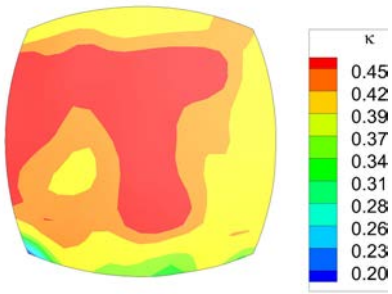

(d) Patient 4

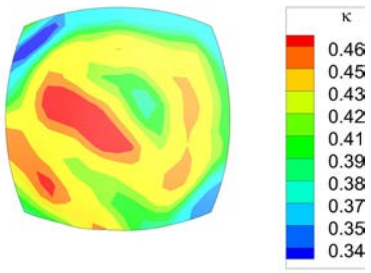

(e) Patient 5(a)

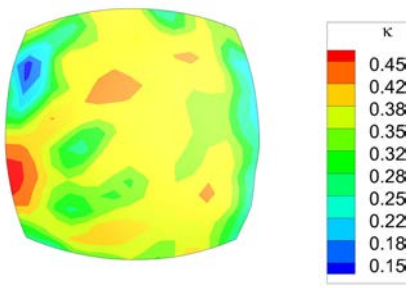

(f) Patient 5(b)

Figure 4.4: κ values of all patients

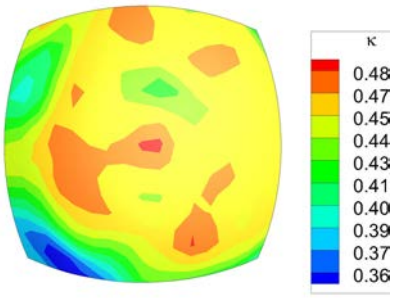

(g) Patient 6

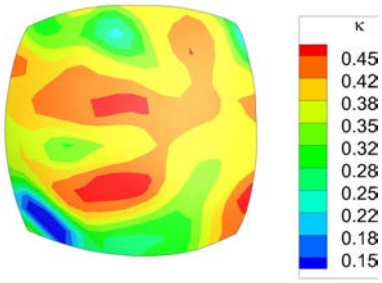

(h) Patient 7(a)

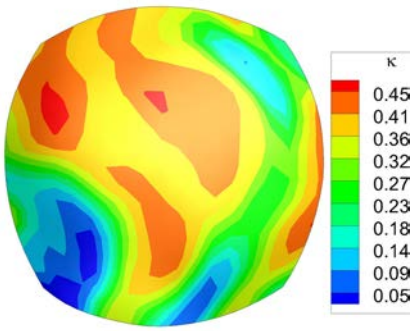

(i) Patient 7(b)

Figure 4.4: κ values of all patients

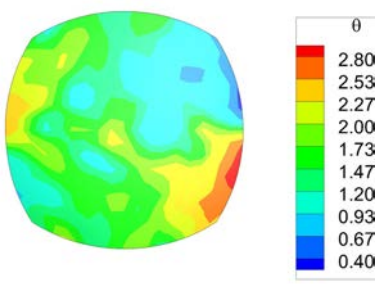

(a) Patient 1

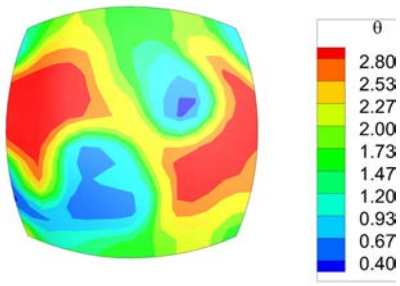

(b) Patient 2

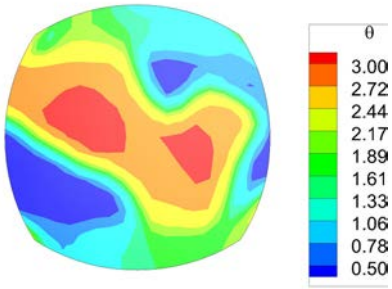

(c) Patient 3

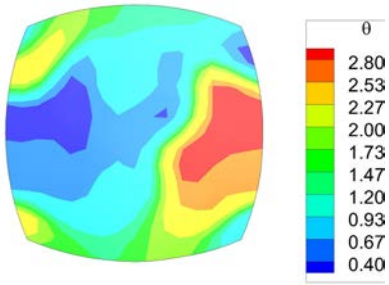

(d) Patient 4

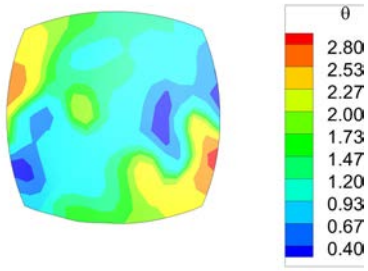

(e) Patient 5(a)

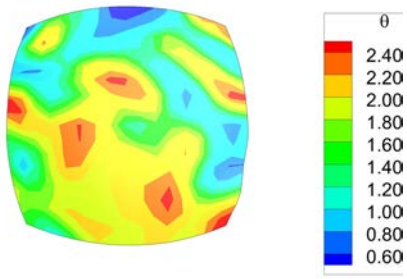

(f) Patient 5(b)

Figure 4.5: θ (rad) values of all patients

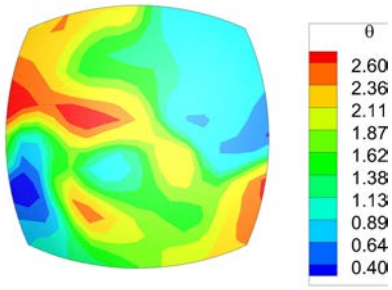

(g) Patient 6

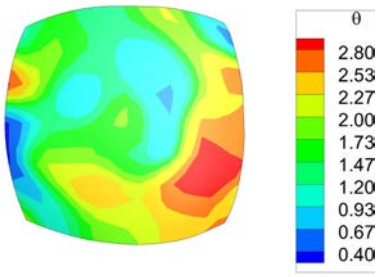

(h) Patient 7(a)

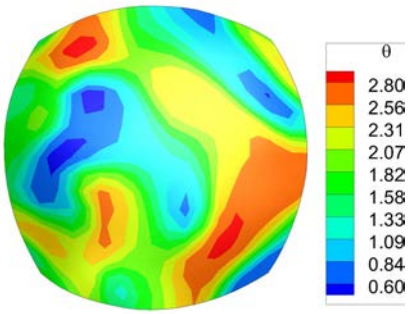

(i) Patient 7(b)

Figure 4.5: θ (rad) values of all patients

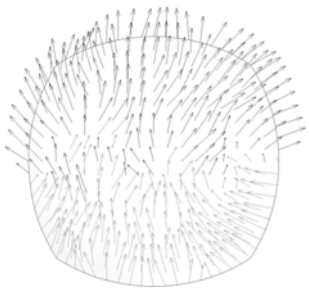

(a) Patient 1

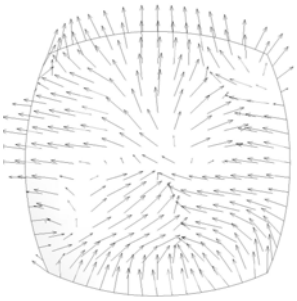

(b) Patient 2

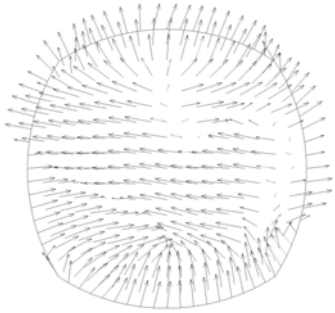

(c) Patient 3

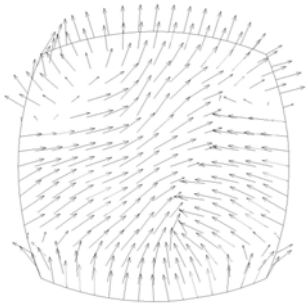

(d) Patient 4

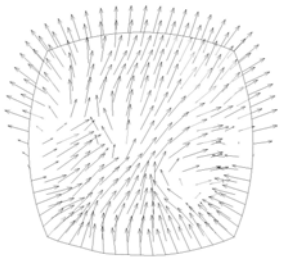

(e) Patient 5(a)

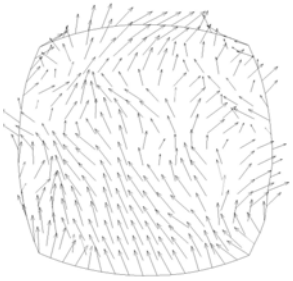

(f) Patient 5(b)

Figure 4.6: Fiber direction of all patients

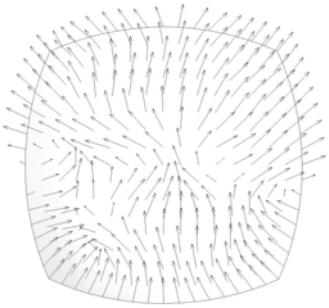

(g) Patient 6

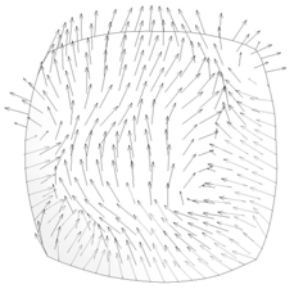

(h) Patient 7(a)

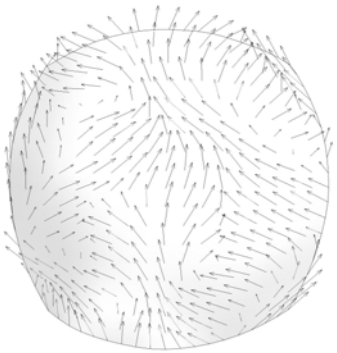

(i) Patient 7(b)

Figure 4.6: Fiber direction of all patients

4.2.2 Forward validation

With the material properties defined on each Gauss point, fully heterogeneous finite element models were derived. Forward finite element analysis was performed on all cases with the identified material properties to simulate the inflation process. The resulting displacement, stress, and strain were compared to experimental data at each pressure state. The stress, strain and displacement error distributions are presented in Figure 4.9, 4.10 and 4.11 respectively. Table 4.2 presents the average percentage errors in the last pressure state. In general, the forward replicated the inflation motion to a high accuracy. As representative examples Figure 4.7 shows that local stress and strain patterns where accurately recovered, and so were the displacements (Figure 4.8).

4.3 Discussion

4.3.1 Major conclusions

In this study, the heterogeneous properties in 9 human ATAA samples were delineated based on full-field stress and strain data acquired from DIC measurements and inverse stress analysis. The purpose of the study is to reveal the heterogeneity of ATAA tissues, albeit still over samples of moderate size. We have resolved the material properties to the spatial resolution of Gauss point spacing, which in our case was on the order of 0.3 mm. This resolution can be further improved by refining the mesh. We validated the heterogeneous properties by forward analyses, and verified that the properties can replicate not only the global deformation and also the local

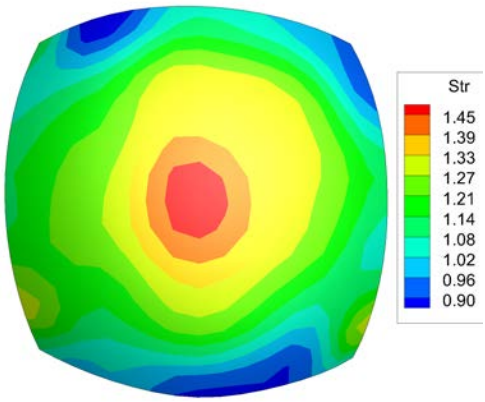

(a) Patient 4 Inverse Stress (N/mm)

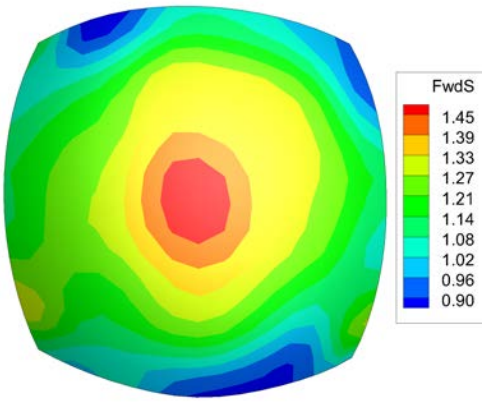

(b) Patient 4 Forward Stress (N/mm)

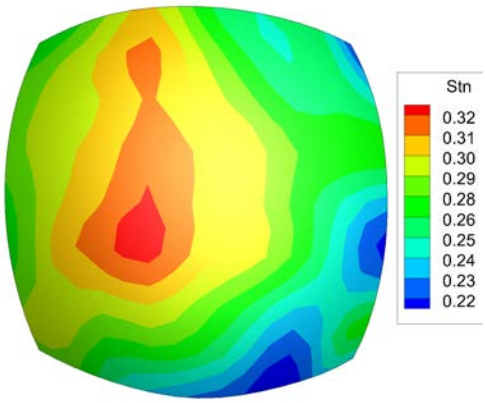

(c) Patient 4 DIC Strain

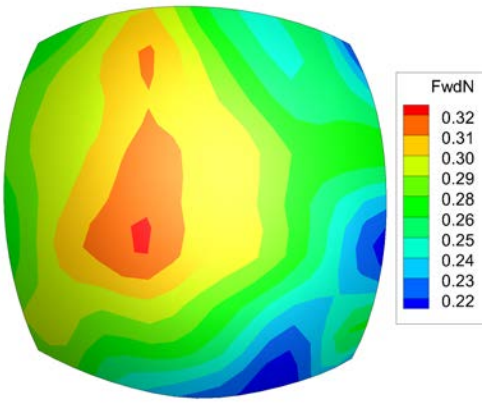

(d) Patient 4 Forward Strain

Figure 4.7: Comparison of experimental and forwardly recovered stress strain distributions in two samples at the last pressure stage

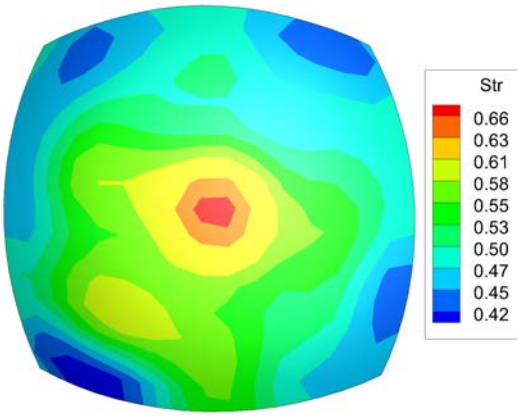

(e) Patient 6 Inverse Stress (N/mm)

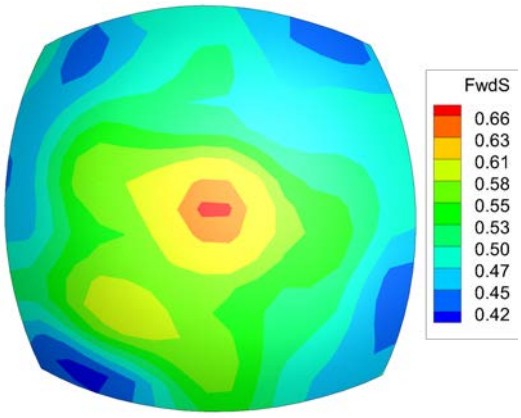

(f) Patient 6 Forward Stress (N/mm)

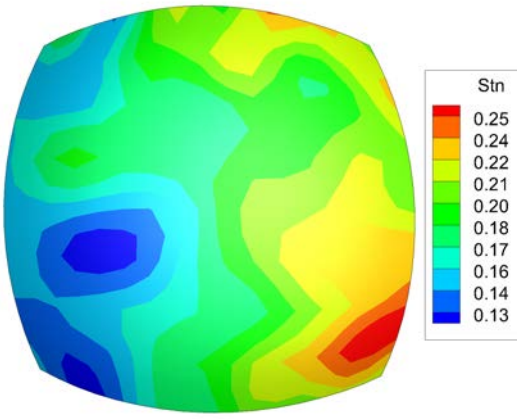

(g) Patient 6 DIC Strain

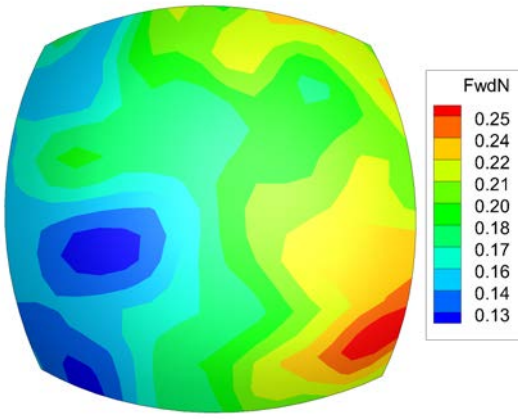

(h) Patient 6 Forward Strain

Figure 4.7: Comparison of experimental and forwardly recovered stress strain distributions in two samples at the last pressure stage

Table 4.2: Stress, strain and displacement error at highest pressure states

Patient	Pressure(kPa)	Stress(%)	Strain(%)	Displacement(%)
1	117	4.95	1.36	0.14
2	99	2.13	2.47	0.46
3	57	2.50	1.50	0.12
4	96	1.73	1.30	0.22
5(a)	48	2.94	7.61	0.64
5(b)	42	3.83	6.01	0.49
6	42	2.29	3.87	0.71
7(a)	81	3.64	3.84	0.36
7(b)	33	13.0	16.8	2.05
Mean	69.5	3.82	3.84	0.36

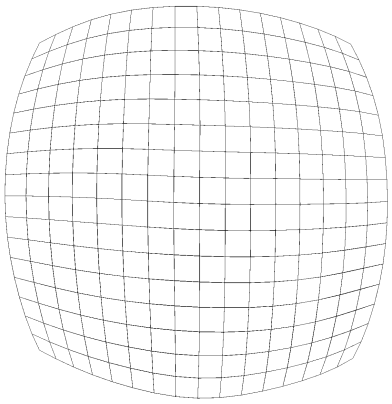

(a) Patient 4 Inverse Mesh and Forward Predict Mesh

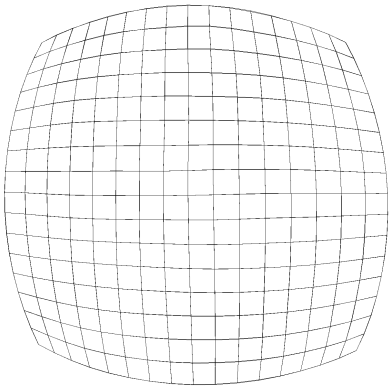

(b) Patient 6 Inverse Mesh and Forward Predict Mesh

Figure 4.8: Comparison of experimental and predicted displacement fields at the last pressure state

stress and strain patterns.

From the results, it is evident that ATAAs are highly heterogeneous. There is a significant level of property variation even within samples of 2 cm in diameter. In previous section, it has been shown that for mechanical analysis a pointwise resolution of heterogeneous property is necessary for accurately predicting the stress and strain states. The true value of this study, perhaps, is that it resolves the properties to a resolution that is comparable to microstructural imaging, thus opens the possibility to quantitatively correlate the local properties to the underlying microstructure of the tissue.

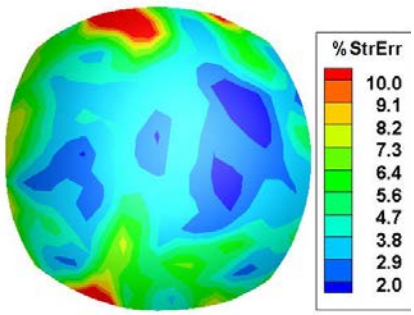

(a) Patient 1

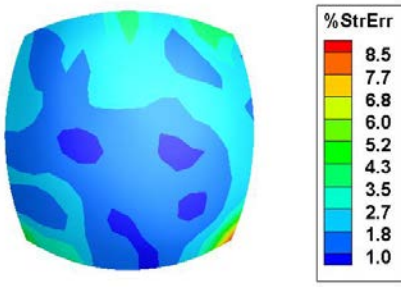

(b) Patient 2

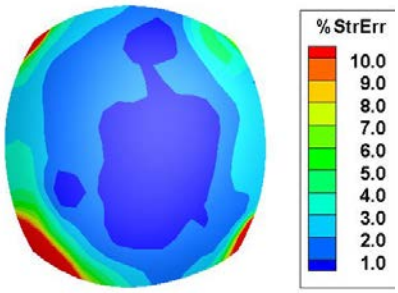

(c) Patient 3

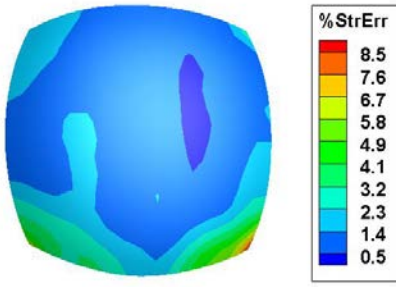

(d) Patient 4

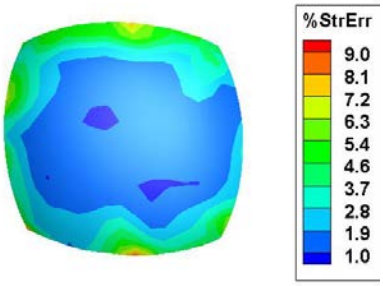

(e) Patient 5(a)

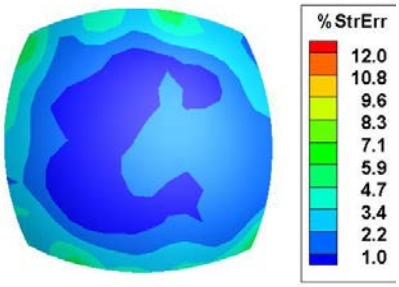

(f) Patient 5(b)

Figure 4.9: Stress error (in %) distribution

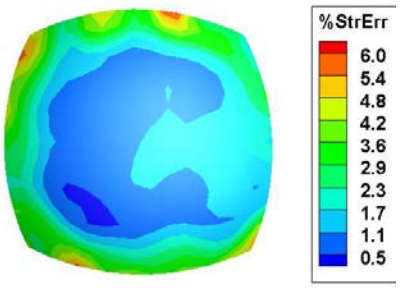

(g) Patient 6

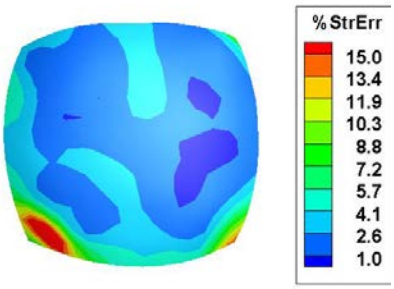

(h) Patient 7(a)

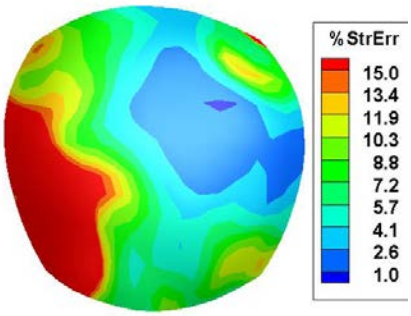

(i) Patient 7(b)

Figure 4.9: Stress error (in %) distribution

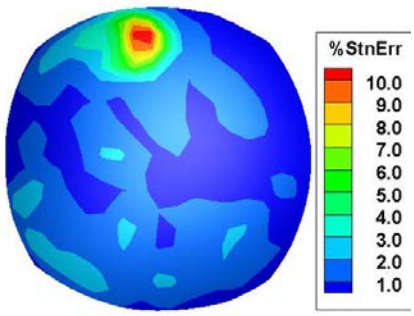

(a) Patient 1

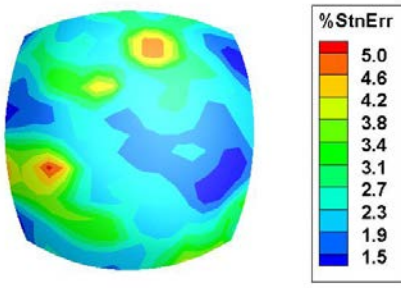

(b) Patient 2

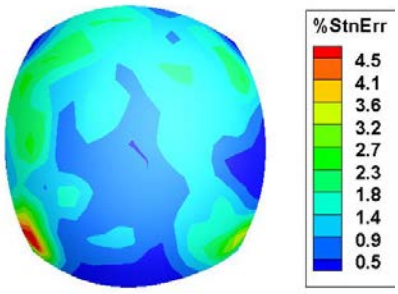

(c) Patient 3

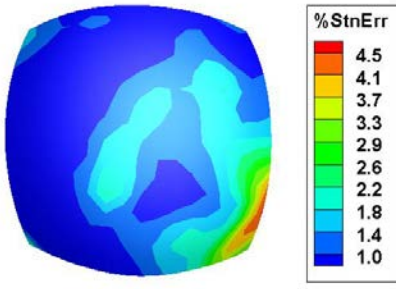

(d) Patient 4

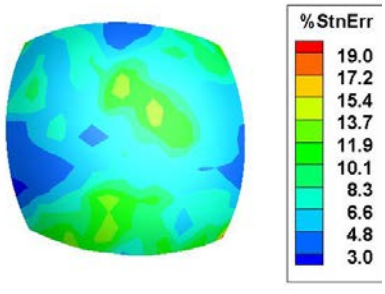

(e) Patient 5(a)

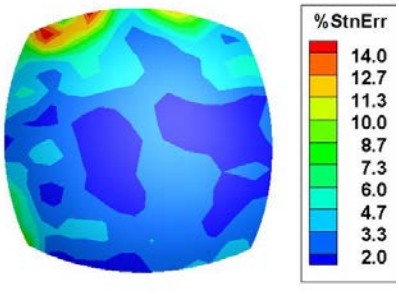

(f) Patient 5(b)

Figure 4.10: Strain error (in %) distribution

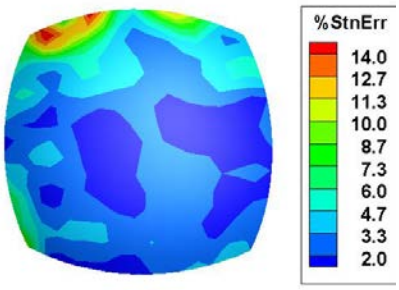

(g) Patient 6

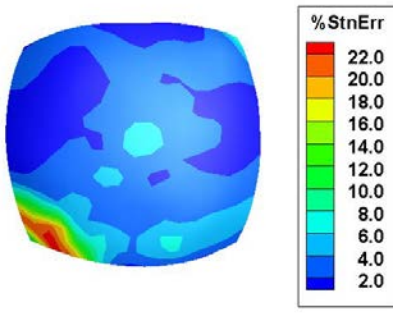

(h) Patient 7(a)

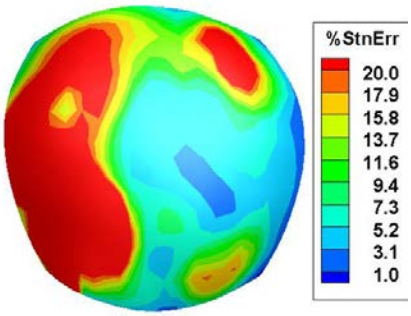

(i) Patient 7(b)

Figure 4.10: Strain error (in %) distribution

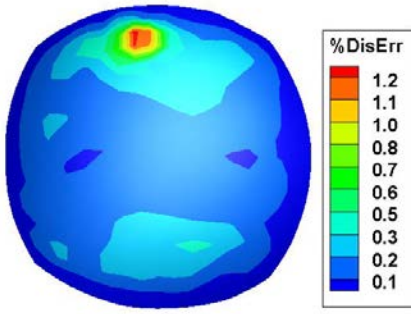

(a) Patient 1

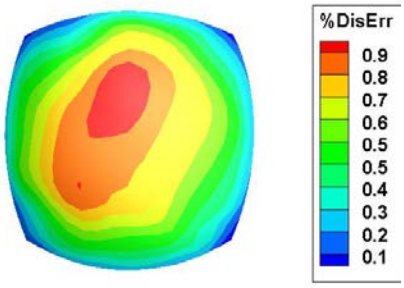

(b) Patient 2

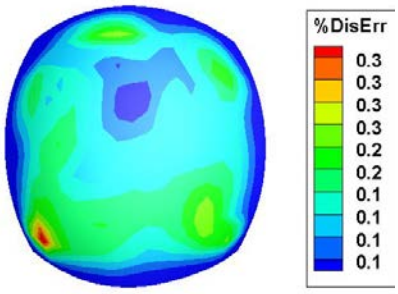

(c) Patient 3

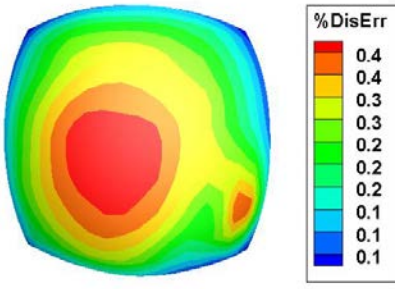

(d) Patient 4

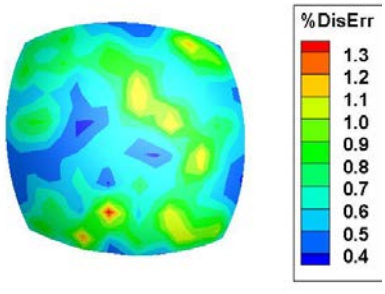

(e) Patient 5(a)

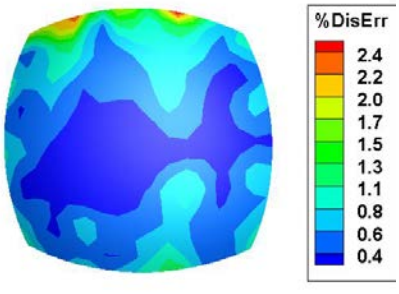

(f) Patient 5(b)

Figure 4.11: Displacement error (in %) distribution

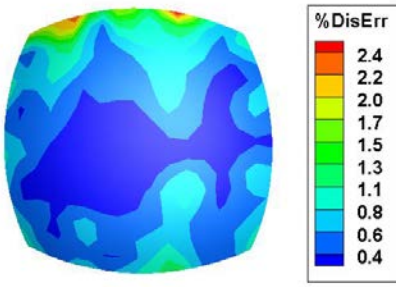

(g) Patient 6

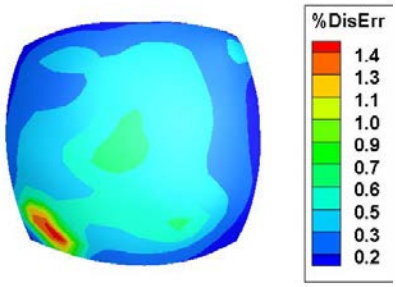

(h) Patient 7(a)

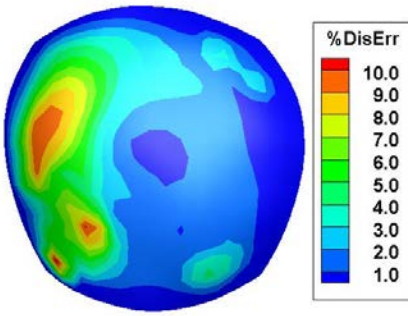

(i) Patient 7(b)

Figure 4.11: Displacement error (in %) distribution

4.3.2 Comparing with existing data in the literature

In terms of the domain average values, our results are consistent with the findings of other studies. Romo et al. reported that μ_2 was in the range of 0.01 to 0.11 N/mm^2 [106]. Their energy function has a different factor ($\frac{\mu_2}{2}$) in contrast to the $\frac{\mu_2}{4}$ in the present function. Also, there are two exponential (fiber) terms in their function whereas the present model contains only one. Finally μ_2 in [106] is in force per unit area whereas the present paper is in force per unit length. Considering the factor difference and the tissue thickness (approximately 2 mm), the μ_2 range Romo's paper should correspond to 0.08-0.88 N/mm, which is comparable to the present results of 0.27 – 1.75 N/mm. The values of γ (0.90 – 14.57 in Romo[106]) also compare well with the present result, 1.61 – 23.94. Pierce et al. [99] obtained ATAA properties obtained using uniaxial tests. They reported that the ranges of μ_1, μ_2 and γ are 0.032 –0.092 N/mm, (0.48 – 31.68 N/mm, and 0.00 –94.63, respectively. The stiffness values have been similarly converted. These results are comparable, although their parameter values seem much more dispersed across patients. Healthy human thoracic data, 0.028 – 0.038 for μ_1, 0.48–1.88 for μ_2 and 5.79–34.79 for γ, were also reported by Pierce [99] et al. Overall, μ_2 and γ are smaller in healthy ATAA sample, supporting again the known fact that ATAA development is a process of collagen reinforcement and stiffening. Consistent with other report. e.g., [106, 100], the values of μ_1 are orders of magnitude smaller that μ_2, indicating that ATAAs are depleted of elastin content. The dispersion parameter, κ, should vary from 0 to 0.5 with $\kappa = 0$ corresponding to a perfect alignment of collagen fibers in the direction $\mathbf{M}$

and $\kappa = \frac{1}{2}$ indicating isotropy. As seen from Table 4.1, the average value of κ is 0.4. This suggests that the ATAAs are moderately anisotropic.

4.3.3 Possible explanation of the identified parameters

The mean values of fiber angle were found to be close to 1.50 (approximately $\frac{\pi}{2}$) in most cases. The local basis vector $\mathbf{G}_1$ is tangent to the horizontal mesh lines which are in the circumferential direction. Thus, $\frac{\pi}{2}$ indicates the longitudinal direction. Note that, the mean fiber angle is close to $\frac{\pi}{2}$ does not necessarily mean that the major symmetry axes is in the longitudinal direction, because, for example, two family of fibers with one at 10° and the other 170° also give an average angle of 90°. A glance at the symmetry axes orientation in Figure 4.6 can tell that there appear to be four dominate direction: circumferential, longitudinal, and two helical directions at 45° and 135°. Indeed, if we separate the asymmetry axes into two groups, those in $[0, \frac{\pi}{2}]$ and in $[\frac{\pi}{2}, \pi]$ in the manner of Pierce et al. [99], we find that the mean value θ in the first group ($[0, \frac{\pi}{2}]$) is 0.80, and the second group $[\frac{\pi}{2}, \pi]$ is 2.36, corresponding nicely to a 45° and a 135° orientation. This analysis suggests that a modified energy function containing four fiber families may better describe the material. Although the number of subjects is relatively small, the present study still shed light on inter- and intra-subject variability in ATAA properties. Not surprisingly the ATAAs exhibited a large inter-subject variability in the elastic properties. Among the samples there are two intra-subject groups. For samples from patient 5, the mean values of μ_1, μ_2, γ, κ and θ are 0.22E-02& 0.69E-02, 0.28 & 1.75, 7.75 & 23.94, 0.41 & 0.37 and 1.39 &

1.54 for (a) & (b) respectively; For patient 7, the mean values of μ_1, μ_2, γ, κ and θ are 0.51E-02& 0.15E-02, 1.10 & 1.83, 15.19 & 23.24, 0.37 & 0.30 and 1.74 & 1.77 for (a) & (b) respectively; The intra-subject study indicates that property variation not only exists in inter-subject patients but also within intra-subject patient. Unfortunately, the information on where these sampled were harvested is not available and therefore it is hard to pin down the regional variations to specific locations. Nevertheless, if we view the average values as the material parameters that one would obtain from a bi-axial tension test applied to the samples, we could conclude that, even at this length scale, there could be significant variability in properties. This conclusion was evidenced by the results from Choudhury who claimed that local variations exist in human abdominal aneurysm mechanical properties[15].

4.3.4 Limitation

There are several limitations embedded in this study. First of all, all results are obtained from 9 cases. This limited sample size prevented us form drawn any statistic conclusions from the results. In addition, the experiments, like many other works, were performed on a small section of ATAA[99, 117]. Although the parameter distributions were mapped out, they are of the sample only and not to be extrapolated. It is even unclear how the distributive parameters can helping modeling and analysis. Nevertheless, the work demonstrated that the heterogeneous properties can be resolved to a very fine spatial resolution, and indeed there are significant property variations in samples of 2 – 4 cm in dimensions. This is the length scale over which

the tissue is taken as homogeneous in traditional bi-axial testing.

The material model can also be improved. The energy function considers a planar fiber distributions which at the end yielded an orthotropic model. The retrospective analysis on the fiber distribution suggested that, perhaps, a four fiber family model similar could be more pertinent[36]. In addition, we did not consider fiber recruitment; a direct consequence could be that the model failed to fit the stress strain date at low pressure regime where the collagen fibers could remain crimped and there do not contribute to load bearing. A recruitment mechanism as that in may improve the curve fitting at low pressures[55]. Also, the configuration of the first pressure step (3 Kpa) was taken to be the stress-free reference, assuming that the pressure balanced the tissue weight in this configuration. This assumption is debatable. A possible improvement to include the pre-stress in the 3 Kpa state in the model and identify them in the nonlinear regression. Nevertheless, these improvement are unlikely to fundamentally change the findings and conclusions, since the material model in overall described the stress-strain very well.

In closing, the pointwise material parameters were characterized in 9 human ascending thoracic aneurysm (ATAA) samples. The ATAA samples were found moderately anisotropic and highly heterogeneous. As alluded before, the true value of this work perhaps lies in that it can provide heterogeneous properties to a spatial resolution comparable to that of microscopic imaging. This opens the possibility of correlating the local properties to the underlying microstructure.

CHAPTER 5
RUPTURE PATTERNS

5.1 Method

5.1.1 Rupture characteristics identification framework

From a biomechanical point of view, rupture happens when the wall stress causing by blood flow and other loadings exceeds the strength limit of the wall tissue. Hence, the tissue strength is one of the fundamental properties connecting to tissue failure. The mechanical properties of ATAA tissue have been investigated by several groups in the last decade. Most of their published data refer to uni-axial or bi-axial tensile tests on the tissues which intrinsically treat the sample as homogeneous. In order to cope with heterogeneity, they either divide the samples according to the harvest location (regionally) or directionally. But overall, the property resolution identified by those methods can be only based on the sample size (typically several centimeters). In general, rupture initiates at the location where the micro-structure starts to break down. Consequently, the local conditions at the rupture site instead of homogenized measures are more meaningful for rupture assessment. In this section, some patterns of ATAA rupture in the inflation test are reported. The work flow is summarized in Figure 5.1.

5.1.2 Rupture site and rupture tension

The rupture tension is defined as the ultimate tension at the rupture site. Since it is unclear whether a component of the tension or the norm (i.e. the total) is

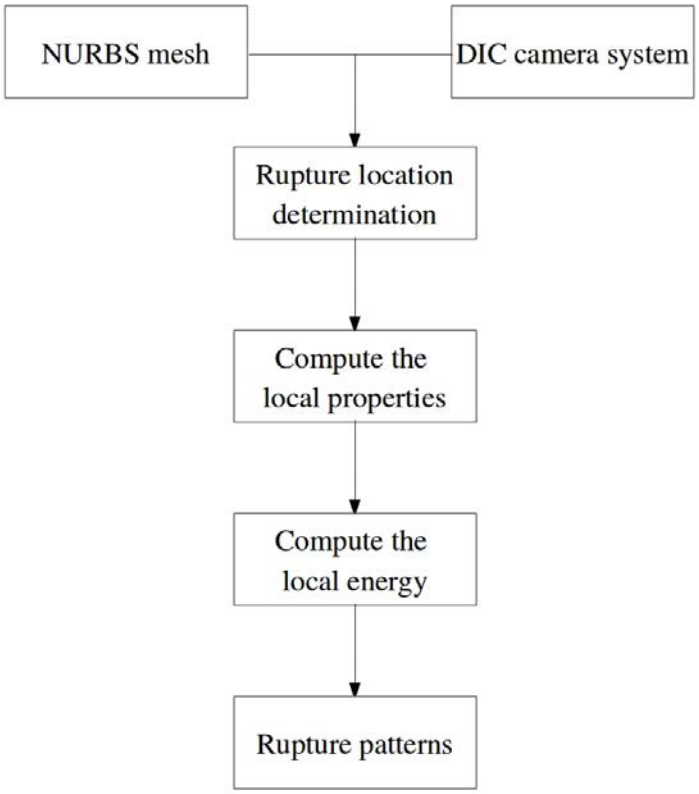

Figure 5.1: Flowchart of rupture patterns identification

a better index, both the norm and the component in the orifice normal direction were computed. The rupture site was identified from the photo image of the second last loading step (the one immediate preceding rupture), or the post rupture image if the one before does not show distinct cracks. The identification scheme is illustrated in Figure 5.2. The bounding coordinates of the orifice were measured in the DIC camera coordinate system. The average values of the horizontal and vertical directions were assumed to be the location of rupture initiation, that is the rupture site. Most specimens bore narrow elliptical cracks. There was one case having symmetric $\wedge$-shaped or curved orifices. For these cases the center of symmetry was taken to be the rupture site. The identification scheme could induce uncertainties in the identified location. To alleviate the influence, the average tension in a small window containing the rupture site was used to determine the rupture tension. The window consists of the crack element and eight surrounding elements (Fig.5.2(b)), containing a total of 81 Gauss points. The size of the window is approximately 9 mm^2. The same average was applied to all other rupture site variables.

5.1.3 Orifice orientation

In eight out of nine cases the orifices were narrow straight slivers, enabling an easy definition of orientation. Figure 5.2(c) illustrates how the orientation was determined. The direction of crack propagation was manually identified, from which the normal direction was determined following the right-hand rule. For the $\wedge$-shape orifice, each branch was treated as a single straight crack. The orientation of the

orifice was characterized by the angle the normal makes to the horizontal direction.

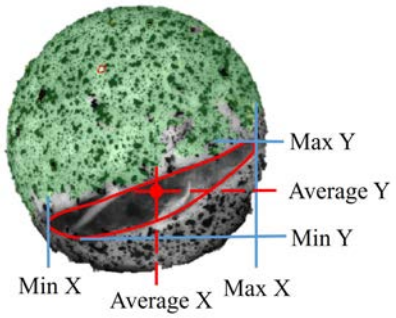

(a) A post rupture image showing orifice

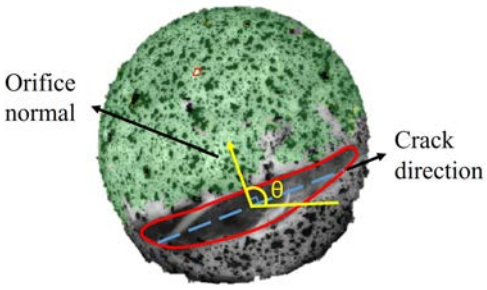

(b) Orifice orientation

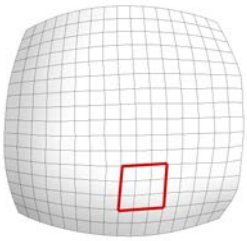

(c) Local window of rupture site

Figure 5.2: Determination of rupture site and orifice orientation

5.1.4 Toughness

Toughness, a measure of material's resistance to fracture, is the amount of energy needed to fracture a material. It can be computed by accumulating the work done by the stress prior to fracture, viz. $TH = \int_{\mathbf{0}}^{\mathbf{E}_f} S_{IJ} dE_{IJ}$. Here S_{IJ} and E_{IJ} are the components of the second Piola-Kirchhoff stress and Green-Lagrangian strain,

respectively, $\mathbf{E}_f$ is the ultimate strain. As the tension and strain values were made available at each Gauss point throughout the loading process, the stress work can be computed locally. A middle points rule was used for this computation:

$$W \approx \sum_{k=1}^{ns-1} \frac{\left(T_{IJ}^{(k)} + T_{IJ}^{(k+1)}\right)\left(E_{IJ}^{(k+1)} - E_{IJ}^{(k)}\right)}{2} \tag{5.1}$$

where T_{IJ} is the components of the second Piola-Kirchhoff tension, E_{IJ} ia the components of the surface strain, and ns is the number of loading steps. The stress work at the rupture site was used to define the thoughness for each sample. Again the values were computed by averaging the stress work in the local window.

5.2 Results

5.2.1 Orifice orientation vs fiber direction

Having identified the rupture sites, the fiber angle at the rupture site was computed for each specimen, and then compared to the orifice orientations. Figure 5.3 presents the result. A sharp linear relation ($y = x$) between the fiber angle and the orifice normal angle is observed, indicating that the orifice is perpendicular to the local fiber direction.

In addition, the cracks appeared to propagate transversely to the fiber direction. As the latter varied spatially, this directional propagation can result in curved cracks. An example is shown in Figure 5.4. The red (gray in black-white print) crescent in the post-rupture image outlines the orifice. The crescent is superimposed on the fiber distribution map, at the same location with respect to the image coordinate system. It is shown that the fiber vectors in the orifice region are transverse to

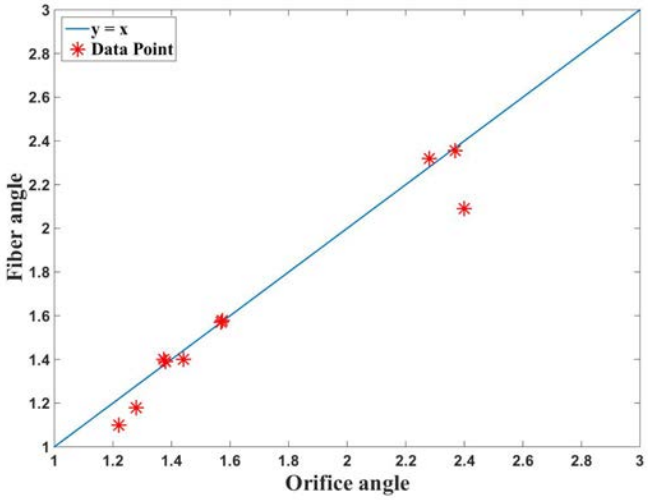

Figure 5.3: Fiber direction vs orifice normal at rupture sits

the orifice. All but one samples were found to follow this normality rule, and seven additional cases are shown in Figure 5.5. The outlier will be discussed later.

5.2.2 Strength and toughness

The norm of the rupture tension, T_f, the component in the fiber direction, T_n, the ultimate strain (norm), E_f, the component in the fiber direction, E_n, and the toughness TH are listed in Table 5.1. Note that the fiber direction can also be interpreted as the direction of orifice normal. No significant relation was found between T_f and TH (p = 0.04), between T_n and TH (p = 0.05), and between E_f and TH (p = 0.006). However, the strain in the fiber direction and the toughness is related (p = 0.18).

To explore whether the peak tension or the stress work (referred to as energy hereafter) is a better predictor of the rupture location, we superimposed the identified

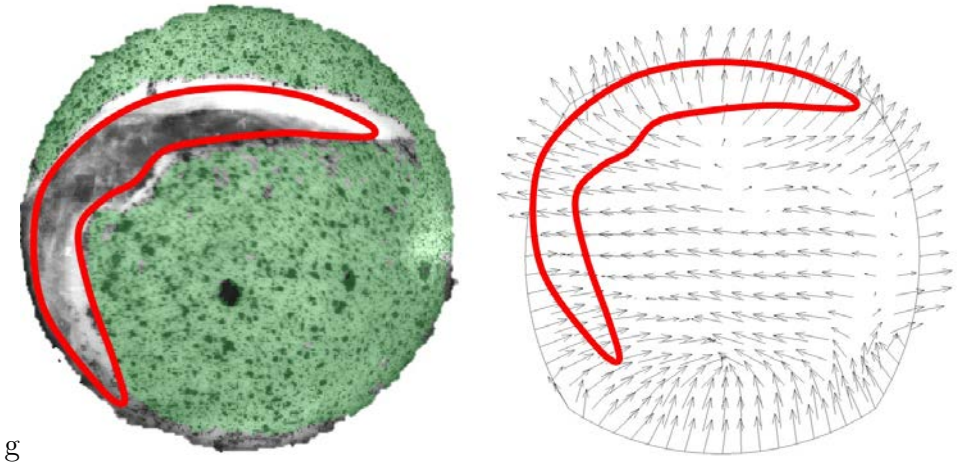

g

(a) Post-rupture image (b) Fiber direction

Figure 5.4: Direction of fracture propagation

rupture window on the tension and energy contours. Figure 5.7 presents two cases. The remaining seven cases are included in Figure 5.6. The boxes are the local window defining the rupture site. It can be seen that for patient 1, both the peak tension and the peak energy predicted the rupture location. For patient 2(b), however, the peak energy predicted the rupture location while the peak tension missed. When the local rupture window encloses or overlaps the peak tension or peak stress red spots, we say that a match is found. The result of matching for all night cases is reported in Table 5.2. It can be seen that the peak energy matched in six out of nine cases, whereas the peak tension matched in four cases. Thus, the peak energy appears to be a more reliable predictor of rupture location.

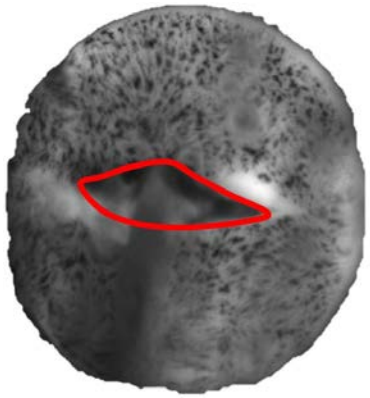

(a) Patient 1: Orifice image

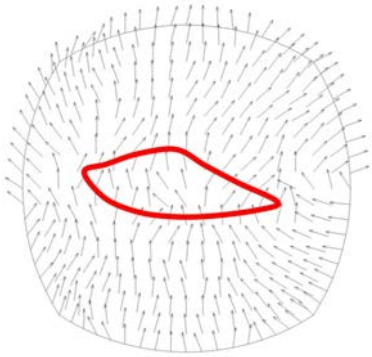

(b) Patient 1: Fiber direction

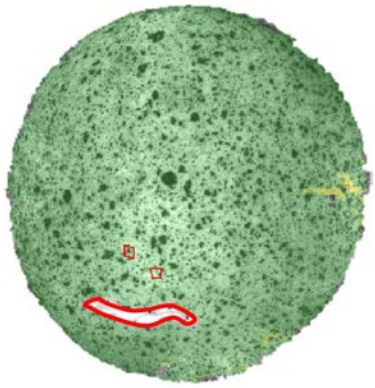

(c) Patient 2: Orifice image

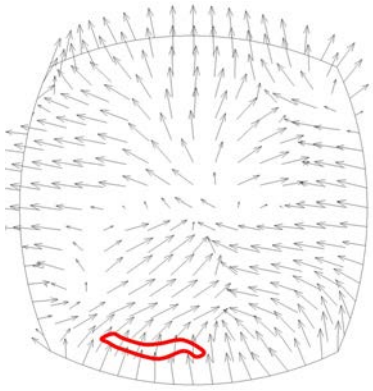

(d) Patient 2: Fiber direction

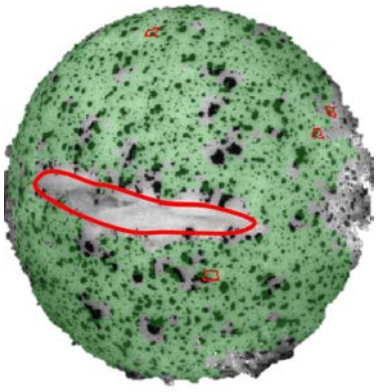

(e) Patient 5(a): Orifice image

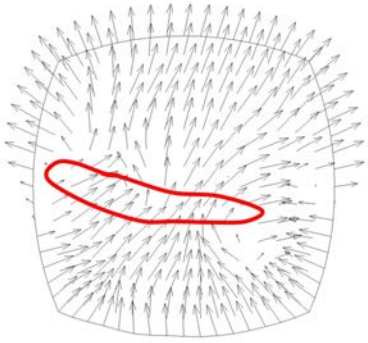

(f) Patient 5(a): Fiber direction

Figure 5.5: Orifice orientation and fiber direction

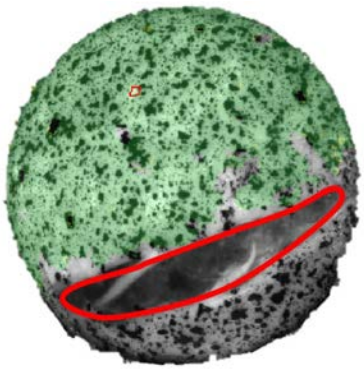

(g) Patient 5(b): Orifice image

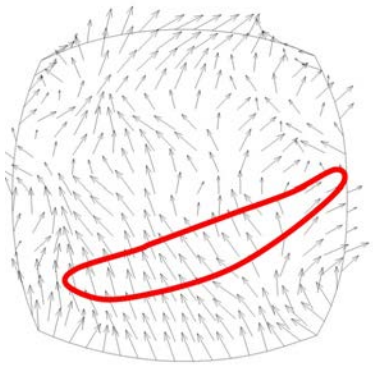

(h) Patient 5(b): Fiber direction

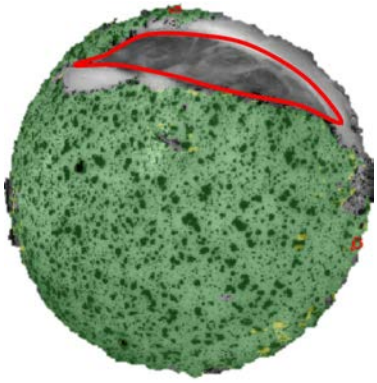

(i) Patient 6: Orifice image

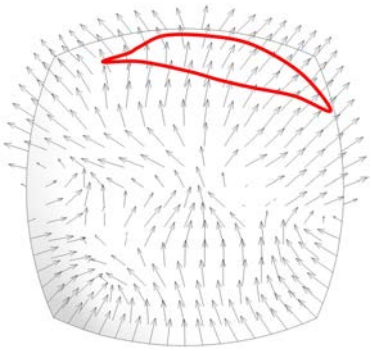

(j) Patient 6: Fiber direction

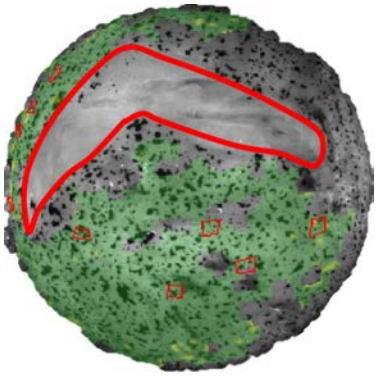

(k) Patient 7(a): Orifice image

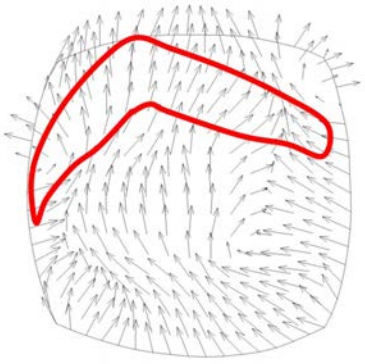

(l) Patient 7(a): Fiber direction

Figure 5.5: Orifice orientation and fiber direction

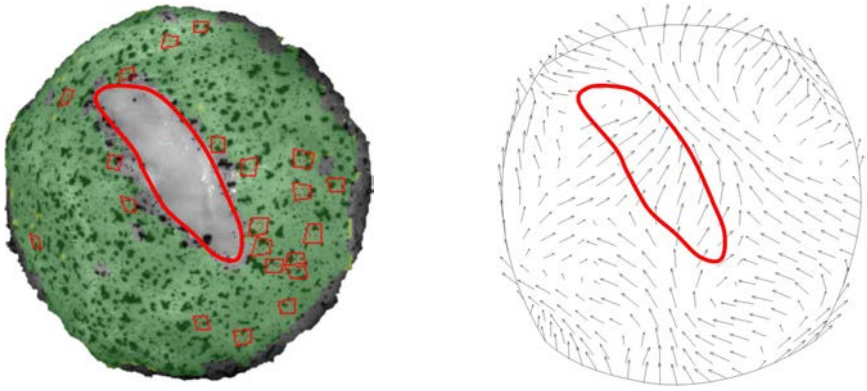

(m) Patient 7(b): Orifice image (n) Patient 7(b): Fiber direction

Figure 5.5: Orifice orientation and fiber direction

5.3 Discussion

5.3.1 Fiber direction

Most biomechanical studies on ATAA properties treated tested specimens as homogeneous. Mechanical properties were obtained from samples of centimeter size. However, the microstructure of the ATAA determines its highly heterogeneous characteristics. At the presence of strong heterogeneities, homogenized stress strain obtained from the uni-axial or bi-axial tests may not be conclusive with regard to the local condition at the rupture site. To address this challenge, we investigated ATAA rupture properties without the assumption of homogeneity. The stress, strain, and properties distributions were identify to within a sub-millimeter resolution. Based on field data of this resolution, rupture site values were obtained by averaging the field data in a local window of approximately 3×3 mm^2. At this level of locality, the ATAA's rupture appears to exhibit some distinct characteristics and consistent

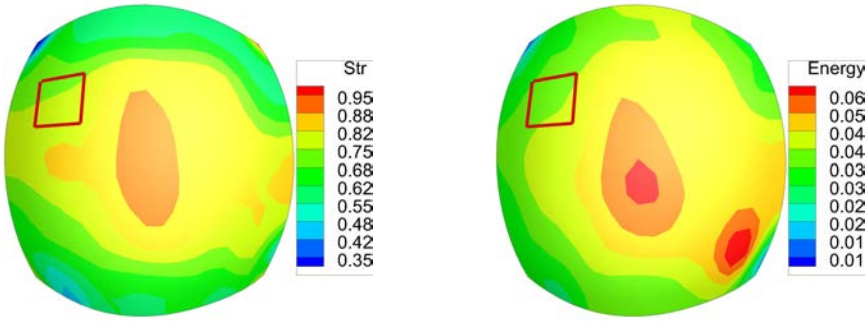

(a) Patient 3: Tension (b) Patient 3: Energy

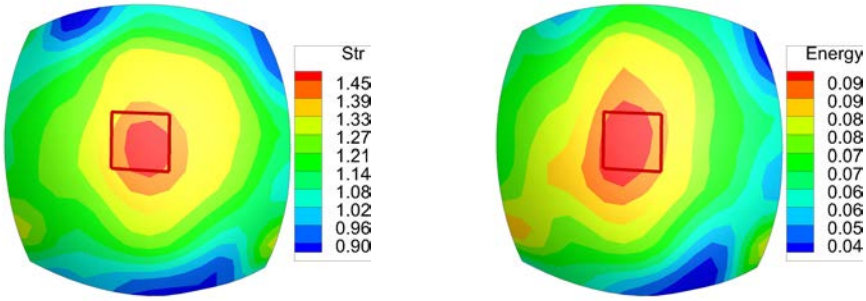

(c) Patient 4: Tension (d) Patient 4: Energy

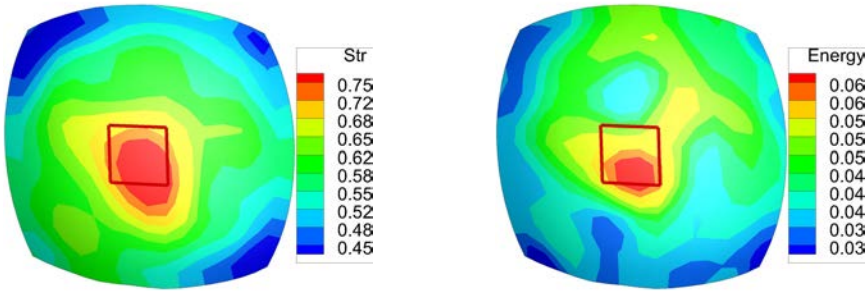

(e) Patient 5(a): Tension (f) Patient 5(a): Energy

Figure 5.6: Rupture location and the sites of the peak tension (N/mm) and peak energy (N/mm)

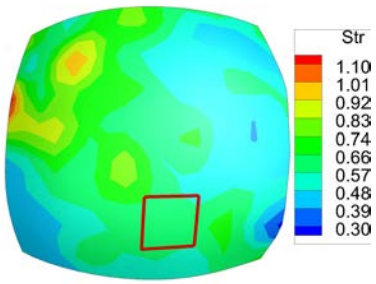

(g) Patient 5(b): Tension

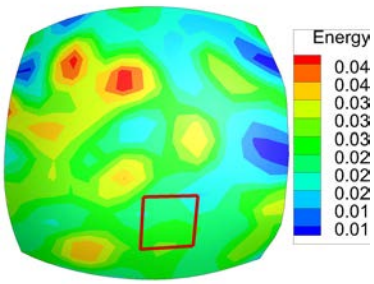

(h) Patient 5(b): Energy

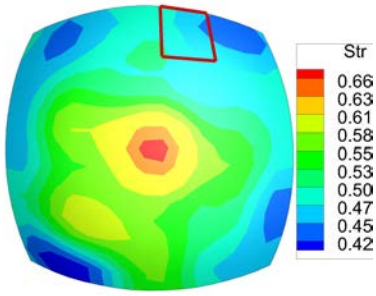

(i) Patient 6: Tension

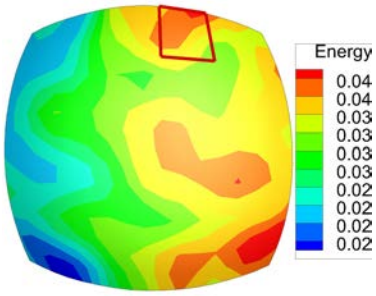

(j) Patient 6: Energy

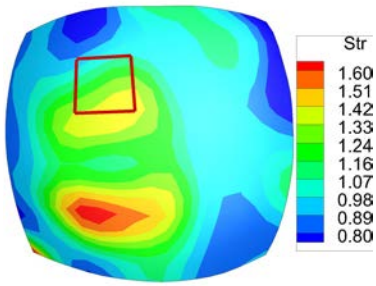

(k) Patient 7a: Tension

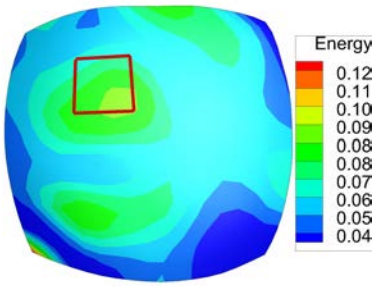

(l) Patient 7(a): Energy

Figure 5.6: Rupture location and the sites of the peak tension (N/mm) and peak energy (N/mm)

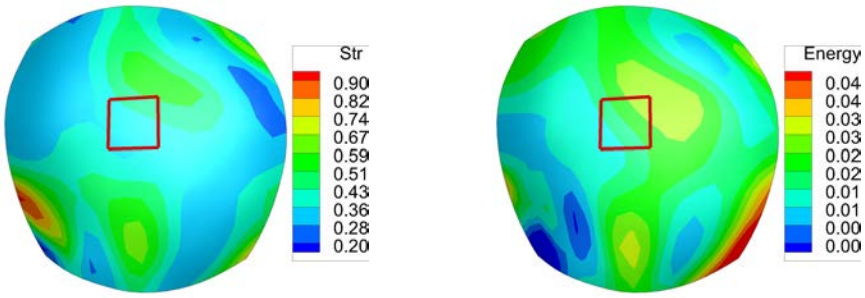

(m) Patient 7(b): Tension (n) Patient 7(b): Energy

Figure 5.6: Rupture location and the sites of the peak tension (N/mm) and peak energy (N/mm)

patterns.

The most striking pattern is that the cracks are preferentially transverse to the fiber direction - the direction of the highest stiffness. In all but one cases the orifice normal is parallel to the local fiber direction. Not only that, the cracks propagated transversely to the fiber direction as well, in some cases resulting in curved orifices. This phenomenon appears counter-intuitive, as one would expect that the tissue cleaves along the fiber, generating orifices that are more or less parallel to the fiber direction. To verify whether the fiber direction was correctly described, the directional stiffness of the tissue was examined. The stress and strain in at the rupture site were rotated to a local system in which the $\mathbf{e}_1$ basis coincides with the fiber direction and $\mathbf{e}_2$ the transverse direction. The rotated stress strain curves of all cases were generated and examined. An example of such curves is shown in Figure 5.8. Note that the stress state is bi-axial; any component (say T_{11}) is a function of three strain

Table 5.1: Strength, ultimate strain, and toughness

Patient	T_n (N/mm)	T_f (N/mm)	E_n	E_f	TH (N/mm)
1	1.71	1.32	0.90	0.60	0.34
2	1.12	0.91	0.26	0.19	0.07
3	0.64	0.51	0.21	0.16	0.04
4	1.44	1.08	0.30	0.19	0.10
5(a)	0.75	0.56	0.38	0.25	0.07
5(b)	0.62	0.52	0.16	0.09	0.02
6	0.48	0.37	0.21	0.13	0.04
7(a)	1.13	1.00	0.26	0.16	0.07
7(b)	0.37	0.31	0.14	0.11	0.02

components. The response functions are surfaces in a high dimensional space. The curves shown here are the projections of the response function into two-dimensional spaces. In all cases the T_{11} curve lies above T_{22}, indicating that the tension in the fiber direction is higher than that in the transverse direction in all load steps. Given that the strains are approximately equal-biaxial, the fact that T_{11} is above T_{22} indicates that the tissue is indeed stiffer in the identified fiber direction.

Could it be that T_{11} happens to be the principal tension so that the tissues

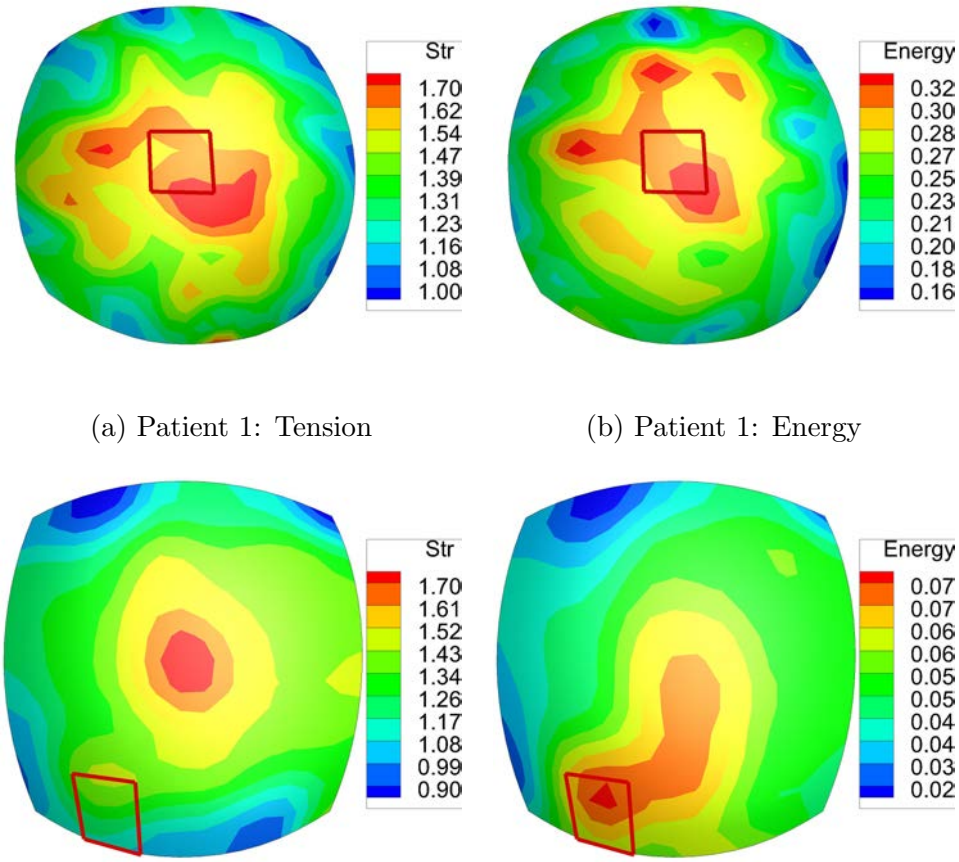

(a) Patient 1: Tension

(b) Patient 1: Energy

(c) Patient 2(b): Tension

(d) Patient 2(b): Energy

Figure 5.7: Rupture site vs the locations of peak tension (N/mm) and peak energy (N/mm)

were merely cleaving in the direction of maximum force? To answer this question, the principal directions were calculated and found that they do not coincide with the fiber direction in most cases. An example of the directional comparison in shown in Figure 5.9. The principal directions were computed from the state prior to rupture. It is clear that the fiber directions are different from the principal directions. In particular,

Table 5.2: Rupture location vs the position of peak tension or peak energy: do they match

Energy (Y/N)	Y	Y	N	Y	Y	N	Y	Y	N
Tension (Y/N)	Y	N	N	Y	Y	N	N	Y	N

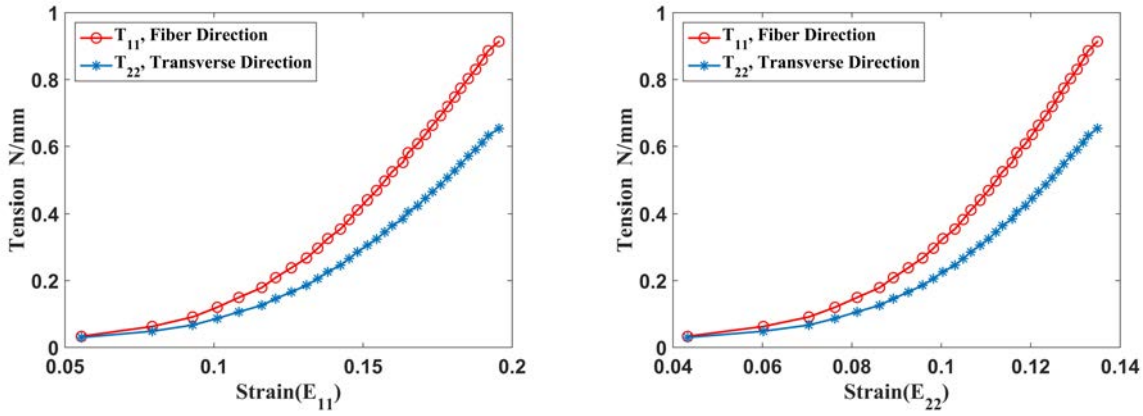

(a) Patient 2: T_{11} and T_{22} vs E_{11}

(b) Patient 2: T_{11} and T_{22} vs E_{22}

Figure 5.8: Stress-strain curves in the fiber and the transverse directions

the principal direction is transverse to the fiber direction in the crack zone.

The only exception to this directional pattern is patient 4, for which the post-rupture image, the fiber map and the contour of the dispersion parameter κ are shown in Figure 5.10. The orifice is roughly a prolate oval, seemingly parallel to the "fiber direction". A close look at the κ contour suggests that this sample is nearly isotropic in the center region where the crack initiated. It can be seen form Figure

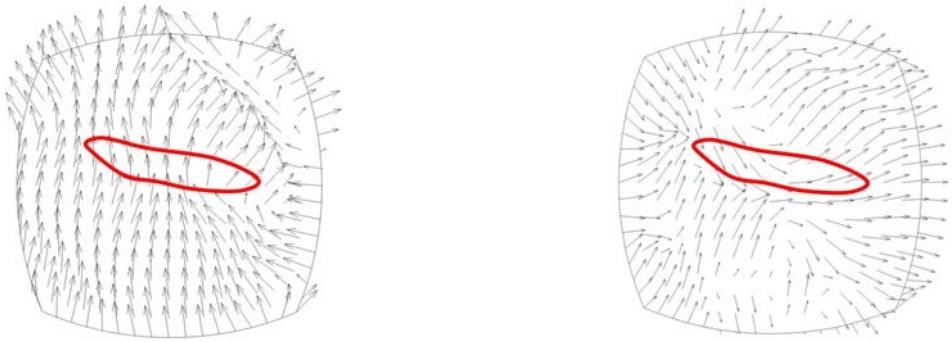

(a) Fiber direction (b) Principal direction

Figure 5.9: Comparison of fiber direction and principal tension direction. In the crack zone the principal tension aligns with the orifice opening

5.10(c) that the κ value around the initial rupture site (the windowed region) is in the neighborhood of 0.47. Recall that a κ value of 0.5 indicates isotropy. The stress-strain curves in the fiber and transverse directions are very close (Figures 5.10(d) and (e)), confirming a near isotropy. Comparing with other cases this sample has the highest average κ value. When the material is nearly isotropic, the "fiber direction" becomes less meaningful, if not completely meaningless. Thus, this case is inconclusive. The seemingly conflicting orientation does not contradict the other cases. In contrast, it highlights the underlying role of fiber distribution.

The fact that the tissue cleaves transverse to the fiber direction has some profound implications. Since the fiber direction is also the direction of preferred directional concentration of collagen, this finding suggests that the collagen content is not the, at least not the only, determinant of the ATAA strength. The microstructure of the collagen network is perhaps playing more important role. It is known that col-

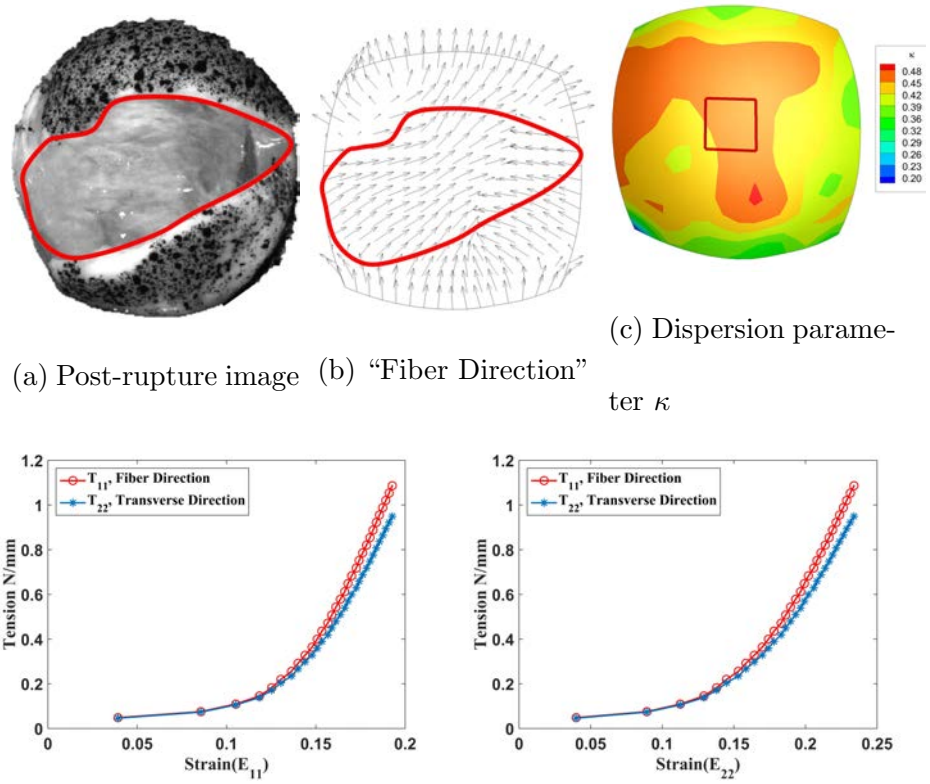

(a) Post-rupture image (b) "Fiber Direction" (c) Dispersion parameter κ

(d) T_{11} and T_{22} vs E_{11} (e) T_{11} and T_{22} vs E_{22}

Figure 5.10: Orifice, fiber map, κ contour and Stress strain curves at the rupture site for patient 4

lagen turnover is important for vessel wall repair and its degradation is believed to be associated with the rupture of aortic aneurysms[68, 36, 8]. Borges et al. reported that collagen is reduced and disrupted in human aneurysms and dissections of ascending aorta[26]. They found that while appearing as uniform lamellae in control group, the collagen fibers are disrupted and irregular in ATAA tissues. Carmo et al. found that the collagen content in abdominal aortic aneurysms is significantly lower than in controls, but there is a significant increase of collagen cross-links[12]. They sug-

gested that in aneurysmal aortic walls old collagen accumulates cross-links while new collagen biosynthesis is somehow defective. A possible explanation of the observed directional preference is that, in aneurysmal aorta tissues collagen is fragmented or disrupted, and more cross-links are formed to maintain the structural integrity. Collagen fibers are recruited to bear load, but they do not contribute much to the ultimate strength because the latter is more likely regulated by the cross-links, which are presumably weaker that the fibers. Carmo's data was from abdominal aortic aneurysms; they may not be extrapolated to ATAAs because of the difference in the two vessels. However, they suggested that the cross-links merit attention. Pichamuthu et al. also noted that differences in mechanical properties are not attributable to absolute collagen content but may be accounted for by microstructural changes in the collagen framework[97].

5.3.2 Toughness

Another observation is that the energy is likely a more reliable criterion for rupture prediction, in the sense that the location of peak energy matched the rupture site better than the peak tension. The curves in Figure 5.11 may shed light on the reason. Figure 5.11(a) presents the tension-strain curves (norm versus norm) at the rupture site and a randomly chosen, non-rupture site, from a sample wherein both the peak tension and the peak energy worked. The tension at rupture site is higher than that for comparing site in every load steps, and naturally reached the ultimate value before the comparing site. Since the tension site curve remains above, a higher

tension (and a similar strain range) necessarily implies a higher energy, and thus both worked. Figure 5.11(b) is an example where the peak energy worked whereas the peak tension failed. It can be seen that the tension at the rupture site was initially higher, but leveled off towards the end showing a progressive weakening. While the tension leveled down to roughly the same level as the comparing site, the strain continued to increase, resulting in a higher energy. For cases like this, a higher energy does not necessarily mean a higher tension, and thus the tension criterion may not work. That the energy criterion worked for more cases in the present study suggests that both stress and strain should be concurrently considered in assessing the rupture propensity. This conjecture is supported by a recent finding of Romo et al [105]. They showed that rupture of the ATAA does not systematically occur at the location of maximum stress, but at a weakened zone where strain localization happened.

5.3.3 Study limitation

The study embodied several limitations. First, all findings were based on macroscopic descriptions. The "fiber direction" is a model representation of structural features, but not a direct physical quantity measured from instruments. Although a strong relation was revealed between the fiber direction and rupture angle, the actual fiber structure was not examined. Future work is needed to link microstructural features, if any, to the macroscopic behavior. There is a pressing need to image the collagen microstructures in order to understand the mechanisms underlying this directional preference. Secondly, the layered structure of the ATAA wall was not

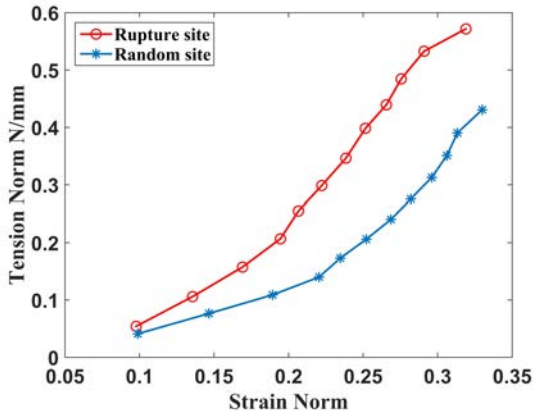

(a) Both energy and tension criteria worked

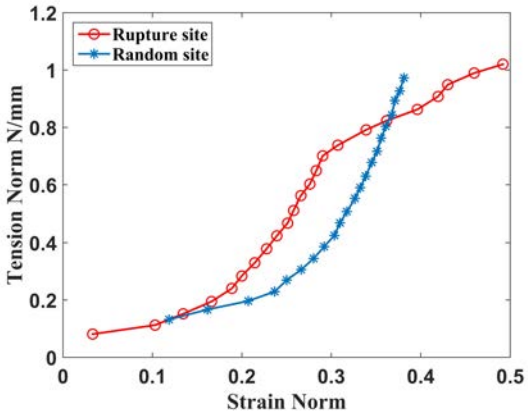

(b) Energy criterion worked

Figure 5.11: Two different tension-strain curves at rupture site and comparison to non-rupture sites

considered. The wall of the ATAA is composed of three distinct layers: the intima, media, and adventitia; each has different characteristics of collagen content and distribution. It has been reported that aortic dissection mostly initiates in the intima and media layers, indicating that the layered structure may play a role in determining the process of tissue failure[27]. The interplay between the layers and rupture was not investigated. It is not clear, for example, whether the tapering of the tension curve in Figure 5.11(b) was caused by the tearing of a layer. Moreover, there are no controls in the study, and thus it is unclear whether healthy ascending aorta follows the same or similar rupture pattern. On the technicality side, there could be a room to improve the identification of the rupture site and the measurement of orifice orientation. Some of them were determined from post rupture image and some were from

the prior image. Due to the inconsistency in image source and manual interferences at some steps, there is a certain level of uncertainty in the identified rupture location. However, as long as the orifice orientation is concerned, since the pattern is so pronounced, any improvement in image processing is unlikely to change the conclusion in any significant manner. It should also be noted that wall tension (the stress resultant over the thickness) was reported instead of the stress, because the wall thickness was not measured at enough points. Related to this, the stress work is the energy consumption per unit surface area, not per unit volume as typically specified in mechanics. Lastly, the data presented are limited by the small population size. More work is needed to confirm the observations.

In summary, the present study revealed some distinct features of ATAA rupture *in vitro*, under the inflation protocol. The initial rupture appears to occur at the position when the surface energy density reaches a threshold value. The tissue fractures preferentially in the direction of the highest stiffness, generating orifices that are locally transverse to the fiber direction. A possible implication is that the directional concentration of collagen content may not be the, at least not the only, determinant of the tissue strength. Instead, the microstructure of the collagen network may play a more important role. In the future, we plan to conduct imaging studies on ATAA microstructre, combining our macroscopic analysis with microstructural interrogation. This multiscale approach may shed light on understanding the mechanisms of ATAA rupture, and hopefully may help to develop better means of risk assessment.

CHAPTER 6
RELATIONSHIP BETWEEN STRENGTH AND ELASTIC PROPERTIES

In this chapter, we explore the relationship between the strength and elastic properties using machine learning. As indicated by many studies, there could exist significant relationships between indicators from tension-strain data and strength[63, 64, 117, 116]. However, these relationships, even if exist, could be hidden in high dimensional spaces and thus are difficult to find in traditional ways. This is the place where machine learning is expected to help. We have collected a large number of tension (the stress resultant over thickness) strain data and they were obtained at different locations in tissue specimens, some at or near sites where the tissue eventually ruptured and most from locations where the tissue remained intact. Therefore, classifying the tension-strain data and further exploring correlations between mechanical response and strength become possible. Also, machine learning techniques have shown a great promise in aneurysm biomechanics. To cite a few, Bisbal et al. used hemodynamic and morphologic together with clinical features to predict the rupture propensity of cerebral aneurysm[9]. Lee et al. utilized surface curvature as a machine learning feature, yielding a higher accuracy in classifying electively and emergent repaired abdominal aortic aneurysms compared to using the diameter criterion[72]. Liang et al. demonstrated that certain shape futures can be used to make predictions of risk scores consistent with finite element stress analysis [73].

Machine learning algorithms, including support vector machine and random

forest, were used to classify tension-strain curves obtained from rupture and non-rupture sites. Leveraging the information provided by the machine learning, we interrogated the rupture group to investigate relationships between the strength and response properties.

6.1 Method

6.1.1 Machine learning features

Tension-strain curves were obtained using inflation test and a pointwise identification method in previous chapters[23, 24, 84]. Three sets of features extracted from the tension-strain data were used to facilitate classification. The first is the constitutive parameters obtained by fitting the data to a nonlinear response function, which is introduced in Chapter 4. The second is geometric characteristics extracted from the curve of total tension versus total strain. These include the maximum curvature, the relative location of the maximum curvature, and the difference between the end and beginning slopes. The last one is combination of the first two. The rationale for selecting these features is explained later.

6.1.1.0.1 Constitutive parameters

The tension-strain data at each Gauss point were fitted to the GOH model as mentioned in Chapter 4. There are five material parameters in the model: $\mu_1, \mu_2, \gamma, \kappa, \theta$; at each Gauss point a set of these parameters were obtained. We used the first four as features for machine learning. The parameter θ, the angle the vector $\mathbf{M}$ makes to the horizontal line (the circumferential direction) , was excluded because it is not

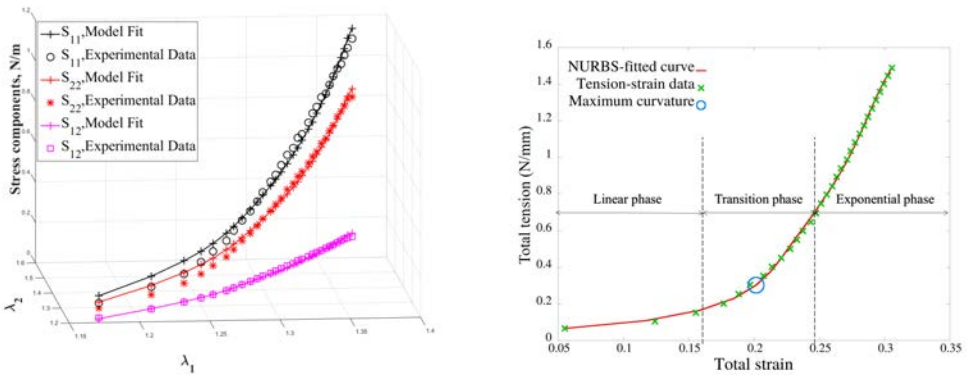

(a) (b)

Figure 6.1: (a) Tension-strain data and fitted response curves; (b) Total tension strain curve and illustration of response phases. In (a), S_{11}, S_{22} and S_{12} are the components of the membrane stress in a local surface basis.

intrinsic. It depends on the choice of coordinate axes. Each set of parameters was given a binary label according to the rupture and non-rupture state at the end. The ones at rupture sites were labeled RUPTURE (1), otherwise NON-RUPTURE (0). Each labeled set formed a material vector.

6.1.1.1 Curve geometry

The response of ATAA tissue typically contains three distinct phases: a nearly linear phase at the beginning, a transition phase in the middle, followed by an exponential-type response at large strains (see illustration in Figure 6.1b). The initial linear behavior is attributed to elastin and non-collagenous matrix. In this phase, the collagen remains crimped and contributes little to load-bearing. As the deformation

increases the collagen fibers are gradually recruited into load bearing, giving rise to the transition period. The exponential response at the later stage is almost entirely due to collagen which becomes taut at this stage [61]. Since elastin is significantly reduced in ATAA , collagen fibers may be recruited earlier, resulting in an early transition[65] and possibly a short transition period [116]. An early recruitment may lead to a quick build-up of stress and consequently, an early rupture. Thus rupture and non-rupture responses may have some distinct characteristics manifested in the tension-strain curve. The curvature of the curve may reflect how fast the recruitment is, and in particular, the position of the maximum curvature may suggest how early the transition occurs. Motivated by these conjectures, we used the maximum curvature and its relative location as geometric features. The difference between the slopes at the beginning and at the end of the curve, which could be a measure of the average curvature, was also included.

It was noted in [24] that, in our study while the GOH function yielded an excellent fit to the medium to high strain response, the fitting quality at low strains tended to be generally poorer. In addition, the values of μ_1 were orders of magnitude smaller that μ_2, making it less trustworthy. Thus, the transitional response may not be faithfully represented by the GOH function. In order to better capture the low strain response, we fitted the response to NURBS functions and then computed the curvature from the NURBS form. At each point, the total tension (i.e., the norm) and the total strain were fitted to a third order NURBS function with three knot intervals. The R^2 values for each curve were around 0.92. The third order NURBS

was employed because it provides a continuous second derivative.

The curvature is given by

$$\kappa = \frac{|f''(x)|}{(1 + (f'(x))^2)^{\frac{3}{2}}} \tag{6.1}$$

where x is the strain norm and $f(x)$ is the tension norm. The relative location of the maximum curvature is defined as

$$c = \frac{x_{mc} - x_{min}}{x_{max} - x_{min}} \tag{6.2}$$

where x_{max} and x_{min} are the two limits of strain range, and x_{mc} is the strain at which the maximum curvature occurs.

6.1.2 Classification by random forest

Random forest is an ensemble learning method popularly used for classification learning tasks[57, 58]. It operates by constructing a multitude of decision trees at training time and outputting the class that is the mode of the classes. Let random forest $\mathcal{F} = \{T_i, i = 1, ..., n\}$ be a set of trees. Each tree T_i in the random forest is trained on a random selection of training samples $\mathfrak{S} = \{\mathfrak{s}_i = (\mathfrak{x}_i, y_i)\}$, where $\mathfrak{x}_i \in R^n$ is the feature vector of training sample $\mathfrak{s}_i$, and y_i is the class label of the corresponding sample. Given a feature vector $\mathfrak{x}_i$, we defined the split function at each node as follows:

$$\begin{cases} \mathfrak{x}_i^{(j)} >= thresh, & \text{go to left child;} \\ otherwise, & \text{go to right child,} \end{cases} \tag{6.3}$$

where $\mathfrak{x}_i^{(j)}$ denotes the j^{th} dimension of vector $\mathfrak{x}_i$. At each splitting node, the classifier generates multiple hypothesized tests by randomly selecting a number of dimensions and thresholds. The one that gives the smallest score to the Gini impurity[11], which has been widely used in decision tree algorithm for selecting splitting attributes, is selected and stored to classify the new coming samples.

6.1.3 Classification by support vector machine(SVM)

A support vector machine (SVM) is a discriminative classifier formally defined by a separating hyperplane. In other words, given labeled training data, the algorithm outputs an optimal hyperplane which can categorize new examples. Given a training data set of n points of the form $(\mathfrak{x}_1, y_1), ..., (\mathfrak{x}_n, y_n)$ where the y_i are either 1 or -1, each indicating the class to which the point $\mathfrak{x}_i$ belongs(1 stands for rupture and -1 stands for non-rupture). Each $\mathfrak{x}_i$ is a $p-$dimensional real vector.

One seeks to find the "maximum-margin hyperplane" that divides the group of points $\mathfrak{x}_i$ for which $y_i = 1$ from the group of points for which $y_i = -1$, which is defined so that distance between the hyperplane and the nearest point $\mathfrak{x}_i$ from either group is maximized.

Any hyperplane can be written as the set of points $\mathfrak{x}$ satisfying

$$\omega \cdot \mathfrak{x} - b = 0, \tag{6.4}$$

where ω is the (not necessarily normalized) normal vector to the hyperplane. The parameter $\frac{b}{\|\omega\|}$ determines the offset of the hyperplane from the origin along the normal

vector ω. The problem is solved by transferring the problem to primal optimization problem, primal-dual problem[49, 19].

To approach better results, SVM employs the kernel trick to map large numbers of features in the input space to higher-dimensional space [59]. In this paper, a popular kernel called radial basis function kernel (RBF) was chosen. The RBF kernel on two samples $\mathfrak{x}_i$ and $\mathfrak{x}_j$, represented as feature vectors in some input space, is defined as

$$K(\mathfrak{x}_i, \mathfrak{x}_j) = \exp(-\frac{\parallel \mathfrak{x}_i - \mathfrak{x}_j \parallel^2}{2\sigma^2}) \tag{6.5}$$

$\parallel \mathfrak{x}_i - \mathfrak{x}_j \parallel^2$ may be recognized as the squared Euclidean distance between the two feature vectors. σ is a free parameter. An equivalent, but simpler, definition involves a parameter $\gamma = \frac{1}{2\sigma^2}$:

$$K(\mathfrak{x}_i, \mathfrak{x}_j) = \exp(-\gamma \parallel \mathfrak{x}_i - \mathfrak{x}_j \parallel^2) \tag{6.6}$$

6.1.4 Preprocessing of data

Features discussed in the previous section were extracted from 11925 tension-strain curves including 11520 non-rupture and 405 rupture. Compared to the total number of tension-strain curves (ntc), the proportion of rupture curves (nrc) is only $\sim$ 3% ($nrc << ntc$), which leads to the non-rupture members being more likely recognized for any machine learning algorithm. To circumvent this issue, we randomly sampled the same amount of curves as rupture curves from non-rupture group for m times. Each sampling group is combined with the rupture group to form a test set. In this set, the number of rupture curves equals to the number of non-rupture curves.

Theoretically, when m is sufficiently large, all the non-rupture information will be included. In this paper, the sampling procedure repeated 50 times. All newly formed data sets were tested by the random forest algorithm to develop the classification model.

6.1.5 N-fold cross validation

The classification was carried out using a ten-fold cross validation [125]. In an N-fold cross validation, the original data was randomly partitioned into N equal sized subsets. A single, non-labeled subset is retained as the validation data, and the remaining N-1 subsets are used as training data. The cross validation process is then repeated N times (the folds), with each of the N subsets used exactly once as the validation data. The N results from the folds are averaged to produce a single estimation. Ten-fold cross validation is the most commonly used [88]. It was adopted in this study and was performed individually to every sampling set generated by the preprocessing.

6.2 Results

A machine learning library, Scikit-learn, was employed in the study[95]. Precision, recall, specificity were used to measure the performance. Shortly, the precision is the proportion of instances in a given class which are correctly classified. The recall value, also known as sensitivity, measures the proportion of positives which are correctly identified. The specificity is the proportion of negatives which are correctly identified. Before testing, the choice of algorithmic parameters is critical since they

have a great impact on the precision. Therefore, algorithmic parameters choosing procedures are presented in the results section as well.

6.2.1 Performance of random forest

Classifications were performed separately over three groups of features. The first set was the elastic parameters $(\mu_1, \mu_2, \gamma, \kappa)$, the second was the geometric parameters (the maximum curvature, the maximum curvature location, the slope difference), and the third group was the union of these two. The performances were summarized in this section. In the random forest, the adequate number of trees must be determined first. Typically, training precision improves with the number of trees and stabilizes when the number reaches a certain level. As we can see from Figure 6.2, precision and recall stabilized at around fifty trees for both cases. Therefore, performance results of both cases were calculated at the number of trees set to fifty.

The ten-fold cross validation results are summarized in Table 6.1. There are two sets of outcomes for each feature group; one considers rupture as positive and the other one treats non-rupture as positive.

6.2.2 Performance of support vector machine(SVM)

There are two parameters in the radial basis function kernel (RBF) SVM: γ and C. The γ parameter defines how far the influence of a single training example reaches, with low values meaning 'far' and high values meaning 'close'. The γ parameters can be seen as the inverse of the radius of influence of samples selected by the model as support vectors. To be noticed, the γ parameter is different from the γ in the GOH

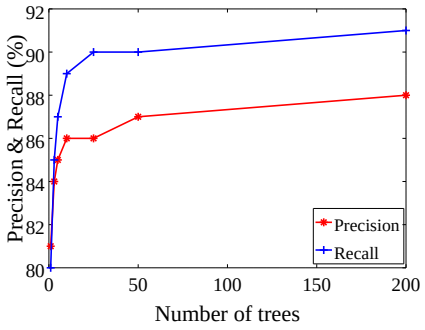

(a) Constitutive parameters

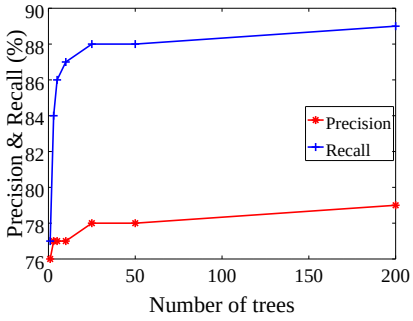

(b) Geometric characteristics

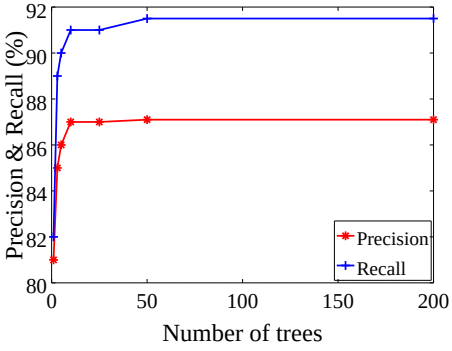

(c) Combined parameters

Figure 6.2: Precision and recall versus number of trees

model. The C parameter trades off misclassification of training examples against simplicity of the decision surface. A low C makes the decision surface smooth, while a high C aims at classifying all training examples correctly by giving the model freedom to select more samples as support vectors.

6.2.2.1 Constitutive parameters

To determine suitable SVM algorithm parameters, a grid table formed by $C = [1, 10, 100, 1000]$ and $\gamma = [1, 10, 100, 1000]$ was tested and presented in Table 6.2.

Table 6.1: Performance of random forest (mean±sdv)

	Precision	Recall	Specificity	Class
Constitutive parameters(CP)	87± 1.2	90± 2.1	85± 1.1	R
	89± 1.5	85± 1.1	90± 2.1	NR
Curve geometry(CG)	78± 1.3	88± 1.4	75± 1.3	R
	86± 1.4	75± 1.3	88± 1.4	NR
CP & CG	87± 1.2	94± 2.2	87± 1.3	R
	93± 1.6	87± 1.3	94± 2.2	NR

*R: Rupture; NR: Non-rupture

Table 6.2: Grid search results (precision, recall in %) for γ & C in RBF kernel SVM

γ \ C	1	10	100	1000
1	(55,99)	(60,93)	(61,92)	(64,88)
10	(62,92)	(70,85)	(76,86)	(81,87)
100	(82,85)	(84,89)	(86,91)	(86,91)
1000	(87,88)	(87,90)	(86,88)	(86,87)

As can be seen from the table, the accuracy results are indeed sensitive with γ and $C = 10, \gamma = 1000$ gives the best precision and recall results, which are 87% and 90% respectively. Therefore, for material properties feature, we took $C = 10, \gamma = 1000$ for all cases.

Table 6.3 presents the ten-fold cross validation results from SVM classifier with using constitutive parameters. As we can see from the table, in terms of rupture class, SVM with RBF kernel function gives 88% precision and 89% recall.

Table 6.3: Performance of material properties (in%)

	Precision	Recall	Specificity	Class
SVM (linear)	56±2.4	95±2.3	24±1.5	R
	88±1.1	24±1.5	95±2.3	NR
SVM (RBF)	87±1.2	90±2.2	88±1.3	R
	88±1.2	88±1.3	90±2.2	NR

Table 6.4: Grid search results (precision, recall in %) for γ & C in RBF kernel SVM

γ \ C	1	10	100	1000
1	(63,86)	(66,94)	(69,97)	(72,96)
10	(71,96)	(75,95)	(77,94)	(78,95)
100	(78,95)	(80,96)	(82,94)	(83,91)
1000	(86,87)	(86,87)	(86,84)	(85,83)

6.2.2.2 Curve geometry

Results from the curve geometry are summarized in this section. As discussed in the previous section, the classifiers' algorithmic parameters were determined first. Grid search results of C and γ for RBF kernel SVM are presented in Table 6.4. It can be determined from the table that optimal combination for curve geometric features is $C = 100$ and $\gamma = 100$, and the accuracy results are sensitive with γ as well.

The performances of the classification under the selected parameters are summarized in Table 6.5. The best precision and recall results are 82% and 94%, which are offered by SVM with RBF kernel classifier.

Table 6.5: Performance of curvature geometric features (in%)

	Precision	Recall	Specificity	Class
SVM (linear)	65±1.4	73±1.2	61±1.3	R
	71±1.3	61±1.3	73±1.2	NR
SVM (RBF)	82±1.4	94±2.0	81±1.5	R
	91±1.7	81±1.5	94±2.0	NR

Table 6.6: Grid search results (precision, recall in %) for γ & C in RBF kernel SVM

γ \ C	1	10	100	1000
1	(70,95)	(76,94)	(80,95)	(85,96)
10	(81,96)	(86,97)	(89,98)	(91,98)
100	(90,97)	(92,97)	(92,98)	(92,98)
1000	(95,84)	(96,86)	(96,86)	(96,86)

6.2.2.3 Union of constitutive parameters and curve geometric characteristics

Like previous procedures, grid search results for SVM with RBF kernel are presented firstly. The results of C and γ for RBF kernel SVM are presented in Table 6.6. It can be determined from the table that optimal combination for curve geometric features is $C = 100$ and $\gamma = 100$

Table 6.7 presents the results from SVM classifier with using the union parameters. As we can see from the table, in terms of rupture class, SVM with RBF kernel function gives 92% precision and 98% recall which are the best performance. Compared to constitutive parameters and curve geometric characteristics, the preci-

Table 6.7: Performance of union features (in%)

	Precision	Recall	Specificity	Class
SVM (linear)	72±1.5	90±2.0	64±1.3	R
	87±1.5	64±1.3	90±2.0	NR
SVM (RBF)	92±2.1	98±1.4	92±1.3	R
	97±1.6	92±1.3	98±1.4	NR

sion and recall values of union parameters set improve to 92% and 98%, which may indicate that the higher feature dimension offers better hyper-plane that can separate the groups.

6.2.3 Implication of feature importance from random forest

Gini importance, which is defined as the total decrease in node impurity averaged over all trees of the ensemble, is an indicator of the weight of each individual feature in classification decision[10]. The importance values are presented in Table 6.8. As we can see from Table 6.8, the parameter γ, which is the exponential index in Equation 4.1, is the most important classification factor among the constitutive parameters and the maximum curvature location is the most important parameter among the geometric features. These two factors remain most influential among the seven parameters when the constitutive parameters and curve geometry were considered together, with γ ranks slightly higher.

The importance values in Table 6.8 suggest that members in the rupture group could have some distinct characteristics that have to do with the exponential parameter γ and the location of maximum curvature. To explore this, we first examined

Table 6.8: Feature importances

Constitutive parameters(CP)	μ_1	μ_2	γ	κ			
Importance	9%	29%	38%	24%			
Curve geometry(CG)	MC	MCL	SD				
Importance	20%	46%	34%				
CP & CG	μ_1	μ_2	γ	κ	MC	MCL	SD
Importance	2%	13%	28%	8%	9%	25%	16%

*MC: maximum curvature; MCL: maximum curvature location; SD: stiffness difference

the distribution of γ. Figure 6.3 presents the histograms of γ in the rupture and non-rupture groups. The figures show that γ in the rupture group is clustered in a narrow band compared to the non-rupture group. In other words, the γ values of all curves in the rupture group are close. If we regard the actual response as exponential (namely $\frac{dS}{dE} \propto S$) in the final stage of response, then, similar γ values would mean that the ratio between the maximum tension (the tension at the end) and the stiffness at the end should also be similar. Indeed, a linear correlation between the maximum tension and the end stiffness was observed, as shown in Figure 6.6.

Similar to γ, the values of the relative location of maximum curvature, c, are also banded although not as sharp as γ. Histograms of the actual stain values at the maximum curvature location are presented in Figure 6.4. Note that we plotted the strain instead of the relative location because this may facilitate a direct comparison with other works in the literature. Examining the tension at the maximum curvature location, it is observed that the tension correlates linearly with the maximum tension (Figure 6.5).

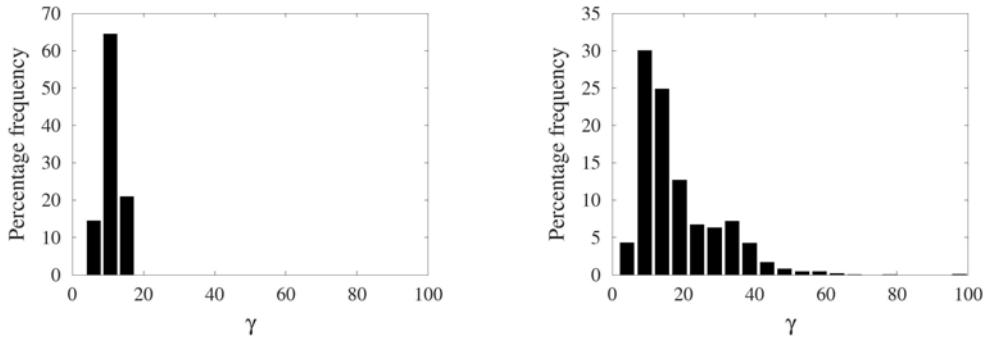

(a) Rupture group (b) Non-rupture group

Figure 6.3: γ distribution

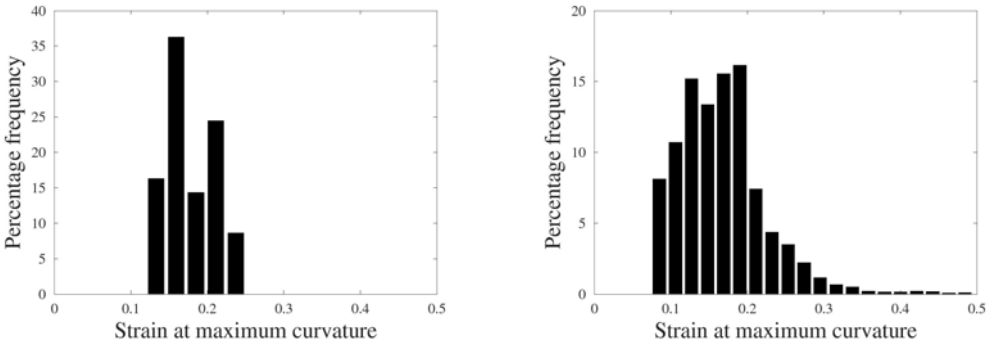

(a) Rupture group (b) Non-rupture group

Figure 6.4: Distribution of strain values at maximum curvature location

6.3 Discussion and Conclusion

The mechanism of ATAA rupture remains poorly understood, making it difficult to assess the rupture risk of diagnosed ATAAs. The difficulty is aggregated by lack of reliable information about the tissues strength at patient-specific level. While it is now routine to predict the wall tension (or stress) using mechanical analysis

based on patient-specific geometry, it is impossible to obtain the tissue strength *in vivo*. The overarching goal of this work is to explore possible linkage between the strength and measurable response. If such relationships exist, it might be possible to infer the strength indirectly from measurable features. Nowadays 4D CT or MRI scans allow the dynamic motion of aneurysm wall to be recorded and hence the wall strain to be inferred. Although the resolution of routine diagnostic scans may not be enough to fully resolve the wall motion, it is expected that the gap can be soon filled by the advance of technology. The wall stress can be reasonably estimated from *in vivo* surface geometry and the blood pressure without invoking the elastic property of the tissue [76, 89, 77, 135]. Thus, it is reasonable to expect the tensions and strain data in the physiological pressure range to be made available. If the strength is indeed related to response features, one might be able to estimate the strength or alternatively, to use some features as surrogate. Machine learning lends itself naturally to the task of exploring such relations.

In this study, we utilized random forest and support vector machine (SVM) to classify rupture and non-rupture tension-strain curves. For random forest, we obtained 87% precision using constitutive parameters, 78% precision using geometric characteristics, 87% precision when the toe sets features were combined together. For SVM with RBF kernel, the precisions of using the three feature sets are, 87%, 82% and 92% respectively. In overall the classification results are decent. The moderate success indicates that the end state of each curve (rupture or non-rupture) can be reasonably differentiated based on response characteristics. Note that we deliberately

excluded features that may be directly associated with rupture (for example the end tension), except for the end stiffness. The results thus suggest that the end state can be differentiated using characteristics of pre-rupture response.

Within the constitutive parameters, γ showed the highest score of importance. For members in the rupture group, nearly 70% of the γ values fall into the range of 8 to 12, while only about 30% in the non-rupture group are in this range. The values of γ in the non-rupture group spread much wider. The implication of a uniform γ is that the strength correlates linearly with the end stiffness at rupture locations(Figure 6.6a). The correlation also exists in non-rupture group, as shown in Figure 6.6b, but with significantly lower slope. It indicates that the algorithm indeed successfully detected a distinct characteristic of the rupture group. This result is consistent the finding in [63], which reached the same conclusion using uniaxial tension test. A similar finding was reported for aortic root aneurysms in [64]. It should be noted that, despite the lower frequency of γ appearance from the non-rupture group, there is still a significant number of non-rupture members in the γ range of the rupture group, due to the sheer size of the non-rupture group. Thus the classification was unlikely made based on γ alone. In other words, γ itself is insufficient for distinguishing responses.

Another key parameter picked out by the machine learning is the location of maximum curvature, c. As alluded earlier, this parameter might be an indicator of how quick the collagen recruitment happens. It is remarkable that the tension at the maximum curvature location correlates significantly with the strength (Figure 6.5a) at rupture locations. Although this parameter in the rupture group is not as tightly

concentrated as γ, it is still banded compared to the non-rupture group. That might explain that, the maximum curvature location correlates also well with the strength at non-rupture locations(Figure 6.6b), and the slopes of both relations are almost the same. Sugita et al. reported that the ATAA strength correlates strongly with the stress at which tangent elastic modulus reaches 63% of the plateau level[117, 116]. The present finding is in congruence with these reports. The finding suggests that tension at the maximum curvature may be a surrogate for the strength. A typical aorta of 5 cm diameter under the physiological blood pressure range of 11-16 kPa would bear a wall tension of 0.28-0.40 N/mm according to Laplace law[114]. We checked several randomly selected curves and found that the tension values at the maximum curvature were within or close to this range. The linear regression in Figure 6.5 shows that the tension at the maximum curvature is approximately 4.4 times below the strength. This tension is much more likely to be reached during the physiological motion.

When the elastic parameters and curve geometry were considered together, the classification identified γ and the location of maximum curvature as the leading features. The outcome is consistent with the individual cases. The stiffness difference (in effect, the end stiffness because the initial stiffness is small) was ranked the third with an importance score of 16%. This is again a confirmation of the linear correlation reported in [63, 64]. It is interesting to note that the stiffness parameter μ_2, a key determinant of the stiffness, was not identified as a leading feature for rupture.

There are several limitations in this study. First, although we used approxi-

mately ten thousands tension-strain curves, they were harvested from 10 samples out of 6 patients in relatively uniform age group. As reported in the literature, patients' age [31, 92, 65, 35], gender [110, 34], disease conditions [92, 87, 96, 43, 41, 5, 126, 43], and aortic valve phenotype [92, 97, 96, 41], can have significant influence on ATAA properties. The samples used in the study certainly do not cover a sufficiently wide range of patient types. The age factor was not considered because the population size was too small. Other risk factors mentioned above were not considered due to lack of information. In addition, the curves were harnessed from small samples, the exact locations of which were not known to this study. Given that the ATAA properties vary regionally [92, 63, 35], tissue samples recruited into study should cover all necessary regions of interest. These limitation should be kept in mind when interpreting the findings. With regard to the mechanical model, the ATAA was treated as mono-layer, the layer heterogeneity, which could be important to rupture and dissection[92, 112], was ignored. The mono-layer assumption also led to the negligence of residual stress, although the influences of residual stress could be small because the samples were already cut open. Also, we have used a version of GOH model that considered only one prominent fiber direction. Other forms of GOH function such as the ones employed in [42] that contains two families of fibers may also be considered in future work.

Secondly, more response features may need to be considered. It is noted that using the three geometric features yielded 78% precision, which may be indicative of an insufficient featuring. More features, such as tension and strain range, energy absorption etc may be considered in future. Combination of response features with

clinical and pathological factors such as the ones investigated in [35] could be more informative. More machine learning classifiers may need to be tested. Pattern recognition classifier, such as convolutional neural network (CNN) has been reported its excellent capability on image classification [109, 52]. It was not used due to its high computational cost. Last but not least, it should be noted that, although the parameter γ and the relative location of the maximum curvature were found significant, they along are not sufficient for classification, let alone prediction.

In concluding, the present contribution leveraged the large amount of tension-strain curves from a previous work to investigate correlations between the strength and response features. Machine learning was used to classify the data and provide insight on the importance of the features. The work showed that the rupture and non-rupture states can indeed be classified using pre-rupture response features. Inspired by the importance scores, the rupture groups was interrogated and some strong correlations between the strength and the response features were revealed. In particular, it was found that the strength correlates strongly with the tension at the point where the curvature of the total tension strain curve attains maximum, which occurs early in the response. It also confirmed that the strength correlates linearly with the end stiffness. The work is an exploratory step towards non-invasive estimation of the ATAA strength. The results, although preliminary, appear promising.

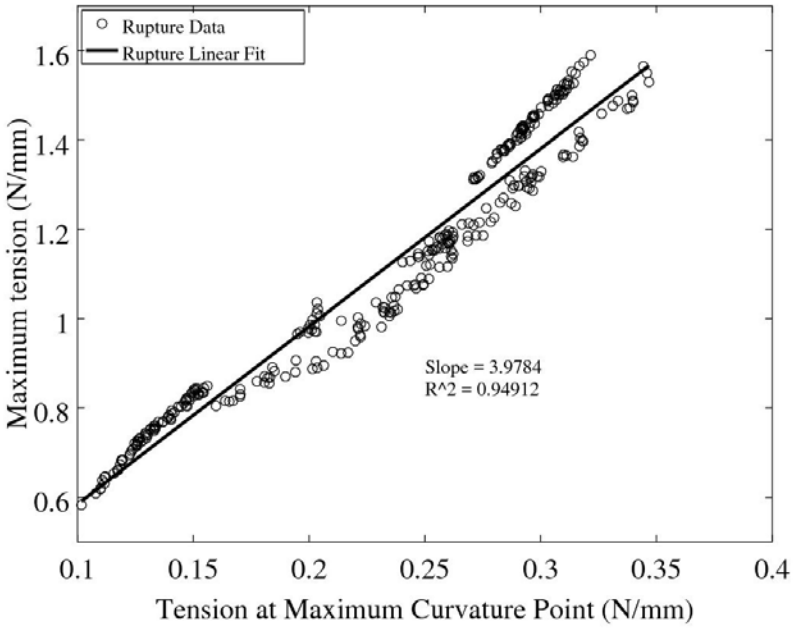

(a) Rupture group

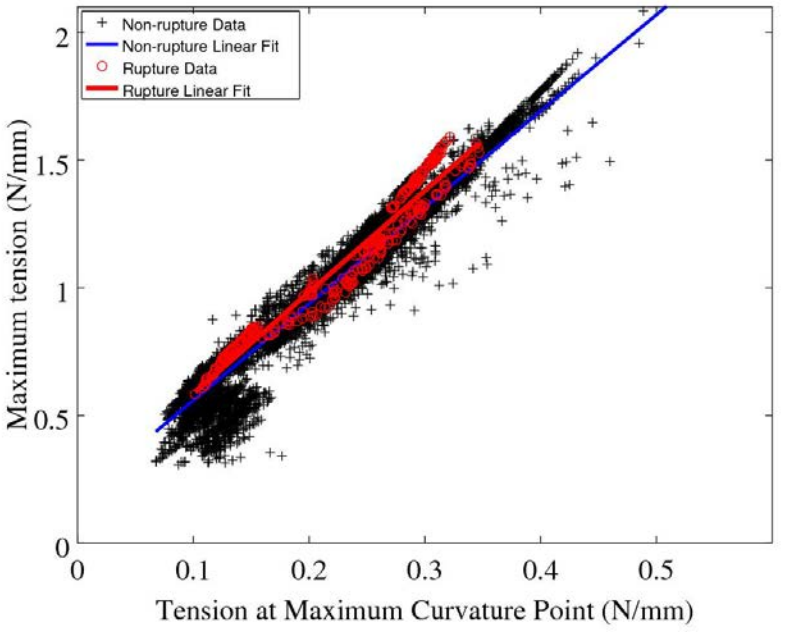

(b) Rupture & Non-rupture group

Figure 6.5: Maximum tension vs tension at the maximum curvature location

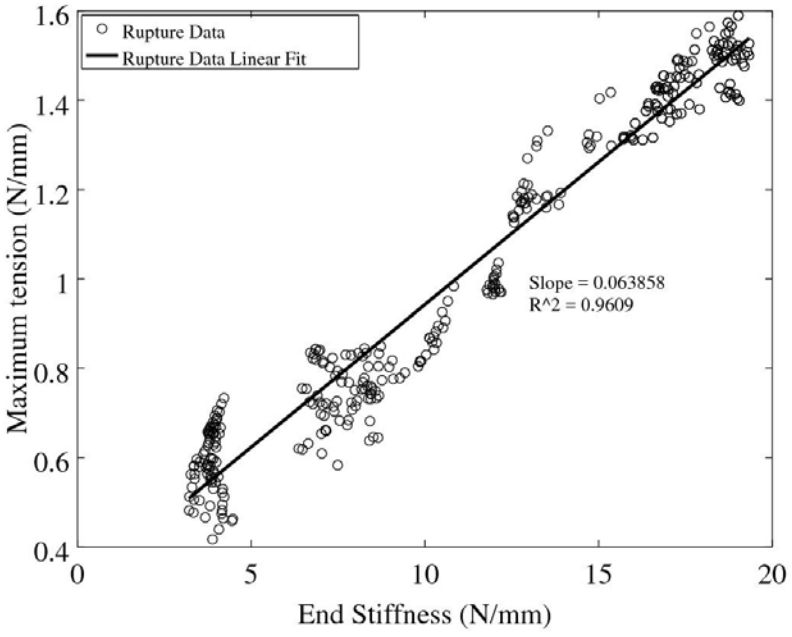

(a) Rupture group

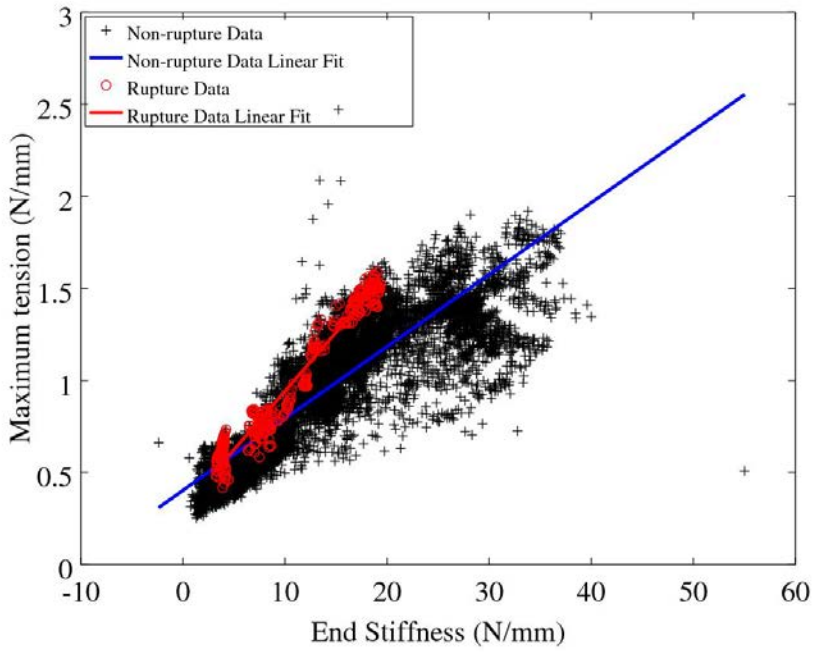

(b) Rupture & Non-rupture group

Figure 6.6: Maximum tension vs end stiffness

CHAPTER 7
CONCLUSIONS

7.1 Summary

This thesis is motivated by the demand of delineating the local heterogeneous conditions of ATAAs, the need of possible patterns is the mechanical behavior that are suggestive of high rupture risk and further establish possible link between the obtained tension-strain response and strength of ATAAs. The protocol developed in this work integrates Digital Image Correction, inflation test, the inverse stress analysis methodology and machine learning technique, enabling the identification of full-field stress, strain and mechanical properties without being limited by the complexity of the tissue heterogeneity. The major contributions of this work are as follows.

1. The heterogeneous properties in 9 human ATAA samples based on full-field stress and strain data acquired from inverse stress analysis and DIC measurements have been identified. The material properties are resolved to the spatial resolution approximately 0.3 mm. The heterogeneous properties were validated by forward analyses, and verified that the properties can replicate not only the global deformation and also the local stress and strain patterns. Inter- and intra- patient properties study evidents that ATAAs are highly heterogeneous. There is a significant level of property variation even within samples of 2 cm in diameter.
2. The membrane assumption is verified by a numerical simulation performed in

Abaqus as well. Results from continue shell element and inverse membrane element were compared and showed that it is appropriate to treat the inflated specimen as membranes, at least for the majority of the pressurized states.

3. Some patterns of the mechanical condition at the rupture sites are revealed. The most striking pattern is that the cracks are preferentially transverse to the fiber direction - the direction of the highest stiffness. In all but one case the orifice normal is parallel to the local fiber direction. Not only that, the cracks propagated transversely to the fiber direction as well, in some cases resulting in curved orifices. This finding may shed light on designing micromechanical studies on ATAA tissue rupture.

4. The toughness is a more reliable criterion for rupture prediction, in the sense that the location of peak energy matched the rupture site better and the peak tension. It concurrently considers both tension and strain and therefore can handle more situations than tension alone.

5. Based on the importance scores provided by the machine learning, implications of some features were interrogated. It was found that the value of γ in GOH model is nearly the same for all members in the rupture group. This indicates that the strength correlates linearly with the end stiffness. In addition, it was found that there is a strong correlation between the strength and the tension at the maximum curvature point of the tension-strain curve. The findings suggest that the strength, which is not available without rupturing the tissue, may be indirectly inferred from pre-rupture response features.

7.2 Future work

By far, this work has successfully (1) determined the local heterogeneity of the ATAA tissue, (2) identified that the toughness could be a potential rupture location indicator and (3) delineated that the crack opens transversely along predicted fiber direction. (4) found strong correlations between the strength and a particular tension in the early stage of response as well as with the end stiffness. To approach the goals of understanding the ATAAs' mechanical characteristics and helping on clinical diagnosis, several tasks that will be pursued in the future:

1. Improvements of current method. As mentioned in previous sections, there are still rooms to improve the current method. For instance, the used GOH model has inferior fitting at low pressure stages, which indicates that the model does not adequately describe the deformation in the early phase of the response. More material models, such as two fiber family model etc., can be tested to seek for improvements[94]. Also, for the machine learning, there are still more mechanical features can be used to help on classification. For example, the high toughness spot we found in the Chapter 5 which matches the rupture location well, can potentially be a good feature since it now can distinguish rupture site from others. Overall, improving the current method can help us to understand more the rupture characteristics of the ATAA tissues.

2. Investigating rupture process. Current experiment determines the rupture initialization location and propagation direction by post rupture images, which may introduce some inaccuracies. To investigate the rupture process, current

setup can be kept except switching the camera to high speed one. The high speed camera will be used to precisely capture the entire inflation procedure from beginning to rupture. In this way, the accurate crack initialization location and propagation direction can be recorded. In the meantime, aforementioned mechanical characteristics, such as toughness, fiber direction, will be calculated used the proposed method. The results later can be used to compare with the recorded ones then help on understanding the rupture of ATAA.

3. *in vivo* characteristics. The method proposed in this method takes the surface motions as input to obtain mechanical characteristics. If there is a way to access aorta motions *in vivo*, the method can be directly applied to compute the related characteristics. In this way, the results may be more trustworthy for clinical diagnosis. Four-dimensional computed tomography(4D CT) has been proposed to provide more valuable information on the shapes and trajectories of human organ since 1992. It can capture dynamic motion of human organ *in vivo*, which could possibly provide aorta deformation motions. If so, the proposed method can be directly used to collect a large database of human aorta mechanical characteristics, which will no doubt help on the rupture predicting. Therefore, to seek help from 4D CT scan will be the most valuable move at the next stage of the work.

REFERENCES

[1] JE Adkins. A reciprocal property of the finite plane strain equations. *Journal of the Mechanics and Physics of Solids*, 6(4):267–275, 1958.

[2] Andrea Avanzini, Davide Battini, Lorenzo Bagozzi, and Gianluigi Bisleri. Biomechanical evaluation of ascending aortic aneurysms. *BioMed Research International*, 2014, 2014.

[3] Ali N Azadani, Sam Chitsaz, Alex Mannion, Aart Mookhoek, Andrew Wisneski, Julius M Guccione, Michael D Hope, Liang Ge, and Elaine E Tseng. Biomechanical properties of human ascending thoracic aortic aneurysms. *Annals of Thoracic Surgery*, 96:50–58, 2013.

[4] Ali N Azadani, Sam Chitsaz, Peter B Matthews, Nicolas Jaussaud, James Leung, Tonia Tsinman, Liang Ge, and Elaine E Tseng. Comparison of Mechanical Properties of Human Ascending Aorta and Aortic Sinuses. *The Annals of Thoracic Surgery*, 93:87–94, 2012.

[5] Anju R Babu, Achu G Byju, and Namrata Gundiah. Biomechanical properties of human ascending thoracic aortic dissections. *Journal of Biomechanical Engineering*, 137(8):081013, 2015.

[6] R Bartels, J Beatty, and B Barsky. An introduction to splines for use in computer graphics & geometric modeling morgan kaufmann publishers, 1987.

[7] Ted Belytschko, Yury Krongauz, Daniel Organ, Mark Fleming, and Petr Krysl. Meshless methods: an overview and recent developments. *Computer Methods in Applied Mechanics and Engineering*, 139(1):3–47, 1996.

[8] Panagiotis Berillis. The role of collagen in the aortas structure. *The Open Circulation and Vascular Journal*, pages 1–8, 2013.

[9] Jesus Bisbal, Gerhard Engelbrecht, Mari-Cruz Villa-Uriol, and Alejandro F Frangi. Prediction of cerebral aneurysm rupture using hemodynamic, morphologic and clinical features: a data mining approach. In *International Conference on Database and Expert Systems Applications*, pages 59–73. Springer, 2011.

[10] L Friedman Breiman, JH Friedman, Stone Olshen, and C Stone. CJ, 1984. Classification and Regression Trees. *Pacific Grove, Kalifornien*, 1983.

[11] Leo Breiman, Jerome Friedman, Charles J Stone, and Richard A Olshen. *Classification and Regression Trees*. CRC Press, 1984.

[12] M. Carmo, L. Colombo, A. Bruno, F. R. M. Corsi, L. Roncoroni, M. S. Cuttin, F. Radice, E. Mussini, and P. G. Settembrini. Alteration of elastin, collagen and their cross-links in abdominal aortic aneurysms. *European Journal of Vascular and Endovascular Surgery*, 23:543–549, 2002.

[13] P Chadwick. Applications of an energy-momentum tensor in non-linear elastostatics. *Journal of Elasticity*, 5(3-4):249–258, 1975.

[14] Katherine H Chau and John a Elefteriades. Natural history of thoracic aortic aneurysms: size matters, plus moving beyond size. *Progress in Cardiovascular Diseases*, 56(1):74–80, 2013.

[15] Nusrat Choudhury, Olivier Bouchot, Leonie Rouleau, Dominique Tremblay, Raymond Cartier, Jagdish Butany, Rosaire Mongrain, and Richard L. Leask. Local mechanical and structural properties of healthy and diseased human ascending aorta tissue. *Cardiovascular Pathology*, 18:83–91, 2009.

[16] William Darrin Clouse, John W Hallett Jr, Hartzell V Schaff, Michelle M Gayari, Duane M Ilstrup, and L Joseph Melton III. Improved prognosis of thoracic aortic aneurysms: a population-based study. *Jama*, 280(22):1926–1929, 1998.

[17] Michael A Coady, John A Rizzo, Graeme L Hammond, Gary S Kopf, and John A Elefteriades. Surgical intervention criteria for thoracic aortic aneurysms: a study of growth rates and complications. *The Annals of Thoracic Surgery*, 67(6):1922–1926, 1999.

[18] Michael A Coady, John a Rizzo, Graeme L Hammond, Divakar Mandapati, Umer Darr, Gary S Kopf, and John A Elefteriades. What is the appropriate size criterion for resection of thoracic aortic aneurysms? *The Journal of Thoracic and Cardiovascular Surgery*, 113(3):476–91; discussion 489–91, March 1997.

[19] Corinna Cortes and Vladimir Vapnik. Support-vector networks. *Machine Learning*, 20(3):273–297, 1995.

[20] Baptiste Coudrillier, Jing Tian, Stephen Alexander, Kristin M Myers, Harry A Quigley, and Thao D Nguyen. Biomechanics of the human posterior sclera: Age- and glaucoma-related changes measured using inflation testingscleral biomechanical changes with age/glaucoma. *Investigative Ophthalmology & Visual Science*, 53(4):1714–1728, 2012.

[21] Ryan R Davies, Lee J Goldstein, Michael A Coady, Shawn L Tittle, John A Rizzo, Gary S Kopf, and John A Elefteriades. Yearly rupture or dissection rates for thoracic aortic aneurysms: simple prediction based on size. *The Annals of Thoracic Surgery*, 73(1):17–28, 2002.

[22] Frances M Davis, Yuanming Luo, Stéphane Avril, Ambroise Duprey, and Jia Lu. Pointwise characterization of the elastic properties of planar soft tissues: application to ascending thoracic aneurysms. *Biomechanics and Modeling in Mechanobiology*, 14(5):967–978, 2015.

[23] Frances M Davis, Yuanming Luo, Stéphane Avril, Ambroise Duprey, and Jia Lu. Pointwise characterization of the elastic properties of planar soft tissues: application to ascending thoracic aneurysms. *Biomechanics and Modeling in Mechanobiology*, 14:967–978, 2015.

[24] Frances M Davis, Yuanming Luo, Stéphane Avril, Ambroise Duprey, and Jia Lu. Local mechanical properties of human ascending thoracic aneurysms. *Journal of the Mechanical Behavior of Biomedical Materials*, 61:235–249, 2016.

[25] Carl De Boor, Carl De Boor, Etats-Unis Mathématicien, Carl De Boor, and Carl De Boor. *A practical guide to splines*, volume 27. Springer-Verlag New York, 1978.

[26] Luciano de Figueiredo Borges, Rodrigo Gibin Jaldin, Ricardo Ribeiro Dias, Noedir Antonio Groppo Stolf, Jean-Baptiste Michel, and Paulo Sampaio Gutierrez. Collagen is reduced and disrupted in human aneurysms and dissections of ascending aorta. *Human Pathology*, 39:437–443, 2008.

[27] Roman W DeSanctis, Robert M Doroghazi, W Gerald Austen, and Mortimer J Buckley. Aortic dissection. *New England Journal of Medicine*, 317(17):1060–1067, 1987.

[28] Marek P Ehrlich, M Arisan Ergin, Jock N McCullough, Steven L Lansman, Jan D Galla, Carol A Bodian, Anil Apaydin, and Randall B Griepp. Results of immediate surgical treatment of all acute type a dissections. *Circulation*, 102(suppl 3):Iii–248, 2000.

[29] John A Elefteriades. Natural history of thoracic aortic aneurysms: indications for surgery, and surgical versus nonsurgical risks. *The Annals of Thoracic Surgery*, 74(5):S1877–S1880, 2002.

[30] John A Elefteriades. Thoracic aortic aneurysm: reading the enemy's playbook. *Current Problems in Cardiology*, 33(5):203–277, 2008.

[31] John A Elefteriades and Emily A Farkas. Thoracic aortic aneurysm. *Journal of the American College of Cardiology*, 55(9):841–857, 2010.

[32] John a Elefteriades and Emily a Farkas. Thoracic aortic aneurysm clinically pertinent controversies and uncertainties. *Journal of the American College of Cardiology*, 55(9):841–57, March 2010.

[33] Gerald Farin. *Curves and surfaces for computer-aided geometric design: a practical guide*. Elsevier, 2014.

[34] Anna Ferrara, Simone Morganti, Pasquale Totaro, Alessandro Mazzola, and Ferdinando Auricchio. Human dilated ascending aorta: mechanical characterization via uniaxial tensile tests. *Journal of the Mechanical Behavior of Biomedical Materials*, 53:257–271, 2016.

[35] Anna Ferrara, Pasquale Totaro, Simone Morganti, and Ferdinando Auricchio. Effects of clinico-pathological risk factors on in-vitro mechanical properties of human dilated ascending aorta. *Journal of the Mechanical Behavior of Biomedical Materials*, 77:1–11, 2018.

[36] J Ferruzzi, DA Vorp, and JD Humphrey. On constitutive descriptors of the biaxial mechanical behaviour of human abdominal aorta and aneurysms. *Journal of the Royal Society Interface*, 8(56):435–450, 2011.

[37] Mark F Fillinger, Steven P Marra, ML Raghavan, and Francis E Kennedy. Prediction of rupture risk in abdominal aortic aneurysm during observation: wall stress versus diameter. *Journal of Vascular Surgery*, 37(4):724–732, 2003.

[38] Mark F Fillinger, ML Raghavan, Steven P Marra, Jack L Cronenwett, and Francis E Kennedy. In vivo analysis of mechanical wall stress and abdominal aortic aneurysm rupture risk. *Journal of Vascular Surgery*, 36(3):589–597, 2002.

[39] Centers for Disease Control, Prevention, et al. National center for injury prevention and control. *Web-based Injury Statistics Query and Reporting System (WISQARS)[online]*, 2005.

[40] HO Foster. Very large deformations of axially symmetrical membranes made of neo-hookean materials. *International Journal of Engineering Science*, 5(1):95–117, 1967.

[41] Claudio M García-Herrera, JM Atienza, FJ Rojo, Els Claes, GV Guinea, Diego J Celentano, C García-Montero, and RL Burgos. Mechanical behaviour and rupture of normal and pathological human ascending aortic wall. *Medical & Biological Engineering & Computing*, 50(6):559–566, 2012.

[42] Claudio M García-Herrera, Claudio A Bustos, Diego J Celentano, and Roberto Ortega. Mechanical analysis of the ring opening test applied to human ascending aortas. *Computer Methods in Biomechanics and Biomedical Engineering*, 19(16):1738–1748, 2016.

[43] Claudio M García-Herrera, Diego J Celentano, and Emilio A Herrera. Modelling and numerical simulation of the in vivo mechanical response of the ascending aortic aneurysm in marfan syndrome. *Medical & Biological Engineering & Computing*, 55(3):419–428, 2017.

[44] T Christian Gasser, Ray W Ogden, and Gerhard a Holzapfel. Hyperelastic modelling of arterial layers with distributed collagen fibre orientations. *Journal of the Royal Society Interface*, 3(6):15–35, March 2006.

[45] Jonathan P Vande Geest, Michael S Sacks, and David A Vorp. The effects of aneurysm on the biaxial mechanical behavior of human abdominal aorta. *Journal of Biomechanics*, 39(7):1324–1334, 2006.

[46] Sanjay Govindjee and Paul A Mihalic. Computational methods for inverse finite elastostatics. *Computer Methods in Applied Mechanics and Engineering*, 136(1):47–57, 1996.

[47] Sanjay Govindjee and Paul A Mihalic. Computational methods for inverse deformations in quasi-incompressible finite elasticity. *International Journal for Numerical Methods in Engineering*, 43(5):821–838, 1998.

[48] Albert E Green and Ronald S Rivlin. On cauchys equations of motion. In *Collected Papers of RS Rivlin*, pages 1359–1361. Springer, 1997.

[49] Isabelle Guyon, B Boser, and Vladimir Vapnik. Automatic capacity tuning of very large vc-dimension classifiers. In *Advances in Neural Information Processing Systems*, pages 147–155, 1993.

[50] Peter G Hagan, Christoph A Nienaber, Eric M Isselbacher, David Bruckman, Dean J Karavite, Pamela L Russman, Arturo Evangelista, Rossella Fattori, Toru Suzuki, Jae K Oh, et al. The international registry of acute aortic dissection (irad): new insights into an old disease. *Jama*, 283(7):897–903, 2000.

[51] Darren Haskett, Gregory Johnson, Aifang Zhou, Urs Utzinger, and Jonathan Vande Geest. Microstructural and biomechanical alterations of the human aorta as a function of age and location. *Biomechanics and Modeling in Mechanobiology*, 9(6):725–736, 2010.

[52] Kaiming He, Xiangyu Zhang, Shaoqing Ren, and Jian Sun. Deep residual learning for image recognition. In *Proceedings of the IEEE Conference on Computer Vision and Pattern Recognition*, pages 770–778, 2016.

[53] James M Hill and Richard T Shield. Notes on a duality of stress and deformation fields in plane finite elasticity. *Journal of Elasticity*, 4(2):167–172, 1974.

[54] Michael R Hill, Xinjie Duan, Gregory A Gibson, Simon Watkins, and Anne M Robertson. A theoretical and non-destructive experimental approach for direct inclusion of measured collagen orientation and recruitment into mechanical models of the artery wall. *Journal of Biomechanics*, 45(5):762–771, 2012.

[55] Michael R Hill, Xinjie Duan, Gregory A Gibson, Simon Watkins, and Anne M Robertson. A theoretical and non-destructive experimental approach for direct inclusion of measured collagen orientation and recruitment into mechanical models of the artery wall. *Journal of Biomechanics*, 45(5):762–771, 2012.

[56] LF Hiratzka, GL Bakris, JA Beckman, RM Bersin, VF Carr, DE Casey Jr, KA Eagle, LK Hermann, EM Isselbacher, EA Kazerooni, et al. Guidelines for the diagnosis and management of patients with thoracic aortic disease: a report of the american college of cardiology foundation/american heart association task force on practice guidelines, american association for thoracic surgery, american college of radiology, american stroke association, society of cardiovascular anesthesiologists, society for cardiovascular angiography and interventions, society of interventional radiology, society of thoracic surgeons, and society for vascular medicine. *Circulation*, 121(3):e266–e369, 2010.

[57] Tin Kam Ho. Random decision forests. In *Document Analysis and Recognition, 1995., Proceedings of the Third International Conference on*, volume 1, pages 278–282. IEEE, 1995.

[58] Tin Kam Ho. The random subspace method for constructing decision forests. *IEEE Transactions on Pattern Analysis and Machine Intelligence*, 20(8):832–844, 1998.

[59] Thomas Hofmann, Bernhard Schölkopf, and Alexander J Smola. Kernel methods in machine learning. *The Annals of Statistics*, pages 1171–1220, 2008.

[60] Gerhard A Holzapfel, Thomas C Gasser, and Ray W Ogden. A new constitutive framework for arterial wall mechanics and a comparative study of material models. *Journal of Elasticity and the Physical Science of Solids*, 61(1-3):1–48, 2000.

[61] Jay D Humphrey. *Cardiovascular solid mechanics: cells, tissues, and organs*. Springer Science & Business Media, 2013.

[62] JD Humphrey. Computer methods in membrane biomechanics. *Computer Methods in Biomechanics and Biomedical Engineering*, 1(3):171–210, 1998.

[63] Dimitrios C Iliopoulos, Rejar P Deveja, Eleftherios P Kritharis, Despina Perrea, George D Sionis, Konstantinos Toutouzas, Christodoulos Stefanadis, and Dimitrios P Sokolis. Regional and directional variations in the mechanical properties of ascending thoracic aortic aneurysms. *Medical Engineering & Physics*, 31(1):1–9, 2009.

[64] Dimitrios C Iliopoulos, Eleftherios P Kritharis, Spyridon Boussias, Alexandros Demis, Christos D Iliopoulos, and Dimitrios P Sokolis. Biomechanical properties and histological structure of sinus of valsalva aneurysms in relation to age and region. *Journal of Biomechanics*, 46(5):931–940, 2013.

[65] Dimitrios C Iliopoulos, Eleftherios P Kritharis, Athina T Giagini, Stavroula A Papadodima, and Dimitrios P Sokolis. Ascending thoracic aortic aneurysms are associated with compositional remodeling and vessel stiffening but not weakening in age-matched subjects. *The Journal of Thoracic and Cardiovascular Surgery*, 137(1):101–109, 2009.

[66] Eric M Isselbacher. Thoracic and abdominal aortic aneurysms. *Circulation*, 111(6):816–828, 2005.

[67] Gunnar Johansson, Ulf Markström, and Jesper Swedenborg. Ruptured thoracic aortic aneurysms: a study of incidence and mortality rates. *Journal of Vascular Surgery*, 21(6):985–988, 1995.

[68] Jeffrey A Jones, Christy Beck, John R Barbour andJouzas A Zavadzkas, Rupak Mukherjee, Francis G Spinale, and John S Ikonomidis. Alterations in aortic cellular constituents during thoracic aortic aneurysm development. *The American Journal of Pathology*, 175:1746–1756, 2009.

[69] Klaus Kallenbach, Thoralf M Sundt, and Thomas H Marwick. Aortic surgery for ascending aortic aneurysms under 5.0 cm in diameter in the presence of bicuspid aortic valve. *JACC: Cardiovascular Imaging*, 6(12):1321–1326, 2013.

[70] Khalil Khanafer, Ambroise Duprey, Mohammad Zainal, Marty Schlicht, David Williams, and Ramon Berguer. Determination of the elastic modulus of ascending thoracic aortic aneurysm at different ranges of pressure using uniaxial tensile testing. *The Journal of Thoracic and Cardiovascular Surgery*, 142(3):682–686, 2011.

[71] Kennith F Layton, David F Kallmes, HJ Cloft, EP Lindell, and VS Cox. Bovine aortic arch variant in humans: clarification of a common misnomer. *American Journal of Neuroradiology*, 27(7):1541–1542, 2006.

[72] Kibaek Lee, Junjun Zhu, Judy Shum, Yongjie Zhang, Satish C Muluk, Ankur Chandra, Mark K Eskandari, and Ender A Finol. Surface curvature as a classifier of abdominal aortic aneurysms: a comparative analysis. *Annals of Biomedical Engineering*, 41(3):562–576, 2013.

[73] Liang Liang, Minliang Liu, Caitlin Martin, John A Elefteriades, and Wei Sun. A machine learning approach to investigate the relationship between shape features and numerically predicted risk of ascending aortic aneurysm. *Biomechanics and Modeling in Mechanobiology*, pages 1–15, 2017.

[74] Folke Lohse, Nora Lang, Wolfgang Schiller, Wilhelm Roell, Oliver Dewald, Claus-Juergen Preusse, Armin Welz, and Christoph Schmitz. Quality of life after replacement of the ascending aorta in patients with true aneurysms. *Texas Heart Institute Journal*, 36(2):104, 2009.

[75] J Lu and X F Zhao. Pointwise Identification of Elastic Properties in Nonlinear Hyperelastic Membranes-Part I: Theoretical and Computational Developments. *Journal of Applied Mechanics -Transactions ASME*, 76(6):061013/1–061013/10, 2009.

[76] Jia Lu, Shouhua Hu, and Madhavan L Raghavan. A shell-based inverse approach of stress analysis in intracranial aneurysms. *Annals of Biomedical Engineering*, 41(7):1505–1515, 2013.

[77] Jia Lu and Yuanming Luo. Solving membrane stress on deformed configuration using inverse elastostatic and forward penalty methods. *Computer Methods in Applied Mechanics and Engineering*, 308:134–150, 2016.

[78] Jia Lu and Xuefeng Zhao. Pointwise identification of elastic properties in nonlinear hyperelastic membranespart i: theoretical and computational developments. *Journal of Applied Mechanics*, 76(6):061013, 2009.

[79] Jia Lu, Xianlian Zhou, and Madhavan L Raghavan. Computational method of inverse elastostatics for anisotropic hyperelastic solids. *International Journal for Numerical Methods in Engineering*, 69(6):1239–1261, 2007.

[80] Jia Lu, Xianlian Zhou, and Madhavan L Raghavan. Inverse elastostatic stress analysis in pre-deformed biological structures: demonstration using abdominal aortic aneurysms. *Journal of Biomechanics*, 40(3):693–696, 2007.

[81] Jia Lu, Xianlian Zhou, and Madhavan L Raghavan. Inverse method of stress analysis for cerebral aneurysms. *Biomechanics and Modeling in Mechanobiology*, 7(6):477–86, December 2008.

[82] Jia Lu, Xianlian Zhou, and Madhavan L Raghavan. Inverse method of stress analysis for cerebral aneurysms. *Biomechanics and Modeling in Mechanobiology*, 7(6):477–486, 2008.

[83] Jia Lu, Xianlian L Zhou, and Madhavan L Raghavan. Inverse elastostatic stress analysis in pre-deformed biological structures: demonstration using abdominal aortic aneurysms. *Journal of Biomechanics*, 40(3):693–696, 2007.

[84] Yuanming Luo, Ambroise Duprey, Stéphane Avril, and Jia Lu. Characteristics of thoracic aortic aneurysm rupture in vitro. *Acta Biomaterialia*, 42:286–295, 2016.

[85] Steven P Marra, Francis E Kennedy, Jeffrey N Kinkaid, and Mark F Fillinger. Elastic and rupture properties of porcine aortic tissue measured using inflation testing. *Cardiovascular Engineering*, 6(4):123–31, December 2006.

[86] Takeo MATSUMOTO, Tomohiro FUKUI, Toshihiro TANAKA, Naoko IKUTA, Toshiro OHASHI, Kiichiro KUMAGAI, Hiroji AKIMOTO, Koichi TABAYASHI, and Masaaki SATO. Biaxial tensile properties of thoracic aortic aneurysm tissues. *Journal of Biomechanical Science and Engineering*, 4(4):518–529, 2009.

[87] Takeo Matsumoto, Tomohiro Fukui, Toshihiro Tanaka, Naoko Ikuta, Toshiro Ohashi, Kiichiro Kumagai, Hiroji Akimoto, Koichi Tabayashi, and Masaaki Sato. Biaxial tensile properties of thoracic aortic aneurysm tissues. *Journal of Biomechanical Science and Engineering*, 4(4):518–529, 2009.

[88] Geoffrey McLachlan, Kim-Anh Do, and Christophe Ambroise. *Analyzing Microarray Gene Expression Data*, volume 422. John Wiley & Sons, 2005.

[89] Karol Miller and Jia Lu. On the prospect of patient-specific biomechanics without patient-specific properties of tissues. *Journal of the Mechanical Behavior of Biomedical Materials*, 27:154–166, 2013.

[90] Dinesh H Mohan and John W Melvin. Failure Properties of Passive Human Aortic Tissue. II- Biaxial Tension Tests. *Journal of Biomechanics*, 16(1):31–44, 1983.

[91] RW Ogden. A note on duality in finite elasticity. *Journal of Elasticity*, 5(1):83–88, 1975.

[92] Ruth J Okamoto, Jessica E Wagenseil, William R DeLong, Sara J Peterson, Nicholas T Kouchoukos, and Thoralf M Sundt III. Mechanical properties of dilated human ascending aorta. *Annals of Biomedical Engineering*, 30(5):624–635, 2002.

[93] Linda A Pape, Thomas T Tsai, Eric M Isselbacher, Jae K Oh, Patrick T OGara, Arturo Evangelista, Rossella Fattori, Gabriel Meinhardt, Santi Trimarchi, Eduardo Bossone, et al. Aortic diameter 5.5 cm is not a good predictor of type a aortic dissection observations from the international registry of acute aortic dissection (irad). *Circulation*, 116(10):1120–1127, 2007.

[94] Salvatore Pasta, Julie A Phillippi, Alkiviadis Tsamis, Antonio D'Amore, Giuseppe M Raffa, Michele Pilato, Cesare Scardulla, Simon C Watkins, William R Wagner, Thomas G Gleason, et al. Constitutive modeling of ascending thoracic aortic aneurysms using microstructural parameters. *Medical Engineering and Physics*, 38(2):121–130, 2016.

[95] F. Pedregosa, G. Varoquaux, A. Gramfort, V. Michel, B. Thirion, O. Grisel, M. Blondel, P. Prettenhofer, R. Weiss, V. Dubourg, J. Vanderplas, A. Passos, D. Cournapeau, M. Brucher, M. Perrot, and E. Duchesnay. Scikit-learn: Machine learning in Python. *Journal of Machine Learning Research*, 12:2825–2830, 2011.

[96] Thuy Pham, Caitlin Martin, John Elefteriades, and Wei Sun. Biomechanical characterization of ascending aortic aneurysm with concomitant bicuspid aortic valve and bovine aortic arch. *Acta Biomaterialia*, 9(8):7927–7936, 2013.

[97] Joseph E Pichamuthu, Julie A Phillipi, Deborah a Cleary, Douglas W Chew, John Hempel, David a Vorp, and Thomas G Gleason. Differential tensile strength and collagen composition in ascending aortic aneurysms by aortic valve phenotype. *The Annals of Thoracic Surgery*, 96(6):2147–54, December 2013.

[98] LA Piegl and W Tiller. The nurbs book: Monographs in visual communication, ch. b-spline basis function. *Springer,*, 11:1, 1997.

[99] David M Pierce, Franz Maier, Hannah Weisbecker, Christian Viertler, Peter Verbrugghe, Nele Famaey, Inge Fourneau, Paul Herijgers, and Gerhard A Holzapfel. Human thoracic and abdominal aortic aneurysmal tissues: damage experiments, statistical analysis and constitutive modeling. *Journal of the Mechanical Behavior of Biomedical Materials*, 2014.

[100] David M Pierce, Franz Maier, Hannah Weisbecker, Christian Viertler, Peter Verbrugghe, Nele Famaey, Inge Fourneau, Paul Herijgers, and Gerhard A Holzapfel. Human thoracic and abdominal aortic aneurysmal tissues: damage experiments, statistical analysis and constitutive modeling. *Journal of the Mechanical Behavior of Biomedical Materials*, 2014.

[101] V Pressler and JJ McNamara. Aneurysm of the thoracic aorta. review of 260 cases. *The Journal of Thoracic and Cardiovascular Surgery*, 89(1):50–54, 1985.

[102] Reed E Pyeritz and Victor A McKusick. The marfan syndrome: diagnosis and management. *New England Journal of Medicine*, 300(14):772–777, 1979.

[103] ML Raghavan and David A Vorp. Toward a biomechanical tool to evaluate rupture potential of abdominal aortic aneurysm: identification of a finite strain constitutive model and evaluation of its applicability. *Journal of Biomechanics*, 33(4):475–482, 2000.

[104] William C Roberts and Jong M Ko. Frequency by decades of unicuspid, bicuspid, and tricuspid aortic valves in adults having isolated aortic valve replacement for aortic stenosis, with or without associated aortic regurgitation. *Circulation*, 111(7):920–925, 2005.

[105] Aaron Romo, Pierre Badel, Ambroise Duprey, Jean-Pierre Favre, and Stéphane Avril. In vitro analysis of localized aneurysm rupture. *Journal of Biomechanics*, 47(3):607–616, 2014.

[106] Aaron Romo, Pierre Badel, Ambroise Duprey, Jean-Pierre Favre, and Stéphane Avril. In vitro analysis of localized aneurysm rupture. *Journal of Biomechanics*, 47(3):607–616, 2014.

[107] Emile Saliba, Ying Sia, et al. The ascending aortic aneurysm: When to intervene? *IJC Heart & Vasculature*, 6:91–100, 2015.

[108] Richard T Schield. Inverse deformation results in finite elasticity. *Zeitschrift für angewandte Mathematik und Physik ZAMP*, 18(4):490–500, 1967.

[109] Karen Simonyan and Andrew Zisserman. Very deep convolutional networks for large-scale image recognition. *arXiv preprint arXiv:1409.1556*, 2014.

[110] Dimitrios P Sokolis and Dimitrios C Iliopoulos. Impaired mechanics and matrix metalloproteinases/inhibitors expression in female ascending thoracic aortic aneurysms. *Journal of the Mechanical Behavior of Biomedical Materials*, 34:154–164, 2014.

[111] Dimitrios P Sokolis, Eleftherios P Kritharis, Athina T Giagini, Konstantinos M Lampropoulos, Stavroula A Papadodima, and Dimitrios C Iliopoulos. Biomechanical response of ascending thoracic aortic aneurysms: association with structural remodelling. *Computer Methods in Biomechanics and Biomedical Engineering*, 15(3):231–248, 2012.

[112] Dimitrios P Sokolis, Eleftherios P Kritharis, and Dimitrios C Iliopoulos. Effect of layer heterogeneity on the biomechanical properties of ascending thoracic aortic aneurysms. *Medical & Biological Engineering & Computing*, 50(12):1227–1237, 2012.

[113] AJM Spencer. The static theory of finite elasticity. *IMA Journal of Applied Mathematics*, 6(2):164–200, 1970.

[114] Jeremiah Stamler, Rose Stamler, and James D Neaton. Blood pressure, systolic and diastolic, and cardiovascular risks: US population data. *Archives of Internal Medicine*, 153(5):598–615, 1993.

[115] Monica M Stringfellow, Peter F Lawrence, and Richard G Stringfellow. The influence of aorta-aneurysm geometry upon stress in the aneurysm wall. *Journal of Surgical Research*, 42(4):425–433, 1987.

[116] Shukei Sugita and Takeo Matsumoto. Yielding phenomena of aortic wall and intramural collagen fiber alignment: Possible link to rupture mechanism of aortic aneurysms. *Journal of Biomechanical Science and Engineering*, 8(2):104–113, 2013.

[117] Shukei Sugita, Takeo Matsumoto, Toshiro Ohashi, Kiichiro Kumagai, Hiroji Akimoto, Koichi Tabayashi, and Masaaki Sato. Evaluation of rupture properties of thoracic aortic aneurysms in a pressure-imposed test for rupture risk estimation. *Cardiovascular Engineering and Technology*, 3(1):41–51, 2012.

[118] JONATHAN P VANDE GEEST, Elena S Di Martino, Ajay Bohra, Michel S Makaroun, and David A Vorp. A biomechanics-based rupture potential index for abdominal aortic aneurysm risk assessment. *Annals of the New York Academy of Sciences*, 1085(1):11–21, 2006.

[119] Henry Vaughan. Pressurising a prestretched membrane to form a paraboloid. *International Journal of Engineering Science*, 18(1):99–107, 1980.

[120] E Venstel and T Krauthammer. Thin plates and shells, theory, analysis and application, 2001.

[121] David A Vorp, ML Raghavan, and Marshall W Webster. Mechanical wall stress in abdominal aortic aneurysm: influence of diameter and asymmetry. *Journal of Vascular Surgery*, 27(4):632–639, 1998.

[122] David A Vorp, Brian J Schiro, Marek P Ehrlich, Tatu S Juvonen, M Arisan Ergin, and Bartley P Griffith. Effect of aneurysm on the tensile strength and biomechanical behavior of the ascending thoracic aorta. *The Annals of Thoracic Surgery*, 75(4):1210–1214, 2003.

[123] David HJ Wang, Michel S Makaroun, Marshall W Webster, and David A Vorp. Effect of intraluminal thrombus on wall stress in patient-specific models of abdominal aortic aneurysm. *Journal of Vascular Surgery*, 36(3):598–604, 2002.

[124] JS Wilson, S Baek, and JD Humphrey. Importance of initial aortic properties on the evolving regional anisotropy, stiffness and wall thickness of human abdominal aortic aneurysms. *Journal of The Royal Society Interface*, 9(74):2047–2058, 2012.

[125] Ian H Witten, Eibe Frank, Mark A Hall, and Christopher J Pal. *Data Mining: Practical machine learning tools and techniques*. Morgan Kaufmann, 2016.

[126] Hiroshi Yamada, Noriyuki Sakata, Hideichi Wada, Tadashi Tashiro, and Eiki Tayama. Age-related distensibility and histology of the ascending aorta in elderly patients with acute aortic dissection. *Journal of Biomechanics*, 48(12):3267–3273, 2015.

[127] Takahiro Yamada. Finite element procedure of initial shape determination for hyperelasticity. In *Computational Mechanics 95*, pages 2456–2461. Springer, 1995.

[128] WH Yang and WW Feng. On axisymmetrical deformations of nonlinear membranes. *Journal of Applied Mechanics*, 37(4):1002–1011, 1970.

[129] Nuran Yener, G Levent Oktar, Dilek Erer, M Murat Yardimci, and Ali Yener. Bicuspid aortic valve. *Annals of Thoracic and Cardiovascular Surgery*, 8(5):264–267, 2002.

[130] Miroslav Zemánek, Jiří Burša, and Michal Děták. Biaxial tension tests with soft tissues of arterial wall. *Engineering Mechanics*, 16(1):3–11, 2009.

[131] Xuefeng Zhao, Xiaolin Chen, and Jia Lu. Pointwise identification of elastic properties in nonlinear hyperelastic membranespart ii: experimental validation. *Journal of Applied Mechanics*, 76(6):061014, 2009.

[132] Xuefeng Zhao, Xiaolin Chen, and Jia Lu. Pointwise Identification of Elastic Properties in Nonlinear Hyperelastic MembranesPart II: Experimental Validation. *Journal of Applied Mechanics*, 76(6):061014, 2009.

[133] Xianlian Zhou and Jia Lu. Inverse formulation for geometrically exact stress resultant shells. *International Journal for Numerical Methods in Engineering*, 74(8):1278–1302, 2008.

[134] Xianlian Zhou and Jia Lu. Estimation of vascular open configuration using finite element inverse elastostatic method. *Engineering with Computers*, 25(1):49–59, 2009.

[135] Xianlian Zhou, Madhavan L Raghavan, Robert E Harbaugh, and Jia Lu. Patient-specific wall stress analysis in cerebral aneurysms using inverse shell model. *Annals of Biomedical Engineering*, 38(2):478–489, 2010.